Wireless Communications and Mobile Computing

Deep Learning Enabled Free Space Optical Communication Systems

Lead Guest Editor: Vivek Kumar Dwivedi
Guest Editors: Ghanshyam Singh and Abhijeet Upadhya

Deep Learning Enabled Free Space Optical Communication Systems

Wireless Communications and Mobile Computing

Deep Learning Enabled Free Space Optical Communication Systems

Lead Guest Editor: Vivek Kumar Dwivedi
Guest Editors: Ghanshyam Singh and Abhijeet Upadhya

Contents

Hindawi
Wireless Communications and Mobile Computing
Volume 2023, Article ID 3950657, 12 pages
https://doi.org/10.1155/2023/3950657

Review Article

Machine Learning in Visible Light Communication System: A Survey

Vishal Narain Saxena, Vivek K. Dwivedi, and Juhi Gupta

Department Electronics and Communication, Jaypee Institute of Information Technology, Noida, India

Correspondence should be addressed to Juhi Gupta; singla.juhi@gmail.com

Received 27 April 2022; Revised 27 October 2022; Accepted 24 November 2022; Published 10 February 2023

Academic Editor: Abdul Basit

With the widespread adoption of high bandwidth utilisation, visible light communication (VLC) has emerged as a potential solution to meet the demands for high-speed data communication due to its simultaneous illumination and transmission. However, numerous nonlinear distortions in VLC cause substantial signal processing challenges and diminish the system's efficacy. VLC communication based on machine learning (ML) approaches provides a greater ability to offset the negative impacts of transceiver nonlinearity. ML is applicable to a variety of VLC challenges, including channel estimation, jitter compensation, position tracking, modulation detection, phase estimation, and security. This study provides a detailed review of several machine learning (ML) algorithms to reduce the design complexity of indoor VLC transmission, as well as ML applications in different design aspects to improve system performance. Furthermore, various applications, challenges, and future research directions based on machine learning algorithms in VLC are addressed.

1. Introduction

Nowadays, with the increasing demand for high data rate transmission, visible light communication (VLC) has gained research popularity as it operates on the upper layer of the electromagnetic spectrum, which is license-free with negligible intrusion, enriched with high data rate and high spectrum efficiency [1, 2]. VLC communication is more economical, more energy efficient, and equipped with a spectrum that is 1000 times more efficient than radio frequency spectrum and can simultaneously be used for communication and illumination [3]. Therefore, the above-mentioned advantages make VLC a viable indoor radio frequency communication option. Furthermore, VLC is also gaining research interest in the area of underwater communication for high-speed and long-distance wireless communication [4].

However, as technology advances, managing large amounts of data becomes more difficult, causing additional challenges and constraints on the communication network in terms of bandwidth, latency, and dependability. To overcome these limitations, communication technologies and architectures have evolved, including the use of upgraded modulation techniques, novel multiplexing approaches, and greater security. However, these new developments make the system even more complicated, making it even more difficult to operate and manage [5]. Conversely, the present optical communication systems are stationary, meaning that the physical channel path between source and destination is unchanging. Consequently, the complexity of the hardware components is reduced. However, optical communication systems of the next generation are expected to be dynamic, spectrum grid-free, modulation format-free, programmable, and adaptable [5]. As a result, these characteristics will improve the system's performance, adaptability, and efficiency.

Machine learning (ML) approaches are potential options for improving the intelligence of communication nodes. It is an idle approach for solving complex problems that take a lot of iteration with conventional methods, as well as problems that do not have a conventional solution. In the ML approach, traditional software can be replaced with ML procedures that gain knowledge from prior information in order to solve complex problems [6]. In wireless

communication, ML has progressed as a practice to the point where it now enables wireless systems to understand and retrieve information by conversing with data. Researchers and engineers across the world have expressed preparatory attention and discourse about the viability of developing 5G standards with the help of machine learning protocols [7, 8]. Wireless communication and ML, on the other hand, have been viewed as distinctive research areas, regardless of the possibility they may have when used together. In wireless communication channel modelling, algorithms are implemented based on probability and signal processing concepts. When such algorithms are evaluated in scenarios, they show some imprecision, which is likely to result in an erroneous performance assessment. ML techniques can monitor defects in systems without the use of complex algorithms. Moreover, wireless signals and, particularly, optical data has limited dataset [9]. Channel estimation and forecasting [10–13], location tracking [14–17], and modulation identification [18–20] are some of the implementations that ML can handle in wireless communication. In VLC, a number of ML algorithms have been implemented in different design scenarios to improve system performance. Many ML algorithms can be used in VLC to minimise nonlinearities, including parametrization from noise, evaluating the complicated mapping correlation between input and output, and assessing expected output depending on the given samples [4, 21]. Further, ML algorithms like the neural network (NN), the k-means algorithm, and the support vector machine (SVM) significantly address the different channel deficiencies, managing optical efficiency and specifying modulation and bit rate [22]. The indoor positioning for VLC network has been addressed using k-Nearest Neighbors (k-NN), weighted k-NN (wk-NN), artificial neural networks (ANN), and clustering as part of the VLC framework [14–24]. Furthermore, SVM, Gaussian mixture model (GMM), and k-means algorithms can efficiently accommodate the nonlinear degradation of VLC systems caused by phase variation [25, 26].

The use of ML algorithms in high-speed VLC systems is an effective method for addressing inherent limitations such as nonlinearity, jitter, and eavesdropping. In addition, ML methods can be efficiently used to estimate modulation, phase, and channel, as well as to track a user's location in a real-time scenario. In the literature, some articles cover various ML algorithms that can be used with the optical wireless communication (OWC) system. The authors of [5] reviewed modulation format identification (MFI) and optical performance monitoring (OPM) methods in the OWC system, while [27] compared some of the ML algorithms that can be used in the OWC systems. The authors of [4] discussed the VLC framework and examined some traditional applications of ML algorithms in VLC. In addition, the authors of [28] reviewed ML algorithms used in VLC indoor tracking. However, to the best of the authors' knowledge, a comprehensive review of ML techniques describing the limitations, specifically in VLC systems, and the solutions to these limitations are still not there in the literature. Therefore, different from the aforementioned studies, this paper provides a comprehensive review of different ML algorithms to reduce the complexity of design and thereby improving the performance of the VLC system in different applications. The contributions of this study are briefed as follows:

(1) A comprehensive review of different ML algorithms implemented in VLC network is presented

(2) Various challenges in VLC system design, such as nonlinearity, jitter, and security, are discussed. Further, the potential ML algorithms to overcome these challenges are described

(3) ML applications in VLC-based indoor positioning and recently explored ML algorithms for channel estimation, phase estimation, and modulation identification to improve VLC transmission characteristics are discussed

(4) Finally, possible challenges and future research directions in VLC based ML algorithms are addressed

The remainder of the paper is organised in the following manner: an ML-based VLC system is illustrated in Section 2. Section 3 discussed some of the ML algorithms applied to VLC systems. Section 4 illustrates VLC limitation factors such as transmitter side nonlinearity, eavesdropping, channel distortion, jitter, positioning, and the effects of receiving nonlinearity on modulation and phase estimation, as well as ML algorithms that were used to mitigate these constraints. Section 5 does comparative studies on ML algorithms. Section 6 discusses some future challenges and areas in VLC where ML algorithms can be applied, followed by a conclusion in Section 7.

2. ML-Based VLC System

We consider an indoor environment where a light source based on a light-emitting diode (LED) is used simultaneously for illumination and data transmission in VLC system. The modulating waveforms change the intensity of the LEDs to obtain data rate up to Gbps [29]. Traditional modulation techniques used in radio frequency systems need to be modified to meet the requirement of optical signal positive value for intensity modulation and also the average and maximum intensity limitations imposed by LEDs and the targeted illumination characteristics [9].

VLC systems in Figure 1 are composed of three components: an LED-based transmitter, an optical-based VLC channel, and an optical-based photo detector (PD) receiver. The VLC transmitter system modulates the radio frequency carrier signal from a binary stream of information, preequalizes and upconverts, and finally modulates the intensity of the LED light through a modulated electrical signal. In VLC, the transmission medium is either free space (mostly in an indoor environment) or underwater. The VLC receiver uses a number of different processes, including downconversion, postequalization, demodulation, and decryption, to achieve the original binary dataset. The BER of the decrypted binary dataset is determined from the decoded

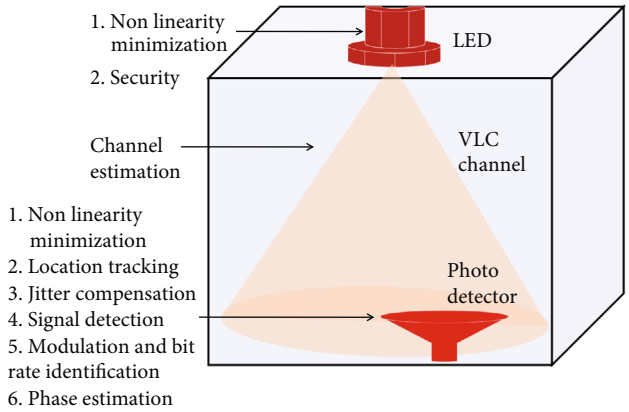

Figure 1: ML-based VLC system.

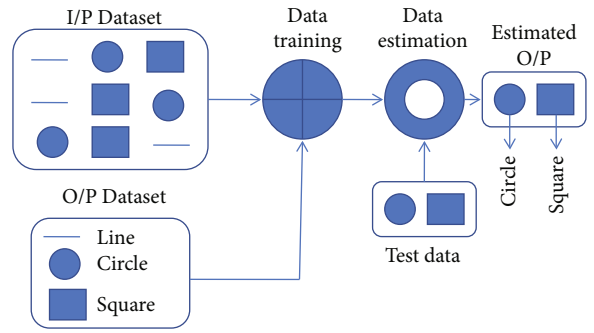

Figure 2: Supervised ML.

bitwise dataset, which indicates the performance of the VLC system [4]. Both the transmitter and the receiver are typically comprised of different ML-based design aspects in order to improve overall VLC system performance. Therefore, the areas of improvement based on ML techniques are mitigation of nonlinearity at the transceiver, channel estimation, jitter compensation, location tracking, modulation detection, phase estimation, and security.

3. Machine Learning

The primary objective of ML technique is to design an algorithm which uses a sufficient number of training datasets in order to establish a correlation between input (i/p) and output (o/p) parameters without specifically stating the nature of the linkage that exists between these two. This section highlights some of the most widely used ML algorithms in the VLC network.

3.1. Supervised ML. In the ML technique, an unidentified function is predicted, which is used to map the i/p, demonstrating the attribute of a specific event, to the o/p, demonstrating the solution to that event [5]. When both i/p and o/p datasets are used during the training phase, this type of ML is referred to as supervised ML (SL). To train the model in SL, a huge volume of dataset containing i/p and its corresponding sets of o/p of an event is used. The estimated o/p is compared to the actual o/p in the training stage, and multiple iterations are used to improve the system's accuracy. After the model has been trained, it is tested with an unfamiliar i/p, referred to as the "testing scenario," and the model precision is obtained by predicting the o/p in the testing event as shown in Figure 2.

The different SL algorithms significant for VLC systems are described as follows:

3.1.1. k-Nearest Neighbor (k-NN). k-NN is among the most simple SL technique which depends on nonparametric tests. The o/p in k-NN is anticipated through i/p-o/p relations established during the training phase. The Manhattan, Hamming, and Euclidean distances are used to determine the tightness between the i/p and o/p datasets [5]. During the training phase, the data is grouped and labelled to facilitate the search. Thereafter, to estimate the o/p from i/p sets the highest number of points in k-closest neighbors are used. Furthermore, Figure 3 graphically depicts the data classification via k-NN technique, in which datasets are labelled into three groups, namely, blue, green, and yellow, based on their colour. The colour red is used to represent unknowable data in this case. For $k = 6$, three of the six closest neighbors are of the colour green, two are of the colour blue, and one is of the colour yellow. Therefore, unidentified data corresponds to group green.

k-NN can also be applied in data regression by merely taking the mean of k-closest neighbors. The most fundamental practice for predicting the value of k is to test individual data at a variety of k values and then choose the k with the least amount of error. Although k-NN is the most appropriate algorithm for handling huge amounts of data and nonlinear applications, its implementation in practical cases is limited by the cost of storage capacity and latency [5].

3.1.2. Support Vector Machine (SVM). The main objective of SVM is to create the most suitable criteria known as hyperplane which can further divide the space into different categories. The SVM can be divided into two types: linear SVM, in which data points can be segregated using a straight line. Other types of SVM include nonlinear SVM, which allows data points to be separated using nonlinear paths [22].

Furthermore, Figure 4 depicts a linear SVM. The SVM has two primary characteristics: the hyperplane and the support vector. We always choose the optimal hyperplane, which is the farthest away from the datasets. Support vectors are the points that are nearest to the hyperplane and have the greatest impact on the location of a hyperplane.

3.1.3. Artificial Neural Networks (ANNs). The ANN is a subset of AI motivated by the human brain biological structure and is modelled like a nervous system. It is a mathematical connection that is dependent on neurons, which are responsible for the proper operation of the human nervous system. ANN, like the human brains, has nerve cells associated with one another in multiple levels of the system called nodes [23].

NN contains a collection of artificial neurons, referred to as nodes, and they are structured in the form of a layer-by-layer hierarchy. In addition, Figure 5 depicts an ANN structure which contains three layers. The three layers are the i/p

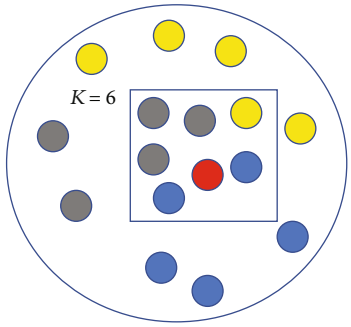

Figure 3: Classification using *k*-NN.

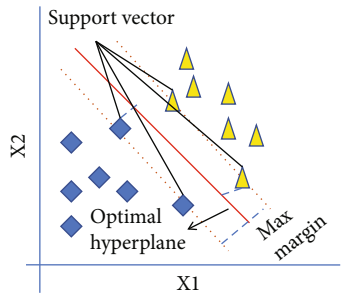

Figure 4: Data segregation using SVM.

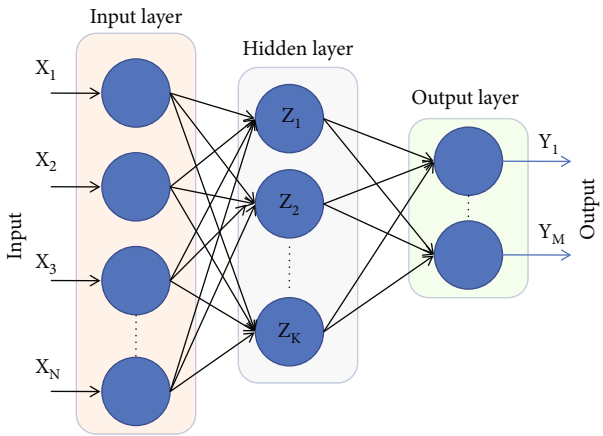

Figure 5: ANN Structure.

layer, the hidden layer, and the o/p layer. The i/p layer runs the data via an activation function prior to moving it to the next layer. The hidden layer obtains the patterns between i/p and features, and the i/p undergoes a sequence of transitions in the hidden layer, culminating in o/p layer. In ANN, the weightage sum of i/p is computed along with a bias, where weightage is the parameters used by ANN to address a particular issue, and they refer to the quality of interaction among neurons in ANN. Thereafter, the weightage sum is forwarded to the activation function, which determines the activation or deactivation of a node, and the o/p is limited to the activated nodes. Further, a DNN is an ANN with two or more hidden layers and is useful for nonlinear modelling that is difficult to solve. Furthermore, it involves a lot of data, which necessitates a longer training period. The advantages of ANN include the ability to manage data parallelly, a potential to keep a data across the whole network, the ability to perform with insufficient information, and low latency [5]. However, it is more complex than *k*-NN and SVM.

3.2. Unsupervised ML (USL). In USL, only i/p or o/p information is used to operate and retrieve data, and these algorithms are developed by examining common trends among datasets. The USL algorithms are based on clustering and dimensionality reduction. In addition, the following subsection will discuss some of the USL algorithms that are implemented in the VLC system.

3.2.1. k-Means Algorithms. It is a partition-based clustering algorithm, wherein clustering data points are divided in different categories based on their alikeness. The *k*-means technique's primary goal is to choose *k* cluster centres at irregular intervals. After that, every data point is assigned to the closest centre using the distance function, and equilibrium can be achieved by iteratively adjusting the centre and relocating the points from one group to the next [24]. It is simple to use and convenient, but selecting the distance function and number of centres *k* is challenging.

3.2.2. Gaussian Mixture Model (GMM). GMM is a distribution-dependent clustering technique. It distributes the data to multiple groups based on its probability distribution, i.e., data in a group has a high likelihood of having a similar distribution [26]. The GMM model includes several Gaussian distributions, each of which has the following control variables: (a) the distribution centre; (b) a covariance determining the thickness of the Gaussian function; and (c) a mixing coefficient. The optimum solution for these variables can be obtained through Maximum Likelihood Estimation (MLE). However, rather than using a single Gaussian, GMM uses a combination of Gaussian, which makes determining the controlling variables for the entire combination more complex and limits GMM's operation.

3.2.3. Density-Based Spatial Clustering of Applications with Noise (DBSCAN). DBSCAN is a density-based clustering technique that creates groups of high-density points (the points that are very close to each other based on Euclidean distance) and considers the neighboring points of low density to be outliers. By using a threshold, DBSCAN can separate the main data from the outliers (noise) in complex datasets [30]. This technique, however, becomes more vulnerable to the threshold setup. The above problem can be overcome by using ordering points to determine the clustering structure (OPTICS) that uses both the data density and locational similarity into consideration.

4. ML Application in VLC

In contemporary communication, VLC has emerged as an innovative transmission technology due to its potential advantages over radio frequency communication. Despite the fact that it has numerous advantages, its applications are hindered by the limitations of its operational systems, which include nonlinearity in the transmitter and receiver,

Table 1: ML algorithms in nonlinearity mitigation.

Method	Ref.	Outcomes
GMM	[20, 26]	(1) Easy to implement (2) Require small set of variable (3) Higher dynamic range is achieved
k-Means algorithm	[26, 53]	(1) Simple structure (2) Extra learning model not needed (3) Data rate up to 400 Mbit/s is achieved (4) High Q-factor (5) Does not work well with cluster of different sizes and densities
LM algorithm	[33]	(1) Can manage multiparameter frameworks (2) Performance improvement is achieved in the context of training complexity (3) It takes a long time in some scenarios
Gaussian kernel-aided DNN	[34]	(1) Can significantly decrease training iterations up to 47.6% (2) Data rate up to 1.5 Gbps
Probabilistic Bayesian-based learning	[35]	(1) Compensate for the negative effects of VLC source nonlinearity (2) Improved BER

eavesdropping, channel distortion, and jitter. As a result, this section will review all of the performance-limiting factors that have an impact on the VLC system, as well as their ML-based mitigation techniques.

4.1. Nonlinearity Mitigation. Nonlinear distortion is a significant problem in VLC systems. The LED in a VLC system has a nonlinear transfer function, which means that the relationship between voltage and current is not linear (it does not follow Ohm's law), implying that LED illumination power is not directly proportional to the controlling element [26]. The nonlinearity in the VLC channel results in serious fading effects. Further, due to the saturation effect of PD, the received information gets clipped [4]. The perspective modelling approach based on ML is useful for the redressal of nonlinearity as it employs induction instead of omission. In the ML model, there are several approaches such as regression analysis, classification techniques, and clustering that have strong nonlinear mapping potential. Thereafter, ML can analyse the system's parameters using a portion of the message data as a label. This allows the system to compensate against nonlinear distortion [18]. In literature, various ML techniques are developed as an intelligence system to deal with nonlinearity in VLC in a range of environments. One of the technique is decision feedback- (DF-) based equalisation which is a type of nonlinear equalisation that rectifies the present bit in accordance with the decision of the prior bit (low or high). This enables the DF equaliser to compensate for the distortion in the present bit resulting from the prior bit. Furthermore, it has a potential to mitigate ISI without intensifying the noise in order to improve the bit rate [31, 32]. Others are ANN-based techniques, which use a portion of the transmitted data as a label and understand the parameters of the systems via their effective nonlinear capabilities, thereby mitigating nonlinear distortions. Moreover, Levenberg-Marquardt (LM) algorithm-based ANN [33], Gaussian kernel-aided DNN [34], and probabilistic Bayesian-based learning (PBL) [35] are applied to mitigate nonlinearity in the VLC system. However, ANN outperforms DF equalisation, but still it is overlooked in VLC due to the additional challenges imposed on the hardware design process. Table 1 summarises some prominent algorithms that have been developed to mitigate nonlinearity in the VLC transceiver architecture.

4.2. Security. Security in any wireless network is a very essential factor. Secured wireless networks prevent confidential data from being overheard. Although the VLC system has a low probability of being wiretapped, it is still a serious issue, especially in public areas such as community centres, malls, research centres, and other places where shared information can be retrieved by multiple persons [36]. Therefore, a number of studies to improve VLC security have been published; one of which is reinforcement learning- (RL-) based beamforming to protect eavesdropping of sensitive information [37]. To obtain a secure VLC network, an RL-based multiple-input-single-output beamforming regulate approach is developed for the Markov decision process in a dynamic situation to optimise beamforming strategy in [37]. Furthermore, deep reinforcement learning-based beamforming is used to enhance the convergence rate and learning of antiwiretapped networks in order to deal with large dimensional and consistent activity environments successfully. In addition, artificial noise-based linear precoding enhances the secrecy rate by employing truncated discrete generalized normal distribution [38]. However, various investigations on physical layer security (PLS) on VLC to determine secrecy outage probability, secrecy threshold, and secrecy capacity are not reviewed because they are outside the scope of this review. Further, interested readers can refer to [36] for information on PLS in VLC.

4.3. Channel Estimation. The visible spectrum (430 THz to 790 THz) is used to transmit optical data in the VLC system. Signals are typically transmitted through LEDs using intensity modulation (IM)/direct detection (DD) scheme, with PD recording signal fluctuations on the recipient side to

Table 2: ML algorithms in channel estimation.

Method	Ref.	Outcomes
ANN	[10]	(1) Simple to use (2) Precision level of up to 97.7% can be obtained
Adaptive PBL	[12]	(1) Can estimate real-time indoor VLC channel (2) Require less training time (3) Decrease calculation complexity
Bayesian compressive sensing	[13]	(1) It can be used to predict underwater VLC channels (2) Enhance efficiency (3) Increase prediction correctness
DNN	[11]	(1) Improve BER without requiring any complicated calculations (2) It has BER performance superior to LS and MMSE algorithms

transform them into digital format. An appropriate channel modelling is the most essential aspect for resilient, error-free, and accurate VLC signal transmission. However, due to uncertain changes in a transmission medium and variable characteristics including unidentified reflective surfaces, rapid changes in noise, and moving structures, channel behaviour is analytically more difficult and nearly unobtainable [10]. However, ML is an effective technique for measuring the correlation among both the inputs and outputs of the VLC network, and they are extremely beneficial if such a relationship is nonlinear in nature. In [11], a DNN algorithm was developed which learns the features of the transmitted medium by labelling the message data as labels and utilising collected data at a receiver as samples. This DNN algorithm outperforms least squares (LS) and minimum mean square error (MMSE) in terms of BER without requiring any complicated calculations at the receiver. In addition, in [10], an ANN-based network for predicting the VLC channel is developed. To estimate the channel properties, six input attributes such as refraction of various surfaces, transmitter architecture, line of sight component, noise, and the location of the transceiver are taken into consideration. Within the training process, this framework was able to estimate the channel property with a precision level of up to 97.7%. Further, an adaptive PBL method was developed in [12], which provides an excellent and reliable method for detecting the real-time indoor VLC channel and thereby reducing the training time. The Bayesian compressive sensing approach is modelled to predict the reflective transmission distance in underwater VLC in [13] that can further be used to retrieve the channel properties. The obtained results demonstrate that the pilot overhead reduces; however, the efficiency and prediction correctness increases. Table 2 presents the ML algorithms used to estimate the VLC channel and their findings.

4.4. Location Tracking. With the growing popularity of the mobile Internet, location-based services (LBS) have become increasingly helpful in determining the precise coordinates for location tracing required for routing. However, because of the transmission properties of radio communication and the complicated indoor spaces, accurate positioning becomes challenging in indoor areas than in outdoor spaces. At the same time, VLC-based indoor localization has gained popularity as a viable method of achieving higher reliability in evaluating position than conventional radio frequency techniques while also being nonintrusive. Moreover, VLC-based positioning has several significant benefits, including minimal expense, high durability, and renewability, making it the most efficient option for indoor localization [28]. Despite the fact that VLC indoor localization provides remarkable gains, some limitations such as VLC signal instruction, scattering, and illuminance noise can affect the accuracy of the location. Therefore, various ML algorithms in VLC are being investigated to attain higher location accuracy.

In order to obtain precise location information, photodetector- (PD-) driven tracking and sensor-based tracking are implemented.

4.4.1. PD-Driven Tracking. PD-driven techniques are widely used in indoor location tracking using VLC systems. The position can be precisely determined by estimating the travel time, incident angle, and received signal strength (RSS) at PD. RSS is one of the abovementioned parameters that is simple to obtain without the use of a complicated structure. The RSS-based technique can be classified into two types: geometric and fingerprint-based techniques [39]. In ML, both single and multiclassifiers are implemented to obtain location. In [14], wk-NN is implemented to precisely position the receiver using the weighted Euclidean distance between nodes. 2nd order regression ML model and the polynomial trilateral ML model are explored in [40] for precise positioning. The obtained results in [14, 40] show that these two techniques outperform the RSS technique. Furthermore, [15, 16] generate fingerprint-based database for precise positioning using wk-NN and k-NN, respectively. The authors of [17] compare four machine learning algorithms: SVM, random forest (RF), k-NN, and decision tree (DT). SVM has the highest location precision of 8.6 cm with a mean calculation time of 41.5 ms, while k-NN has the shortest mean calculation time of 5.6 ms with a location precision of 13 cm. The authors of [23] used an ANN to establish a link between the considered RSS and the receiver location, assuming that the RSS calculation error is induced by the VLC reflective surface and multipath impact. Although a huge volume of sampling data is used in the training, the location precision is enhanced, with a mean

location error of 6.39 cm. In addition, RSS-based ANN is investigated in [41] to determine the location of luminaries. The proposed algorithms investigate the highest location error with a line of sight (LoS) component that is 2.9 cm and a non-LoS that is 8.1 cm. Another ML algorithm is clustering that involves uniting a collection of items in such a way that items in the similar set are more closely related to other items in the similar set than items in the opposite set. A pair of LED luminary-based cluster algorithms is investigated in [42], wherein the LEDs are modulated at multiple wavelengths and the RSS is observed at the receiving side, after which a fingerprint region is generated and evaluated for the prediction of the recipient location in an indoor space. The results indicate an average precision of 31 cm, which is much less than the accuracy of other models like ANN. *k*-means clustering in association with linear regression is used [43] in order to achieve accurate positioning where datasets are generated for RSS through several luminaries. The obtained results have a mean accuracy of 40 cm, which is significantly less accurate than some algorithms such as ANN.

However, each ML algorithm has its own set of advantages, such as precision, reliability, and other features. As a result, a ML technique known as "merging of classifiers" can now be used to take advantage of the strengths of single ML algorithms, namely, multiple classifiers. The authors in [44] used a combination of three classifiers: the extreme learning machine (ELM), the RF, and the *k*-NN, and this fusion of classifiers is trained based on RSS fingerprints. Following that, two additional combining techniques, grid-dependent least squares (GD-LS) and grid-independent least squares (GI-LS), are introduced in order to achieve a precise positioning outcome by combining the strengths of each classifier. The output of this algorithm is better than conventional RSS-based positioning, with precision and reliability of less than 0.05 m in 85% of cases. In addition, the authors of [45] investigate two-layer fusion network (TLFN). TLFN is an algorithm that merges several locating predictions created via various fingerprints and different classifiers with supervised ML. Through the combination of such diverse position evaluations, it is possible to improve the precision of location calculation. Comparing the abovementioned combined estimator to a single locating prediction model, the combined estimator is significantly more precise and reliable, with an average precision of 5.38 cm. Despite this, the aforementioned algorithms have significantly more calculation complexity due to the necessity of calculating various classifiers and combining their location estimations.

4.4.2. Sensor-Based Tracking. The incident angle plays an important role in sensor-based tracking; the sensor takes the image and delivers the location of LED coordinates, which can then be used to estimate the location. However, the incident angle is also influenced by the sensor's inclination angle, which can result in positioning errors [28]. Authors in [46, 47] discussed sensor-based ANNs that train the link between picture attributes (primarily illumination) and location variables such as 3D locations, location coordinate, and incident angle. These studies further exhibit that the location inaccuracy induced by sensor inclination angle is efficiently adjusted with high-level precision. Furthermore, unlike traditional location algorithms, these schemes involve a huge volume of data for training. However, it significantly reduces the time required for location estimation, implying that real-time location monitoring is possible. Furthermore, Table 3 illustrates the results of various ML algorithms for VLC positioning.

4.5. Jitter Compensation. Jitter is a common occurrence in the VLC network that has a significant impact on performance and induces signal distortion, which leads to signal estimation errors. The most common type of jitter in VLC is amplitude jitter, which occurs in pulse amplitude-modulated- (PAM-) VLC and has a negative impact on the network's bit error rate (BER). This can be compensated using ML algorithms in the VLC-PAM system. Jitter in VLC networks happens at irregular intervals with no set rules. Therefore, the classification and NN-based techniques become ineffective in addressing this issue. However, signal miscalculation affected by jitter can be mitigated through modified density-based spatial clustering of applications with noise (DBSCAN) algorithms. DBSCAN is a well-known unsupervised ML technique that can distinguish between different types of datasets, obviating the need for additional training data and processes [30]. Authors in [48] illustrate the IQ-Time DBSCAN postequalization technique to reduce the effects of amplitude variations in QAM16 carrier-less amplitude and phase-modulated VLC systems. This technique increases the Q factor from 1.5 to 2.5 dB, with a maximum amplitude variation of 70% of the signal. Furthermore, the authors investigate the abovementioned technique constraint with severe amplitude variation scenarios. In addition, 2D-DBSCAN is represented in [30] to minimise the effect of amplitude variation in PAM8 VLC. The Q-factor of the proposed network is enhanced by a factor of 1.6 to 3.2 dB. Further, this technique also investigates the effect of amplitude variation when the maximum jitter becomes 5% of the mean amplitude. The obtained results show that BER more than 7% hard decision-forward error correction constrain can even be attained at 10% jitter. Furthermore, in [49], the authors examined DBSCAN in a PAM4 carrier-less amplitude and phase-modulated VLC system to reduce amplitude variation. This investigation was carried out at a rate of 600 Mbit/s. In comparison to the conventional scheme, a Q-factor of 2.299 dB to 3.299 dB is obtained by using 0.12 amplitude variation spectrum.

4.6. Modulation Identification. There are several factors in VLC that can contribute signal nonlinearity, including nonlinear LED characteristics, PD nonlinearity, and transceiver circuit nonlinearity. Nonlinearity, for example, can cause severe in-phase and quadrature phase magnitude imbalances at the receiver side, rendering the conventional predefined threshold technique ineffective in signal judgement. Therefore, cluster algorithms of perception decisions (CAPD) [18, 19] and GMM [20] are being investigated in order to mitigate the miscalculation induced by constellation

Table 3: ML algorithms for position estimation.

Method	Ref.	Outcomes
k-NN & wk-NN	[14–17]	(1) The dataset must be modified with the change in transmission medium (2) The models are trained with RSS-based datasets (3) These models outperform conventional methods based on received signal strength (4) [15] Has the best average location accuracy of 4.2 cm (5) Low to moderate efficiency
ANN	[23, 41, 46, 47]	(1) A large amount of sampling data is required (2) Highly reliable after plenty of training process (3) Sensors or RSS-based datasets train models (4) With the LoS component, [41] has the best positioning accuracy of 2.7 cm (5) Useful for real-time location monitoring (6) Highly efficient
k-Means	[42, 43]	(1) Models are trained with RSS-based datasets (2) Moderate reliability (3) Less accurate than ANN and *k*-NN (4) Efficiency moderate to high
Comparison of SVM, RF, *k*-NN, and DT	[17]	(1) Highest location accuracy of 8.6 cm with SVM (2) Shortest mean calculation time of 5.6 cm with *k*-NN
Multiple classifier	[44, 45]	(1) Take advantage of strengths of single classifier (2) Precise and reliable (3) High calculation complexity

discrepancy. In [18], CAPD is developed through *k*-means, which further postequalizes in-phase and quadrature phase amplitude discrepancy losses in carrier-less amplitude and phase-modulated VLC systems and performs the modulation format detection, in order to achieve better performance. The gain of the abovementioned technique is increased by a factor of 1.6 to 2.5 dB compared to the simple linear remuneration technique. This technique also outperforms the Volterra equalisers in terms of performance by lowering the BER minimum of 10% while requiring the least amount of calculation complexity possible. Because the CAPD calculates the coordinates based on the centre and position, it is possible that some specific points located among centres will result in incorrect calculations. As a result, in order to overcome this problem, preequalization-based *k*-means clustering is investigated in [19]. By using carrier-less amplitude and phase-modulated VLC in five bands and sixteen orders, it has been demonstrated that preequalization has a positive impact on the results. This technique is capable of efficiently preventing nonlinear behaviour while also decreasing the BER to the 50% to 99% range. However, in [22], the authors investigate the GMM framework to group the successive data by taking the similarity among them into consideration. The BER results were examined with and without the GMM technique, using a variety of bias currents. According to the obtained results, it has been discovered that the technique with GMM can operate over a wide range of bias current and voltage but requires more time to complete. However, when the data is not large, this time gap is not as significant. Therefore, through GMM, it is possible to obtain enhanced performance while consuming minimal time resources. Table 4 represents the ML algorithms implemented for modulation identification with their findings.

4.7. Phase Estimation. In VLC, nonlinearity can lead to severe phase distortion. The conventional constant modulus algorithm applied to equalisation techniques can lead to miscalculations in the obtained constellation coordinates, which further deteriorates the performance. However, ML techniques like GMM [26], SVM [50], and *k*-means [25] efficiently mitigate nonlinear distortions in VLC induced by phase variation. The authors of [26] evaluated the efficiency of GMM and *k*-means techniques in QAM16 VLC with a high degree of nonlinearity. The authors explored the correlation between peak-to-peak voltage and BER. In LEDs, the voltage and controlling elements are nonlinear, and when the peak-to-peak voltage is extremely low or extremely high, the signals suffer from significant distortions. According to the results, GMM has a lower BER than *k*-means. However, the peak-to-peak voltage obtained with GMM is 250 mV which is higher than *k*-means. Further, gain in GMM is increased by a factor of 1 dB than *k*-means with 1.5 Gbps bit rate. Further, in [25], authors investigated QAM8 coordinates in underwater VLC. The investigation of BER at various peak-to-peak voltage levels is conducted. Once the *k*-means phase correction technique is applied to each coordinate, the BER of each coordinate is reduced to a certain level, and with a bit rate of 1.2 Gbps and a phase variation of 3.9276°, the BER of the entire system is decreased. Following that, the maximum data rate rises to 1.4625 Gbps. Additionally, in [50], the authors investigate SVM for evaluating and correcting the phase distortion in two-band and four-order carrier-less amplitude and phase modulation VLC. The obtained results illustrate that phase deviation can be significantly rectified and BER is effectively lowered to 7% with a data rate of 400 Mbps. Further, the conclusions of ML algorithms for phase estimation are illustrated in Table 5.

Table 4: ML algorithms in modulation identification.

Method	Ref.	Outcomes
k-Means algorithms	[18, 19]	(1) [18] Based on postequalization and [19] based on preequalization (2) BER reduced by 10% in [18] and by 50% in [19] (3) Gain improved by a factor of 1.6 dB to 2.5 dB in comparison to linear compensation
GMM	[20]	(1) Can operate on a wide range of bias current and voltage (2) Require more time in execution

Table 5: ML algorithms for phase estimation.

Method	Ref.	Outcomes
k-Means	[25]	(1) Can efficiently improve BER performance (2) Maximum data rate up to 1.4625 Gbps is obtained
GMM	[26]	(1) Low BER than *k*-means (2) Gain is 1 dB higher than *k*-means with 1.5 Gbps bit rate
SVM	[50]	(1) BER can be reduced to 7% with significant correction in phase distortion (2) Data rate up to 400 mbps can be obtained

5. Comparative Analysis

Every ML approach has its own set of benefits and drawbacks. Few are extremely precise, but others are less complicated to calculate. Therefore, the implementation of any particular ML scheme is dependent on the individual's requirements, the application's features, and the availability of the system. e.g., in SL, *k*-NN is a very simple technique that involves a limited number of parameters for proper realisation. Moreover, *k*-NN is not preferred in datasets with a large degree of dimensionality [24]. On the other hand, SVM is found to be appropriate for problems with a large degree of dimensionality and linear differentiability. Furthermore, SVMs' kernel-based approach makes them suitable for nonlinear training datasets even though identifying the right kernel is a challenging process [50]. For lesser amounts of data, the DT technique is recommended. Nevertheless, this method is extremely sensitive to unbalanced datasets, especially if the tree is quite complex. RF, however, accumulates multiple DTs to control imbalancing but at the cost of additional calculation complexity [17]. DNN works exceptionally well in nonlinear and complicated systems. Furthermore, it is capable of working solely with raw information, obviating the need for additional data processing. Moreover, it involves the processing of a high amount of data, making it both complex and time consuming.

USL primarily utilised clustering and dimensionality reduction. The *k*-means is a clustering technique that is quick and simple. Furthermore, the number of centroids in it is predetermined, limiting its flexibility. However, GMM has high flexibility as it is based on prior probability, but the need for parametric optimization causes it to be expensive to enforce [26]. Furthermore, DBSCAN is density-specified clustering and preferred in noisy data points.

Therefore, in VLC, these ML algorithms are used based on their strength and system usability, such as ANN is used in nonlinearity mitigation, channel estimation, and positioning due to its strong nonlinear mapping ability; *k*-NN and algorithms based on multiple classifiers are used in location tracking due to their high precision. Moreover, jitter occurs randomly in a system that can be effectively mitigated by DBSCAN. Clustering is used to estimate phase and modulation for its ability to group unlabelled data. Furthermore, Table 6 represents the most prevalent ML schemes implemented in VLC networks.

6. Future Perspective

In recent times, VLC has yielded a slew of incredible results in 5G era and beyond. Still, there are some major roadblocks in various areas, such as the current optical architecture, which is currently slowing down the VLC network process. As a result, in the coming years, some new design concepts must be investigated in order to reduce system failures. Existing VLC indoor and underwater channels do not take into account the various issues that determine precise channels, so a comprehensive VLC analytical network design is required. It is necessary to implement a VLC-based diverse communication system. ML is a powerful tool which has attracted considerable interest due to its strong i/p-o/p mapping potential, identification, and correlation efficiency. In particular, ML gained special popularity in image and video processing, AI, and certain other sectors, but it is still in its initial stages in VLC [27]. To date, the ML techniques in VLC have not been effectively exploited. In addition, convolutional neural networks (CNNs) are not fully investigated with VLC networks using ML technology as their feature extraction potential as well as their structural channel for VLC are quite complex. Therefore, it will take additional investigation into various ML techniques in order to completely realise the insight of VLC networks.

Table 6: Comparison of various ML schemes.

ML algorithms	Applications	Ref.	Action position	Characteristic parameters
k-NN	Positioning	[14–17]	Receiver	Supervised, moderate complexity
SVM	Phase estimation	[50]	Receiver	Supervised, moderate complexity
ANN and DNN	Nonlinearity mitigation, positioning, and channel estimation	[10, 11, 23, 33, 41, 46, 47]	Receiver	Supervised, high complexity
Multiple classifier	Positioning	[44, 45]	Receiver	Supervised, high complexity
k-Means	Nonlinearity mitigation, positioning, phase estimation, and modulation identification	[18, 19, 25, 26, 42, 43, 53]	Transmitter and receiver both	Unsupervised, low complexity
GMM	Modulation identification and phase estimation	[20, 26]	Receiver	Unsupervised, moderate complexity
DBSCAN	Jitter compensation	[30, 48, 49]	Receiver	Unsupervised, low complexity

Furthermore, some significant open research challenges that can be addressed in the future are stated as follows:

(i) Real-time VLC transmission is a time-dependent process that necessitates datasets and training in a real-time environment. Moreover, in a real-time scenario, the channel behaviour of VLC elements varies with time. The VLC-based ML techniques use offline data training. As a result, the system should be implemented with self-learning, modifying, and optimization capabilities in future applications [51]

(ii) The VLC networks are typically confined in narrow frequency band of luminaries; however, ML of high illumination can be used to minimise the aforesaid constraint [4]

(iii) VLC is primarily used for LoS communication using single set of LED and PD. However, the multiple-input and multiple-output VLC transmission using arrays of LEDs and PDs represent the emerging trends. Additionally, ML applications in multiple-input and multiple-output VLC can enhance the performance [51]

(iv) Another area of investigation in VLC network with ML is channel modelling including different types of indoor surfaces for refraction, reflection and scattering, higher-order nLoS components, geographical illumination dispersion, and noise. As a result, smart ML is a part of future VLC network research to accommodate the aforementioned complexity [27]

(v) ML-based VLC systems mostly use M-PAM ($M = 4$, 8, 16), CAP-MQAM, and CAP-QPSK modulation techniques. Furthermore, since VLC is primarily used for high-speed data transmission, ML with more effective modulation techniques like probabilistic constellation shaping modulation and geometric constellation shaping formats [52] can be implemented to increase the data rate and energy efficiency

(vi) LBS with ML can be efficiently used in Internet of Things- (IoT-) based VLC applications. Appropriate route design is required for a variety of indoor positioning applications that can have a significant impact on QoS. It is considered that ML classification models such as ANN are much more efficient for precise location tracking [39]

7. Conclusion

The various ML algorithms for reducing the computational complexity in indoor VLC transmission, as well as ML applications in different design requirements to increase network performance, have been comprehensively reviewed in this paper. Different ML schemes have their own set of benefits and drawbacks. In real-time situations, the investigator must make reasonable decisions based on individual requirements, investigation features, and equipment availability, including calculation complexity, device nonlinearity, and overhead. On the basis of the available literature, it can be concluded that the ML implementation areas in VLC are still inadequate. Further investigation of ML techniques is required for different real-time VLC application scenarios in the future. This will be beneficial for VLC's future research in 5G and beyond.

Data Availability

Data sharing is not applicable to this article as no new data was created or analysed in this study.

Conflicts of Interest

The authors declare that they have no conflicts of interest.

References

[1] N. Chi, H. Haas, M. Kavehrad, T. D. C. Little, and X. L. Huang, "Visible light communications: demand factors, benefits and opportunities [Guest Editorial]," *IEEE Wireless Communications*, vol. 22, no. 2, pp. 5–7, 2015.

[2] R. Gupta and J. Gupta, "Future generation communications with game strategies: a comprehensive survey," *Computer Communications*, vol. 192, no. 1, pp. 1–32, 2022.

[3] V. N. Saxena, J. Gupta, and V. K. Dwivedi, "Diversity combining techniques in indoor VLC communication," in *2021 IEEE 4th International Conference on Computing, Power and Communication Technologies (GUCON)*, pp. 1–4, Kuala Lumpur, Malaysia, 2021.

[4] N. Chi, J. Jia, F. Hu, Y. Zhao, and P. Zou, "Challenges and prospects of machine learning in visible light communication," *Journal of Communications and Information Networks*, vol. 5, no. 3, pp. 302–309, 2020.

[5] W. S. Saif, M. A. Esmail, A. M. Ragheb, T. A. Alshawi, and S. A. Alshebeili, "Machine learning techniques for optical performance monitoring and modulation format identification: a survey," *IEEE Communications Surveys & Tutorials*, vol. 22, no. 4, pp. 2839–2882, 2020.

[6] M. E. M. Cayamcela, H. Lee, and W. Lim, "Machine learning for 5G/B5G mobile and wireless communications: potential, limitations, and future directions," *IEEE Access*, vol. 7, article 137184, 2019.

[7] C. Zhang, P. Patras, and H. Haddadi, "Deep learning in mobile and wireless networking: a survey," *IEEE Communications Surveys and Tutorials*, vol. 21, no. 3, pp. 2224–2287, 2019.

[8] Y. Fu, S. Wang, C. X. Wang, X. Hong, and S. McLaughlin, "Artificial intelligence to manage network traffic of 5G wireless networks," *IEEE Network*, vol. 32, no. 6, pp. 58–64, 2018.

[9] P. G. Pachpande, M. H. Khadr, A. F. Hussein, and H. Elgala, "Visible light communication using deep learning techniques," in *IEEE 39th Sarnoff Symposium*, pp. 1–6, Newark, NJ, USA, 2018.

[10] A. Yesilkaya, O. Karatalay, A. S. Ogrenci, and E. Panayirci, "Channel estimation for visible light communications using neural networks," in *International Joint Conference on Neural Networks (IJCNN)*, pp. 320–325, Vancouver, BC, Canada, 2016.

[11] W. Xi, Z. Huang, and Y. Ji, "Deep neural network method for channel estimation in visible light communication," *Optics Communications*, vol. 462, article 125272, 2020.

[12] X. Chen and M. Jiang, "Adaptive statistical Bayesian MMSE channel estimation for visible light communication," *IEEE Transactions On Signal Processing*, vol. 65, no. 5, pp. 1287–1299, 2017.

[13] X. Ma, F. Yang, S. Liu, and J. Song, "Channel estimation for wideband underwater visible light communication: a compressive sensing perspective," *Optics Express*, vol. 26, no. 1, pp. 311–321, 2018.

[14] M. T. Van, N. V. Tuan, T. T. Son, H. L. Minh, and A. Burton, "Weighted k-nearest neighbour model for indoor VLC positioning," *IET Communications*, vol. 11, no. 6, pp. 864–871, 2017.

[15] F. Alam, M. T. Chew, T. Wenge, and G. S. Gupta, "An accurate visible light positioning system using regenerated fingerprint database based on calibrated propagation model," *IEEE Transactions on Instrumentation and Measurement*, vol. 68, no. 8, pp. 2714–2723, 2019.

[16] M. Xu, W. Xia, Z. Jia, Y. Zhu, and L. Shen, "A VLC-based 3-D indoor positioning system using fingerprinting and K-nearest neighbor," in *IEEE 85th Vehicular Technology Conference*, pp. 1–5, Sydney, NSW, Australia, 2017.

[17] H. Tran and C. Ha, "Improved visible light-based indoor positioning system using machine learning classification and regression," *Applied Sciences*, vol. 9, no. 6, pp. 1048–1072, 2019.

[18] X. Lu, K. Wang, L. Qiao, W. Zhou, Y. Wang, and N. Chi, "Nonlinear compensation of multi-CAP VLC system employing clustering algorithm based perception decision," *IEEE Photonics Journal*, vol. 9, no. 5, pp. 1–9, 2017.

[19] X. Lu, M. Zhao, L. Qiao, and N. Chi, "Non-linear compensation of multi-CAP VLC system employing pre-distortion base on clustering of machine learning," in *Optical Fiber Communication Conference*, pp. 1–3, 2018.

[20] X. Wu, F. Hu, P. Zou, and N. Chi, "Application of Gaussian mixture model to solve inter-symbol interference in PAM8 underwater visible light system communication," *IEEE Photonics Journal*, vol. 11, no. 6, pp. 1–10, 2019.

[21] Y. Wang, L. Tao, X. Huang, J. Shi, and N. Chi, "8-Gb/s RGBY LED-based WDM VLC system employing high-order CAP modulation and hybrid post equalizer," *IEEE Photonics Journal*, vol. 7, no. 6, pp. 1–7, 2015.

[22] F. N. Khan, Q. Fan, C. Lu, and A. P. T. Lau, "Machine learning methods for optical communication systems and networks," in *Optical Fiber Telecommunications*, pp. 921–978, Academic Press, 2019.

[23] H. Huang, A. Yang, L. Feng, G. Ni, and P. Guo, "Artificial neural-network-based visible light positioning algorithm with a diffuse optical channel," *Chinese Optics Letters*, vol. 15, no. 5, article 050601, 2017.

[24] M. Saadi, T. Ahmad, Y. Zhao, and L. Wuttisttikulkij, "An LED based indoor localization system using kmeans clustering," in *2016 15th IEEE International Conference on Machine Learning and Applications (ICMLA)*, pp. 246–252, Anaheim, CA, USA, 2016.

[25] X. Wu and N. Chi, "The phase estimation of geometric shaping 8-QAM modulations based on K-means clustering in underwater visible light communication," *Optics Communications*, vol. 444, pp. 147–153, 2019.

[26] X. Wu, F. Hu, P. Zou, X. Lu, and N. Chi, "The performance improvement of visible light communication systems under strong nonlinearities based on Gaussian mixture model," *Microwave and Optical Technology Letters*, vol. 62, no. 2, pp. 547–554, 2020.

[27] Z. Ghanem, A. Alsaraira, L. Al-Tarawneh, and O. A. Saraereh, "Comparative analysis of ML-schemes in OWC systems," *Journal of Electrical Engineering and Technology (IJEET)*, vol. 12, no. 8, pp. 115–132, 2021.

[28] X. Wang and J. Shen, "Machine learning and its applications in visible light communication based indoor positioning," in *2019 International Conference on High Performance Big Data and Intelligent Systems (HPBD&IS)*, pp. 274–277, Shenzhen, China, 2019.

[29] Z. Ghassemlooy, W. Popoola, and S. Rajbhandari, *Optical Wireless Communications; System and Channel Modelling with Matlab*, CRC Press, 2013.

[30] X. Lu, Y. Zhou, L. Qiao et al., "Amplitude jitter compensation of PAM-8 VLC system employing time-amplitude two-dimensional re-estimation base on density clustering of machine learning," *Physica Scripta*, vol. 94, no. 5, article 055506, 2019.

[31] P. A. Haigh, Z. Ghassemlooy, H. L. Minh et al., "Exploiting equalization techniques for improving data rates in organic optoelectronic devices for visible light communications," *Journal of Lightwave Technology*, vol. 30, no. 19, pp. 3081–3088, 2012.

[32] H. L. Minh, D. O'Brien, G. Faulkner et al., "100-Mb/s NRZ visible light communications using a postequalized white LED,"

IEEE Photonics Technology Letters, vol. 21, no. 15, pp. 1063–1065, 2009.

[33] X. Li, Q. Gao, C. Gong, and Z. Xu, "Nonlinearity mitigation for VLC with an artificial neural network based equalizer," in *IEEE Globecom Workshops (GC Wkshps)*, pp. 1–6, Abu Dhabi, United Arab Emirates, 2018.

[34] N. Chi, Y. Zhao, M. Shi, P. Zou, and X. Lu, "Gaussian kernel-aided deep neural network equalizer utilized in underwater PAM8 visible light communication system," *Optics Express*, vol. 26, no. 20, pp. 26700–26712, 2018.

[35] C. Chen, X. Deng, Y. Yang, P. Du, H. Yang, and L. Zhao, "LED nonlinearity estimation and compensation in VLC systems using probabilistic Bayesian learning," *Applied Sciences*, vol. 9, no. 13, pp. 2711–2722, 2019.

[36] M. Obeed, A. M. Salhab, M. Alouini, and S. A. Zummo, "Survey on physical layer security in optical wireless communication systems," in *2018 Seventh International Conference on Communications and Networking (ComNet),*, pp. 1–5, Hammamet, Tunisia, 2018.

[37] L. Xiao, G. Sheng, S. Liu, H. Dai, M. Peng, and J. Song, "Deep reinforcement learning-enabled secure visible light communication against eavesdropping," *IEEE Transactions on Communications*, vol. 67, no. 10, pp. 6994–7005, 2019.

[38] M. A. Arfaoui, H. Zaid, Z. Rezki, A. Ghrayeb, A. Chaaban, and M. Alouini, "Artificial noise-based beamforming for the MISO VLC wiretap channel," *IEEE Transactions on Communications*, vol. 67, no. 4, pp. 2866–2879, 2019.

[39] Y. Zhuang, L. Hua, L. Qi et al., "A survey of positioning systems using visible LED lights," *IEEE Communications Surveys & Tutorials*, vol. 20, no. 3, pp. 1963–1988, 2018.

[40] Y. C. Chuang, Z. Q. Li, C. W. Hsu, Y. Liu, and C. W. Chow, "Visible light communication and positioning using positioning cells and machine learning algorithms," *Optics Express*, vol. 27, no. 11, p. 16377, 2019.

[41] W. Sayed, T. Ismail, and K. Elsayed, "A neural network-based vlc indoor positioning system for moving users," in *2019 International Conference on Smart Applications, Communications and Networking (SmartNets)*, pp. 1–6, Sharm El Sheikh, Egypt, 2019.

[42] M. Saadi, T. Ahmad, Y. Zhao, and L. Wuttisttikulkij, "An LED Based indoor localization system using k-means clustering," in *15th IEEE International Conference on Machine Learning and Applications (ICMLA)*, pp. 246–252, Anaheim, CA, USA, 2016.

[43] M. Saadi, Z. Saeed, T. Ahmad, M. K. Saleem, and L. Wuttisittikulkij, "Visible light-based indoor localization using k-means clustering and linear regression," *Transactions on Emerging Telecommunications Technologies*, vol. 30, no. 2, pp. 1–15, 2019.

[44] X. Guo, S. Shao, N. Ansari, and A. Khreishah, "Indoor localization using visible light via fusion of multiple classifiers," *IEEE Photonics Journal*, vol. 9, no. 6, pp. 1–16, 2017.

[45] X. Guo, F. Hu, N. R. Elikplim, and L. Li, "Indoor localization using visible light via two-layer fusion network," *IEEE Access*, vol. 7, pp. 16421–16430, 2019.

[46] T. Yuan, Y. Xu, Y. Wang, P. Han, and J. Chen, "A tilt receiver correction method for visible light positioning using machine learning method," *IEEE Photonics Journal*, vol. 10, no. 6, pp. 1–12, 2018.

[47] M. Polasek and J. Nemecek, "Optical positioning using neural network," in *2018 41st International Conference on Telecommunications and Signal Processing (TSP)*, pp. 1–5, Athens, Greece, 2018.

[48] X. Lu, L. Qiao, Y. Zhou, W. Yu, and N. Chi, "An I-Q-time 3-dimensional post-equalization algorithm based on DBSCAN of machine learning in CAP VLC system," *Optics Communications*, vol. 430, pp. 1–7, 2019.

[49] W. X. Yu, X. Y. Lu, and N. Chi, "Signal decision employing density-based spatial clustering of machine learning in PAM-4 VLC system," *Proceedings of SPIE*, vol. 7, pp. 1354–1363, 2018.

[50] W. Niu, Y. Ha, and N. Chi, "Novel phase estimation scheme based on support vector machine for multiband-CAP visible light communication system," in *Asia Communications and Photonics Conference*, pp. 1–3, 2018.

[51] N. Chi, Y. Zhou, Y. Wei, and F. Hu, "Visible light communication in 6G: advances, challenges, and prospects," *IEEE Vehicular Technology Magazine*, vol. 15, no. 4, pp. 93–102, 2020.

[52] Z. Qu and I. B. Djordjevic, "Optimal constellation shaping in optical communication systems," in *20th International Conference on Transparent Optical Networks (ICTON*, pp. 1–5, Bucharest, Romania, 2018.

[53] J. Ma, J. He, J. Shi, J. He, Z. Zhou, and R. Deng, "Nonlinear compensation based on K-means clustering algorithm for Nyquist PAM-4 VLC system," *IEEE Photonics Technology Letters*, vol. 31, no. 12, pp. 935–938, 2019.

Hindawi
Wireless Communications and Mobile Computing
Volume 2022, Article ID 2697932, 9 pages
https://doi.org/10.1155/2022/2697932

Research Article

ResNet-Enabled cGAN Model for Channel Estimation in Massive MIMO System

Jyoti Deshwal Yadav, Vivek K. Dwivedi, and Saurabh Chaturvedi

Department of Electronics and Communication Engineering, Jaypee Institute of Information Technology, Noida 201309, India

Correspondence should be addressed to Saurabh Chaturvedi; saurabh.chaturvedi@jiit.ac.in

Received 22 April 2022; Revised 8 July 2022; Accepted 5 August 2022; Published 29 August 2022

Academic Editor: Abdul Basit

Massive multiple-input multiple-output (MIMO), or large-scale MIMO, is one of the key technologies for future wireless networks to exhibit a large accessible spectrum and throughput. The performance of a massive MIMO system is strongly reliant on the nature of various channels and interference during multipath transmission. Therefore, it is important to compute accurate channel estimation. This paper considers a massive MIMO system with one-bit analog-to-digital converters (ADCs) on each receiver antenna of the base station. Deep learning (DL)-based channel estimation framework has been developed to reduce signal processing complexity. This DL framework uses conditional generative adversarial networks (cGANs) and various convolutional neural networks, namely reverse residual network (reverse ResNet), squeeze-and-excitation ResNet (SE ResNet), ResUNet++, and reverse SE ResNet, as the generator model of cGAN for extracting the features from the quantized received signals. The simulation results of this paper show that the trained residual block-based generator model of cGAN has better channel generation performance than the standard generator model in terms of mean square error.

1. Introduction

The frequency of wireless data traffic has increased dramatically worldwide during the last few decades [1]. This scenario puts considerable pressure on the current wireless communication system. The instant increase in the demand for several laptops and smart devices, the prevalence of online gaming and social networking, and the high-demand services like interactive media led to an outburst in cellular network data traffic, with demands projected to rise continuously at a rapid rate [2, 3]. As per Cisco's visual networking index forecast, the global mobile data traffic increased approximately ten-fold from 2013 to 2018 [4]. By the end of 2022, most of the traffic will be derived from mobile phones. The previous wireless generation systems were not able to manage this enormous amount of data. This scenario has motivated the consideration of a wireless technology known as multiple-input multiple-output (MIMO), both in theory and practice [5]. MIMO technology uses multiple antennas for a considerable improvement in spectral efficiency. This technology is divided into three parts: point-to-point MIMO, multiuser MIMO, and massive MIMO [6]. The point-to-point MIMO is the simplest form of MIMO in which a base station (BS) equipped with an antenna array serves a terminal equipped with an antenna array [6]. In multiuser MIMO, the array of terminals using the same time-frequency resources is served by a single base station [7]. This scenario comes from a point-to-point MIMO setup by splitting the K-antenna terminal into multiple separate terminals. The massive MIMO is a scalable version of multiuser MIMO. It is also called the extension of MIMO technology, which includes hundreds and even thousands of antennas at the BS to enhance the throughput and energy efficiency [8]. The underlying idea that allows for a considerable gain in energy efficiency is that energy can be absorbed with high intensity into smaller areas when a large number of antennas are used [9]. By utilizing the multiplexing gains and spatial diversity, massive MIMO improves the robustness and spectral efficiency of wireless communication systems under limited channel fading and bandwidth [10]. The issues associated with practical massive MIMO systems are the high power consumption and expensive

hardware. The utilization of analog-to-digital converters (ADCs) is one of the promising solutions for this issue. The power transmitted by these complex ADCs is inversely proportional to the number of antennas [11]. The power consumed by each ADC increases exponentially with the number of quantization bits and linearly with the sampling rate [12, 13]. Therefore, low-resolution one-bit ADCs are considered for a massive MIMO system.

In a one-bit massive MIMO system, deep learning (DL) techniques are being applied to empower its full potential [14]. The influence of DL techniques grew rapidly in early 2000s. DL is a subset of machine learning (ML) that makes use of neural networks and utilizes supervised, unsupervised, and reinforcement learning [15]. DL is used in a number of domains, including automatic speech recognition, object detection, and image classification. It is also used in many wireless communication applications, such as resource management, spectral sensing, beamforming, signal detection, and channel estimation [16–18]. Using the DL techniques, a task can be analyzed easily and with reliable results. In [19], DL techniques have been successfully used for signal detection with nonlinear distortion and joint channel estimation. In [20], a deep convolutional neural network (CNN) has been used to explore channel correlation and improve the channel estimation accuracy. DL approaches can also be used to solve the beam selection problem in massive MIMO systems [21].

In [22], a DL technique was used to estimate the channel for one-bit massive MIMO system. By using this DL technique, it is difficult to generate a more realistic channel matrix because of information loss with subsequent layers in neural networks [22]. This paper employs the same DL technique used in [22] with different CNN architectures to generate more realistic and accurate channels for one-bit massive MIMO system.

The performance of the proposed approach is measured in terms of mean square error (MSE) and the number of used BS antennas. The conditional generative adversarial network (cGAN) is a form of GAN that is used to determine an adaptive loss function, called GAN loss, for variety datasets and applications. The learning curves for the generator and discriminator models of all the cGAN versions are also tracked and estimated. The following are the main contributions of this paper: The reverse residual network (reverse ResNet), squeeze-and-excitation ResNet (SE ResNet), ResU-Net++, and reverse SE ResNet versions of the ResNet architecture are successfully implemented as a generator model of cGAN, and their performance is compared in terms of MSE and the number of BS antennas used. The learning curves of the generator and discriminator models are also examined. The learning curves show that both the generator and discriminator are following their adversarial property, indicating that the training scheme is working properly. However, after upgrading the ResNet to its variants, the discriminator may need to be upgraded as well to keep up with the more powerful generator. The results exhibit that for channel estimation, the cGAN with reverse SE ResNet as a generator model outperforms the other techniques. The rest of this paper is structured as follows: The architecture of a one-bit massive MIMO system is described in Section 2. The characteristics of DL models and channel estimation using cGAN are discussed in Section 3. The simulation results are presented and compared in Section 4. Finally, Section 5 concludes the paper.

2. Architecture of One-Bit Massive MIMO System

In a basic massive MIMO setup, each BS is equipped with a large number of antennas and serves a cell with a large number of users. Each user is considered as a single antenna. All users simultaneously occupy the full time-frequency resources both in uplink and downlink transmissions. On the BS and user sides, an uplink massive MIMO system with a uniform linear array (ULA) is considered. As shown in Figure 1, there are M BS antennas and K single-antenna mobile users (MUs). Each antenna at BS is equipped with two one-bit ADCs for real and imaginary components of the signal received from each MU antenna. By following the channel model of [22], the channel matrix for the K MUs can be expressed by

$$h_k = \sum_{l=1}^{N_\rho} \omega_l a\left(\beta_{\text{azi}}^k, \beta_{\text{aod}}^k\right), \tag{1}$$

where l is the channel path, N_ρ is the number of channel paths, the complex gain of each path l is ω_l, and $a(.)$ denote the array response vector of the BS. β_{azi}^k and β_{aod}^k denote the azimuth angle of departure and elevation angle of departure, respectively. Finally, the full channel matrix H for K MUs can be expressed by (2), where the dimension of H is $M \times K$:

$$H = [h_1, h_2, .. \cdots \cdots, h_k, .. \cdots \cdots, h_K]. \tag{2}$$

2.1. Applying One-Bit ADCs for Channel Estimation. The channel is estimated at the BS by using a pilot sequence of length τ from the user side. As shown in Figure 1, K MUs concurrently transmit the pilot sequence of length τ to BS. The received signal Y at the BS before one-bit quantization is given by [22]:

$$\mathrm{Y} = H\phi + N, \tag{3}$$

where the dimension of Y is $\mathrm{M} \times \tau$, N is a noise matrix whose dimension is $M \times \tau$, and ϕ is the randomly assigned pilot sequence from K users. During the quantization process, the real and imaginary components of a signal from BS antennas are separately quantized using one-bit ADC. The function used for quantization is signum function sgn(.). After one-bit quantization, the received signal Y can be expressed by [22]

$$Y = \text{sgn}\,(H\phi + N), \tag{4}$$

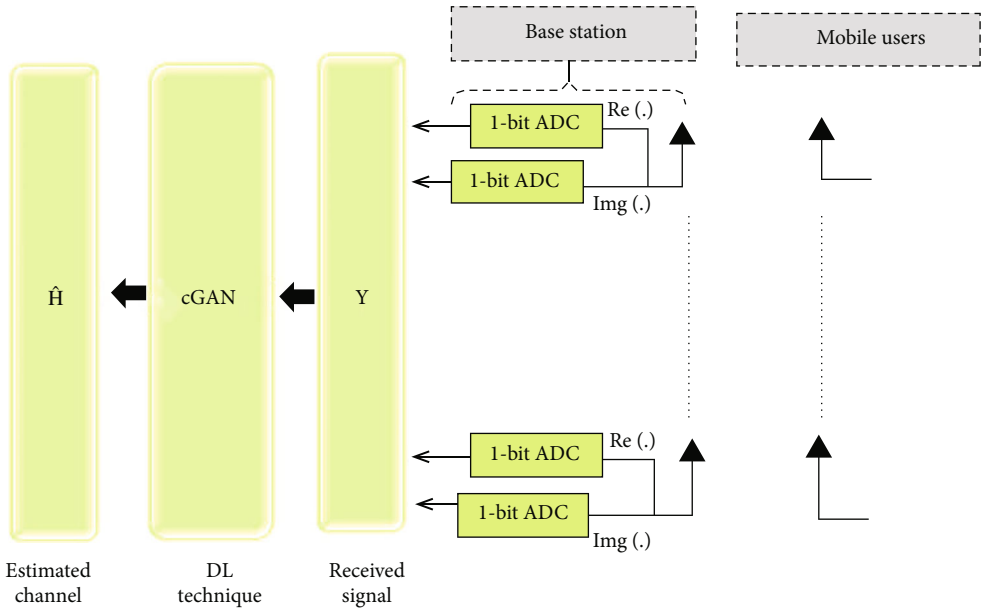

Figure 1: Architecture of one-bit massive MIMO system.

where sgn(.) is

$$\text{sgn} = \begin{cases} 1 \text{ for } x \geq 0, \\ -1, \text{ otherwise.} \end{cases} \tag{5}$$

The quantized signal Y takes the values from the set $\{1+j, 1-j, -1+j, -1-j\}$. The goal of this research is to use an adversarial DL model to extract the channel matrix $\hat{H}$ from the quantized received signal Y, as well as to evaluate their performance in terms of MSE and the number of BS antennas employed.

3. Channel Estimation Using cGAN

In this section, CNN-based cGAN has been used to perform the channel estimation tasks. In this work, the channel estimation is considered as an image-to-image translation problem by considering channel matrix H and received signal Y as two channel images with parameters of $M \times N \times 2$ and $M \times \tau \times 2$, respectively. Here two channels signify the real and imaginary part of the complex matrix.

3.1. cGAN Architecture. The standard GAN is composed of two neural networks, namely generator G and discriminator D. As shown in Figure 2, G learns the data distribution from the original dataset and generates new images [23]. The G is trained to improve the quality of generated data to fool the discriminator, so that generated samples produced by G are considered real ones, and the D is trained to differentiate between generated and real samples. If D can successfully differentiate between the generated and real samples, then G will receive feedback based on D's success, so that G can learn to generate samples similar to the real ones. Both networks work against each other to achieve the best results [22]. To achieve this goal, the cGAN loss is composed of two parts: the adversarial loss and the $L1$ loss [24]. The adversarial loss can be expressed by

$$L_{\text{cGAN}}(G, D, Y, H) = \min_G \max_D \mathbb{E}[\log D(H)] + \mathbb{E}[\log(1 - D(G(Y)))]. \tag{6}$$

The expression of $L1$ loss is given by

$$L_1 = \left(\mathbb{E}\left[\|H - G(Y)\|^2\right]\right). \tag{7}$$

Here L_1 distance is added to the generator loss to encourage the low-frequency accuracy of the generated image. The L_1 distance is preferred over L_2 distance because it produces images with less blurring. Finally, the complete expression for the cGAN loss is given by [22]

$$L_{\text{cGAN}}(G, D, Y, H) = \min_G \max_D \mathbb{E}[\log D(H)] + \mathbb{E}[\log(1 - D(G(Y)))] + \lambda L_1(G). \tag{8}$$

The architecture of G and D neural networks must be carefully chosen in order to make training easier [25].

3.2. Proposed CNN Architectures for G Model of cGAN. In this paper, a cGAN architecture is used to create artificial channel samples in a one-bit massive MIMO system illustrated in Figure 3. To make the training process easier, the architecture for the G model must be chosen carefully [26]. After conducting a thorough model exploration for the G model and taking into account prior findings [22, 27], a few ResNet variant architectures have been applied to the G model in this work, and the learning curves of the G and D models have also been analyzed to verify the proper functionality of training scheme. In the cGAN model, both

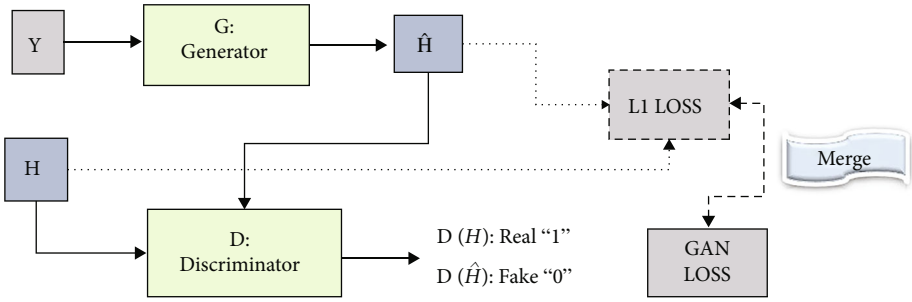

Figure 2: Learning framework of cGAN.

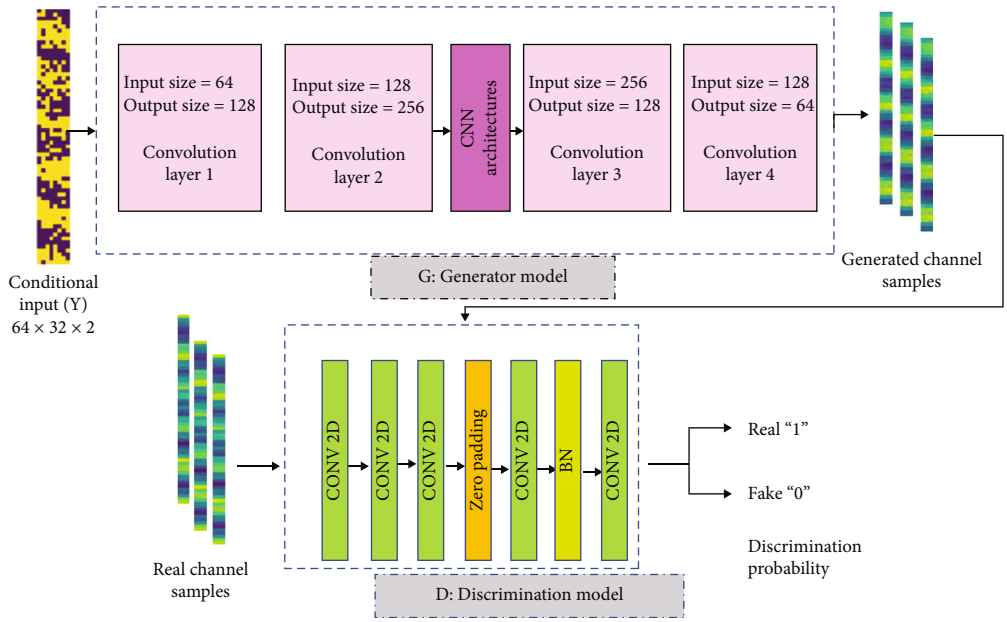

Figure 3: Proposed cGAN architecture for channel estimation in one-bit massive MIMO system.

G and D using CNN architectures are composed of many convolutional layers, batch normalization (BN) layers, activation functions, and dropout layers. The first CNN architecture implemented for the G model of cGAN in this paper is reverse ResNet [26] for channel estimation. As depicted in Figure 4, the order of BN layer, activation function, and convolution layer in the residual block of ResNet described in [28] was changed from Conv-BN-ReLU to BN-ReLU-Conv in this CNN architecture. This modified architecture of ResNet, i.e., reverse ResNet, trains faster and achieves better results than ResNet [28]. The second CNN architecture implemented for the cGAN G model in this paper is SE ResNet, in which an SE block is added to ResNet to perform feature recalibration.

In the SE ResNet architecture, SE block is used after each residual block in order to improve the network's representation [29]. As demonstrated in Figure 5, the global average pooling layer is used for the squeeze phase to minimize the overfitting by reducing the total number of parameters in the model, and two fully connected layers are used for the excitation phase to fine-tune the obtained features for precise channel estimation in the SE block following a channel-wise scaling operation. The third ResNet variant implemented for the cGAN G model in this paper is ResUNet++ [30]. A few modifications have been done in this CNN architecture to make it less complex. The output of each SE ResNet block is concatenated with its corresponding layer in the decoder. ResUNet++ is based on the ResUNet architecture that was presented in [27] for channel estimation. The ResUNet++ architecture takes advantage of both the residual and SE blocks in the U-Net CNN architecture [31]. A residual block spreads information across layers and reduces the vanishing gradient problem, while an SE block performs the feature recalibration [32]. Figure 6 depicts the block diagram of modified ResUNet++ architecture. In the modified ResUNet++ architecture, the encoder uses the SE block with residual block, whereas the decoder uses a sequence of deconvolution, BN, dropout, and concatenation with the SE ResNet through skip connections [32].

Reverse SE ResNet is the fourth CNN architecture used in this paper for the G model of cGAN. As shown in Figure 7, this CNN architecture combines reverse ResNet and SE ResNet. Because of the reverse ResNet and the SE ResNet, this combination allows for faster training and better feature calibration.

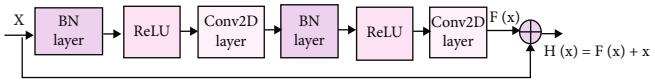

Figure 4: Reverse ResNet architecture for G model of cGAN.

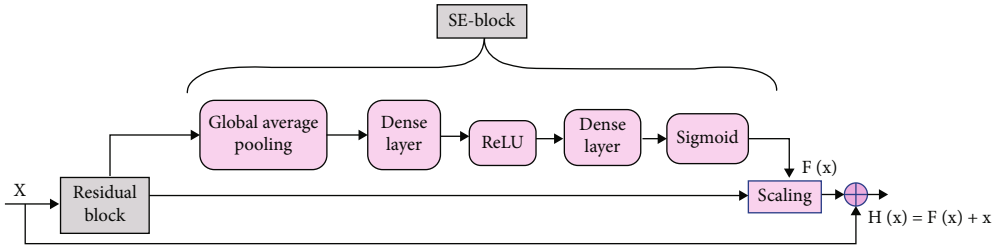

Figure 5: SE ResNet architecture for G model of cGAN.

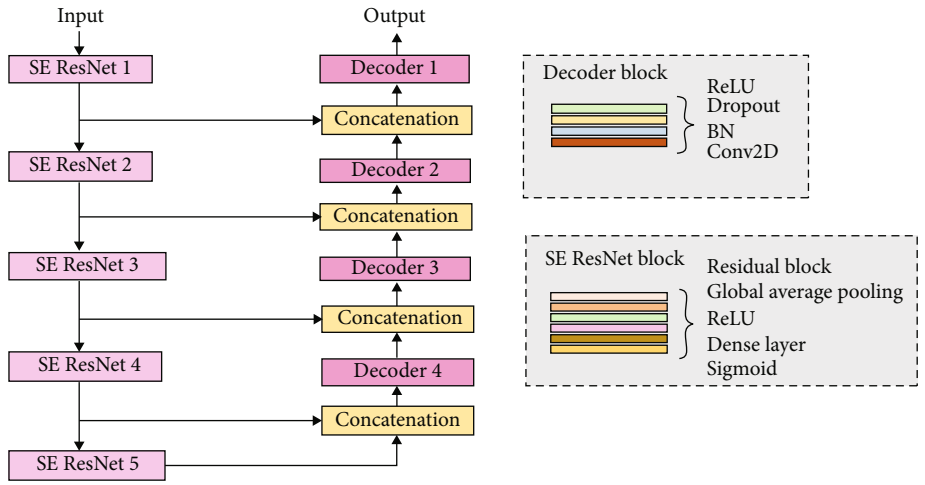

Figure 6: ResUNet++ architecture for G model of cGAN.

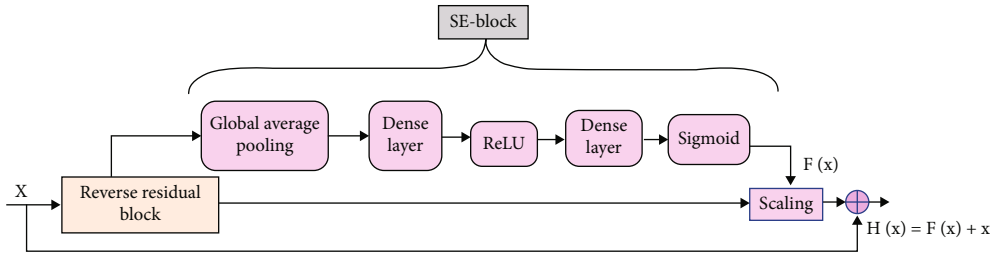

Figure 7: Reverse SE ResNet architecture for G model of cGAN.

3.3. Discriminator Model Architecture. The PatchGAN architecture [24] has been used for the D model in this paper. As reported in [24], the PatchGAN discriminator takes individual patches of an image rather than the entire image and classifies them separately as real and fake, which encourages sharp and high-frequency details of an image. The cGAN D model has two-dimensional convolutional layers with a kernal size of 4, BN layers, and ReLU activation function. The advantage of adopting PatchGAN is that the image size is unrestricted, as well as the image resolution and texture structures are unaffected [33].

4. Simulation Results

4.1. Datasets and Model Training. In this paper, an indoor massive MIMO scenario "I1_2p4" of [34] has been considered for channel estimation using cGAN in one-bit massive MIMO system. In this scenario, there is a $10\text{m} \times 10\text{m}$ dimensional room with two tables.

Users are arranged on x-y grids and antennas are placed on up part of the ceiling. A dataset is generated by taking this scenario, called the DeepMIMO dataset. The parameters for channel simulation are listed in Table 1. Moreover, four

Table 1: Parameters for simulation.

Antenna array type	ULA
Bandwidth (BW)	0.01 GHz
Antenna spacing	BW/2
Total paths	10

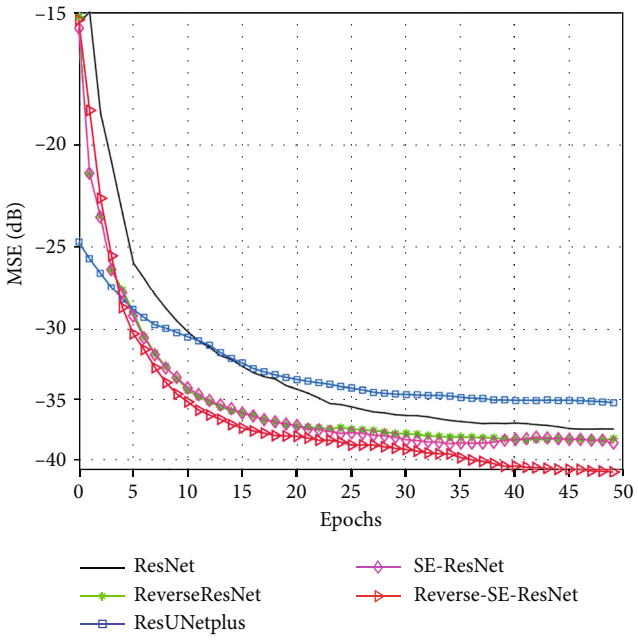

Figure 8: Model comparison in terms of MSE.

channel datasets are generated with different number of BS antennas; M varies from 64 to 256, and the number of MUs is fixed to $K = 32$. For the training and testing purposes, the generated DeepMIMO dataset components were shuffled and distributed in the ratio of 70% and 30%, respectively [35]. To train the G model of cGAN, the Adam optimization algorithm [36] with a learning rate of 2×10^{-4} has been used. The RMSProp algorithm [37] has been adopted with a learning rate of 2×10^{-5} for stable training of the D model.

4.2. Matrices Estimation. This paper makes the use of MSE to compute the variation between the actual channel matrix and the estimated channel matrix. The MSE is expressed by [22]

$$\text{MSE} = 10 \log_{10}\{\mathbb{E}[H - \widehat{H}]2\}, \tag{9}$$

where H and $\widehat{H}$ are the vectors to represent the actual channel matrix and estimated channel matrix over all antennas. $\mathbb{E}[.]$ calculates values of expectation.

4.3. Performance Comparison. In this paper, the cGAN G model has been implemented using four variants of ResNet architecture, namely reverse ResNet, SE ResNet, ResUNet++, and reverse SE ResNet for channel estimation in one-bit massive MIMO system, and their performance is compared

Table 2: Performance comparison of cGAN models.

CNN architecture for G model of cGAN	Minimum MSE (dB)
ResNet	-37.2479
Reverse ResNet	-38.0479
ResUNet++	-35.0092
SE ResNet	-37.9267
Reverse SE ResNet	-40.1313

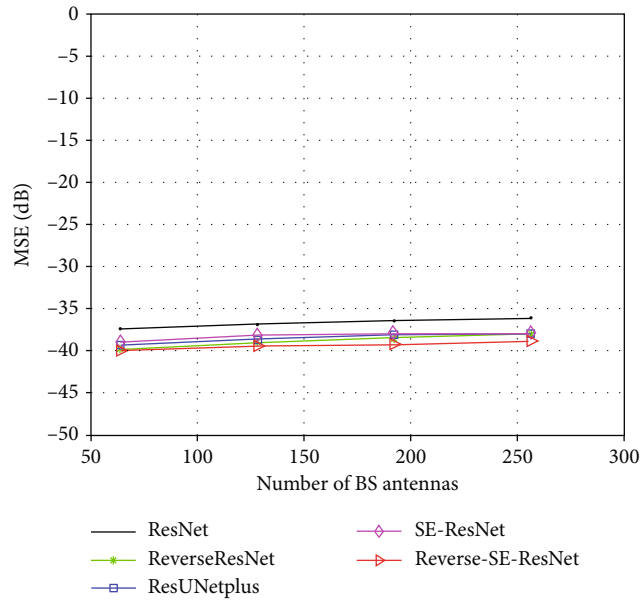

Figure 9: Model performance comparison by varying the number of BS antennas.

with the cGAN G model implemented with ResNet architecture [28] and U-Net architecture [29]. Figure 8 and Table 2 exhibit the performance comparison in terms of MSE. As shown, the cGAN G model with reverse SE ResNet architecture outperforms the remaining cGAN models. The cGAN G model based on reverse SE ResNet is capable of producing better channel estimation results than that of other models because an SE block performs feature recalibration through which a network can learn to use global data to selectively highlight the essential features and suppress the nonessential ones.

Moreover, by reversing the residual block, the model trains faster and achieves better results than the results of original residual block. As depicted in Figure 9, the MSE performance is compared by varying the number of BS antennas and setting the pilot sequence length to 8 and the number of MUs to 32. It can be observed that the MSE value of all cGAN models increases a bit when the number of BS antennas is increased from 64 to 256. The MSE value of cGAN G model with reverse SE ResNet architecture stays in the range from -40 dB to -39 dB. There is no noticeable improvement in MSE for all the G models by increasing the number of BS antennas from 64 to 256. Figures 10 and

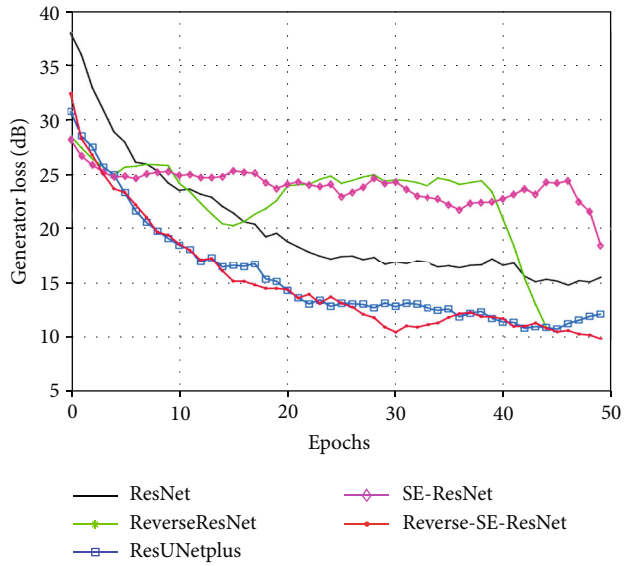

Figure 10: Comparison of the G training curves of all cGAN models.

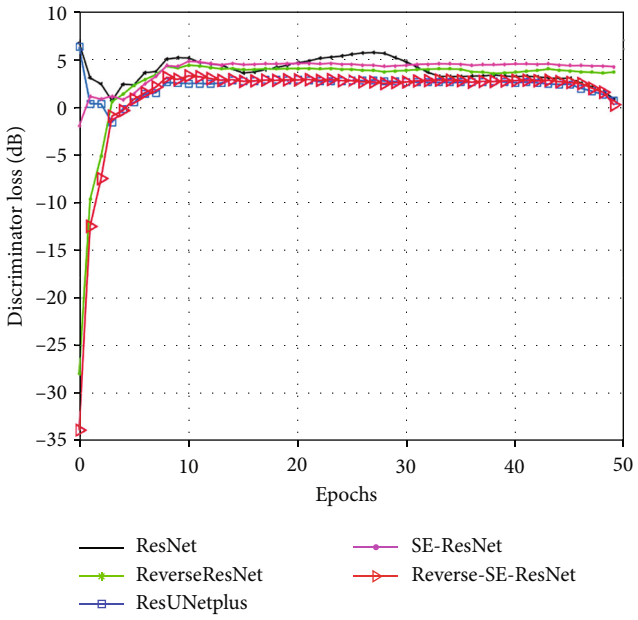

Figure 11: Comparison of the D training curves of all cGAN models.

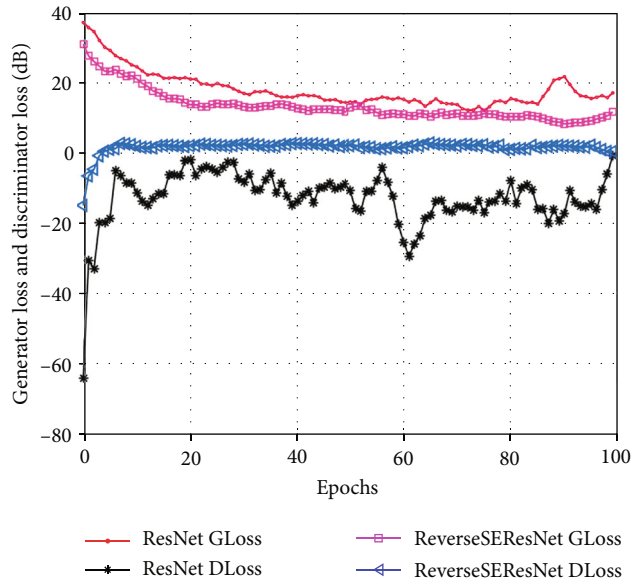

Figure 12: Comparison of the G and D losses.

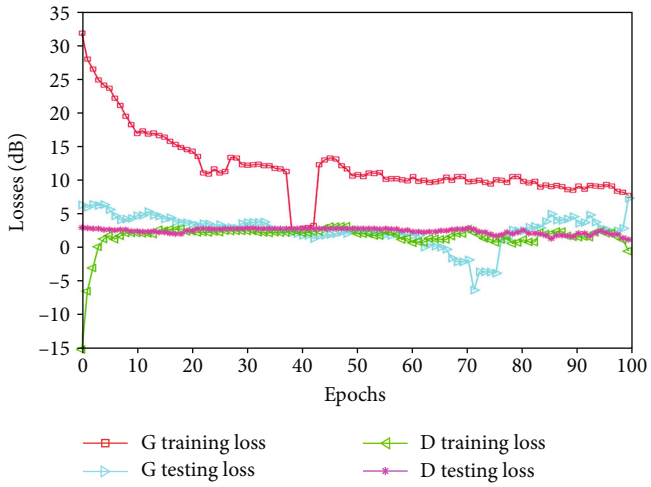

Figure 13: Comparing the training and testing losses of generator and discriminator of cGAN.

11 demonstrate the training curves of the cGAN G and D models. It appears that balancing the convergence of both G and D is extremely difficult. When one of them is over trained, the system becomes unstable. It is observed that G performs poorly in beginning epochs and improves with subsequent epochs, but D performs well in initial epochs because D can quickly distinguish between a real and a fake one. As shown in Figure 12, the training curves of cGAN G model using ResNet and reverse SE ResNet CNN architectures are compared with the training curves of cGAN D model. With subsequent epochs, the training curves of both the G and D models converge. Figure 12 depicts the adversarial property of cGAN. As can be seen, finding a reasonable gradient to follow during training for the G model in the early epochs is challenging; therefore, the G loss is fairly random. The G eventually improves, but it still does not converge properly as shown in Figure 12.

The user's traffic and mode collapse in cGAN are two possible explanations of this convergence failure. Both the G and D models are trying to minimize their own loss function. It is also clear from Figure 12 that the same cGAN model performs differently with different G models, and the strength of D varies in proportion to the strength of G. Lastly, the training and testing losses of cGAN G and D models are compared in Figure 13. As shown in Figure 13, there is a large gap between the G's training and testing losses, but only a small gap between the D's training and testing losses. It can be concluded that cGAN performance

with testing data is better and satisfactory while performing channel estimation for massive MIMO systems.

5. Conclusion

In this paper, the cGAN generator models have been implemented using different CNN architectures, including reverse ResNet, SE ResNet, SE ResNet, ResUNet++, and reverse SE ResNet, and their performances have been compared in terms of MSE for channel estimation. As shown in the simulation results, a cGAN model with a reverse SE ResNet generator and a PatchGAN discriminator can be used to estimate channels precisely. The cGAN discriminator model can be developed with reverse SE ResNet CNN architecture and compared in future work to gain better results for channel estimation. Furthermore, other GAN models, such as deep convolutional GAN and cycle GAN, can also be proposed and used instead of cGAN for channel estimation in a one-bit massive MIMO system.

Data Availability

The underlying data supporting the results may be made available on request.

Conflicts of Interest

The authors declare that they have no conflicts of interest.

References

[1] R. Chataut and R. Akl, "Massive MIMO systems for 5G and beyond networks-overview, recent trends, challenges, and future research direction," *Sensor*, vol. 20, no. 10, p. 2753, 2020.

[2] P. Sabeti, A. Farhang, I. Macaluso, N. Marchetti, and L. Doyle, "Blind channel estimation for massive MIMO: a deep learning assisted approach," in *IEEE International Conference on Communications*, pp. 1–6, Dublin, Ireland, 2020.

[3] A. Khansefid and H. Minn, "On channel estimation for massive MIMO with pilot contamination," *IEEE Communications Letters*, vol. 19, no. 9, pp. 1160–1163, 2015.

[4] H. Papadopoulos, C. Wang, O. Bursalioglu, X. Hou, and Y. Kishiyama, "Massive MIMO technologies and challenges towards 5G," *IEICE Transactions on Communications*, vol. -E99.B, no. 3, pp. 602–621, 2016.

[5] L. Fan, S. Jin, C.-K. Wen, and H. Zhang, "Uplink achievable rate for massive MIMO systems with low-resolution ADC," *IEEE Communication Letter*, vol. 19, no. 12, pp. 2186–2189, 2015.

[6] T. Marzetta, E. Larsson, H. Yang, and H. Ngo, *Introduction in Fundamentals of Massive MIMO*, Cambridge University Press, 2016.

[7] E.-G. Larsson, O. Edfors, F. Tufvesson, and T.-L. Marzetta, "Massive MIMO for next generation wireless systems," *IEEE Communications Magazine*, vol. 52, no. 2, pp. 186–195, 2014.

[8] H. Halbauer, A. Weber, D. Wiegner, and T. Wild, "Energy efficient massive MIMO array configurations," in *2018 IEEE Globecom Workshops (GC Wkshps)*, pp. 1–6, Abu Dhabi, United Arab Emirates, 2018.

[9] D. Muirhead, M.-A. Imran, and K. Arshad, "A survey of the challenges, opportunities and use of multiple antennas in current and future 5G small cell base stations," *IEEE Access*, vol. 4, pp. 2952–2964, 2016.

[10] D. Borges, P. Montezuma, R. Dinis, and M. Beko, "Massive MIMO techniques for 5G and beyond-opportunities and challenges," *Electronics*, vol. 10, no. 14, p. 1667, 2021.

[11] C. Kong, A. Mezghani, C. Zhong, A.-L. Swindlehurst, and Z. Zhang, "Multipair massive MIMO relaying systems with one-bit ADCs and DACs," *IEEE Transactions on Signal Processing*, vol. 66, no. 11, pp. 2984–2997, 2018.

[12] Z. Xiao, J. Zhao, T. Liu, L. Geng, F. Zhang, and J. Tong, "On the energy efficiency of massive MIMO systems with low-resolution ADCs and lattice reduction aided detectors," *Symmetry*, vol. 12, no. 3, p. 406, 2020.

[13] S. Jacobsson, G. Durisi, M. Coldrey, U. Gustavsson, and C. Studer, "Throughput analysis of massive MIMO uplink with low-resolution ADCs," *IEEE Transactions on Wireless Communications*, vol. 16, no. 6, pp. 4038–4051, 2017.

[14] M. B. Mashhadi and D. Gündüz, "Deep learning for massive MIMO channel state acquisition and feedback," *Journal Indian Institute of Science*, vol. 100, no. 2, pp. 369–382, 2020.

[15] A. Ly and Y.-D. Yao, "A review of deep learning in 5G research: channel coding, massive MIMO, multiple access, resource allocation, and network security," *IEEE Open Journal of the Communications Society*, vol. 2, pp. 396–408, 2021.

[16] J. Gao, M. Hu, C. Zhong, G.-Y. Li, and Z. Zhang, "An attention-aided deep learning framework for massive MIMO channel estimation," *IEEE Transactions on Wireless Communications*, vol. 21, no. 3, pp. 1823–1835, 2022.

[17] M. Meenalakshmi, S. Chaturvedi, and V. K. Dwivedi, "Performance analysis of polar codes in 5G new radio," in *International Conference on Signal Processing and Communication*, pp. 96–99, Noida, India, 2021.

[18] M. Meenalakshmi, S. Chaturvedi, and V. K. Dwivedi, "Deep learning techniques for OFDM systems," *IETE Journal of Research*, pp. 1–15, 2021.

[19] Y. Zhang, M. Alrabeiah, and A. Alkhateeb, "Deep learning for massive MIMO with 1-bit ADCs: when more antennas need fewer pilots," *IEEE Wireless Communication Letter*, vol. 9, no. 8, pp. 1273–1277, 2020.

[20] E. Balevi and J. G. Andrews, "Two-stage learning for uplink channel estimation in one-bit massive MIMO," in *Asilomar Conference on Signals, Systems, and Computers*, pp. 1764–1768, Pacific Grove, CA, USA, 2020.

[21] M. Kim, W. Lee, and D.-H. Cho, "Deep scanning-beam selection based on deep reinforcement learning in massive MIMO wireless communication system," *Electronics*, vol. 9, 2020.

[22] Y. Dong, H. Wang, and Y.-D. Yao, "Channel estimation for one-bit multiuser massive MIMO using conditional GAN," *IEEE Communications Letters*, vol. 25, no. 3, pp. 854–858, 2021.

[23] A. A. Al-Shargabi, J. F. Alshobaili, A. Alabdulatif, and N. Alrobah, "COVID-CGAN: efficient deep learning approach for COVID-19 detection based on CXR images using conditional GANs," *Applied Sciences*, vol. 11, no. 16, p. 7174, 2021.

[24] K. Lata, M. Dave, and K.-N. Nishanth, "Image-to-image translation using generative adversarial network," in *International conference on Electronics, Communication and Aerospace Technology*, pp. 186–189, Coimbatore, India, 2019.

[25] E. Balevi, A. Doshi, and J.-G. Andrews, "Massive MIMO channel estimation with an untrained deep neural network," *IEEE*

Transactions on Wireless Communications, vol. 19, no. 3, pp. 2079–2090, 2020.

[26] E. Balevi and J.-G. Andrews, "Wideband channel estimation with a generative adversarial network," *IEEE Transactions on Wireless Communications*, vol. 20, no. 5, pp. 3049–3060, 2021.

[27] J. D. Yadav, V. K. Dwivedi, and S. Chaturvedi, "Performance comparison of cGAN models for channel estimation in one-bit massive MIMO system," in *IEEE Microwave Theory and Techniques in Wireless Communications*, pp. 296–300, Riga, Latvia, 2021.

[28] S. Zagoruyko and N. Komodakis, "Wide residual networks," 2016, https://arxiv.org/abs/1605.07146.

[29] J. Hu, L. Shen, and G. Sun, "Squeeze-and-excitation networks," in *Conference on Computer Vision and Pattern Recognition*, pp. 7132–7141, Salt Lake City, UT, USA, 2018.

[30] D. Jha, D. Johansen, T.-D. Lange, P. Halvorsen, and M.-A. Riegler, "A comprehensive study on colorectal polyp segmentation with ResUNet++, conditional random field and test-time augmentation," *IEEE Journal of Biomedical and Health Informatics*, vol. 25, no. 6, pp. 2029–2040, 2021.

[31] O. Ronneberger, P. Fischer, and T. Brox, "U-Net: convolutional networks for biomedical image segmentation," in *International Conference on Medical Image Computing and Computer-Assisted Intervention*, pp. 234–241, Munich, Germany, 2015.

[32] F.-I. Diakogiannis, F. Waldner, P. Caccetta, and C. Wu, "ResUNet-a: a deep learning framework for semantic segmentation of remotely sensed data," *ISPRS Journal of Photogrammetry and Remote Sensing*, vol. 162, pp. 94–114, 2020.

[33] Y. Zhou, K. Yu, M. Wang et al., "Speckle noise reduction for OCT images based on image style transfer and conditional GAN," *IEEE Journal of Biomedical and Health Informatics*, vol. 26, no. 1, pp. 139–150, 2022.

[34] A. Alkhateeb, "DeepMIMO: a generic deep learning dataset for millimeter wave and massive MIMO applications," in *Information Theory and Applications Workshop*, pp. 1–8, San Diego, USA, 2019.

[35] E. Balevi, A. Doshi, A. Jalal, A. Dimakis, and J.-G. Andrews, "High dimensional channel estimation using deep generative networks," *IEEE Journal on Selected Areas in Communications*, vol. 39, no. 1, pp. 18–30, 2021.

[36] D.-P. Kingma and J.-L. Ba, *Adam: A Method for Stochastic Optimization*, International Conference on Learning Representations, 2015.

[37] S. Ruder, "An overview of gradient descent optimization algorithms," 2016, https://arxiv.org/abs/1609.04747.

Hindawi
Wireless Communications and Mobile Computing
Volume 2022, Article ID 9168945, 8 pages
https://doi.org/10.1155/2022/9168945

Research Article

Capacity Optimization of MISO System in Intercell Interference of Visible Light Communication System

Agha Yasir Ali,[1] **Abdeldime M. S. Abdelgader**,[2] **Lubna Farhi**,[1] **Umm E. Laila**,[1] **and Shujun Wang**[3]

[1]*Sir Syed University of Engineering and Technology Karachi, Pakistan*
[2]*Karary University, 12304, Sudan*
[3]*West Anhui University, Nanjing, China*

Correspondence should be addressed to Abdeldime M. S. Abdelgader; abdeldime@karary.edu.sd

Received 20 March 2022; Revised 21 July 2022; Accepted 3 August 2022; Published 26 August 2022

Academic Editor: Ghanshyam Singh

The capacity of multiple input and single out (MISO) system is investigated in intercell interference environment of a visible light communication (VLC) system. The interference is dominating in cell edges and the center of the room due to overlapping of light signals from neighbor cell. The footprint of one cell extends at high SNR, and consequently, this increases the intercell interference regions. Therefore, the channel capacity is greatly deteriorated due to interference power. In this paper, the channel capacity can be improved using diversity gain of MISO-based VLC system. The light-emitting diode (LEDs) of MISO system in a cell can use the same data to improve the diversity gain of the system. The MISO array is derived as per SNR requirements in interference region of the room. The capacity of the MISO system is examined and compared with that of the single input and single output (SISO). A trade-off of the MISO array is obtained at different SNRs to achieve the interference free capacity system. Theoretical and simulation capacity response show that the interference is considerably minimized by using diversity gain of MISO system. The interference free capacity is achieved at 44 dB, 49.5 dB, and 51.7 dB SNR using 4X1, 9X1 and 16X MISO system, respectively.

1. Introduction

The VLC MIMO system emerge as the promising technology used to support high performance in communication systems [1]. MISO-VLC system is generalized into two types, i.e., the imaging and nonimaging MISO system. The most usage in MISO equipment system is imaging in which the channel matrix is guaranteed to be with full-rank, and the multiplexing gain is extremely high [2]. There are lot of challenges in VLC system. The cell interference is one of the important issues need to be investigated and solved. The cell interference is initiated when the different neighbor cells attempt to use the identical resource at the same time. The cell interference deteriorates the system performance especially channel capacity, bit error rate, and data rate. The MISO system can increase the channel capacity without consuming extra bandwidth and SNR. The high-order MISO is commonly applied in VLC system and for further exploiting of the multipath channel capacity [3–5]. However, increasing the number of light-emitting diode (LED) and other hardware of the transmitter in a limited space is also a challenge. Therefore, it is important to find an optimized topology for the high-order MISO array system in mobile receivers which can maximize the system performance of MISO-VLC.

Several interference mitigation methods have been studied in the literature under various conditions and network infrastructures. The distribution of multicolor, time division, frequency reuse, and cell coordination is commonly used to eliminate the interference. The utilization of bandwidth, power, and blanking resources are utilized to overcome the cell interference effects. In [6], the dynamic and static allocation of frequency resources, time slots, and the power distribution is controlled at the receiver to ensure that the cell

interference remains within acceptable limits. The signal-to-noise ratio (SNR), signal-to-interference-noise ratio (SINR), and optical channel constraints relation is investigated in [7] to provide fair comparison across optical wireless communication. A phase predistorted joint detection technique is investigated in [8] to improve the system performance of uplink nonorthogonal multiple access (NOMA). This scheme outperforms the previously proposed successive interference cancellation-based NOMA with or without predistortion. The fix power allocation to successive interference cancellation algorithms is examined. These schemes increase the complexity at transmitter side. The proposed scheme in [9] is comprised of a two-level algorithm—one at the base station level, and the other at a central controller to which a group of neighboring base stations are connected. The frequency share and reuse combined method is investigated in [10], in which the two resource allocation algorithms are used to minimize interference and maximize the system throughput. This technique utilizes more resources by increasing the number of cells. A static scheduler technique is offered to achieve high signal-to-interference-noise ratio (SINR) in [11]. Two approaches are proposed, one for the centralized part, and the other is based on the greedy color allocation. Both approaches improve the performance of cell-edge users but they increase the complexity of the system. A polynomial time distributed algorithm is proposed in [12] to minimize the cell interference, while the resource allocations has been tackled with blanking. However, the excessive use of blanking may deteriorate the performance. The pilot-based interference estimation scheme proposed in [13] is a crucial step to control power and band resources for cell–edges users. However, the pilot-based schemes are not accurate, and it utilizes extraband resources. An orthogonal frequency division multiplexing (OFDM), based load balancing algorithm is proposed in [14] for managing the resources of the resulting hybrid VLC/RF network and determining the user association to each system. The complexity of this optimization problem is excessively high for practical VLC/RF networks. The coverage analysis of multiuser VLC networks is presented in [15]. This work employed a dynamic cell formation method for grouping the optical access points in multiple optical cells that cover a footprint to minimize the intercell interference. Then, the transmission based on blind interference alignment in each optical cell is utilized to minimize the interference.

This paper investigates the channel capacity in cell interference area by using the MISO system. The interference power is different in different areas of the room due to interference and distance. The channel capacity is deteriorated due to signal-to-interference-noise ratio (SNIR). Therefore, the formulation to find the number of MISO array is utilized which minimize the intercell interference effect. The cell interference free channel capacity is derived by using a high-order MISO array at different levels of SNR. This technique secures the power, bandwidth, transmitter, and receiver complexity and many other complex algorithm used in transmitter and receivers. The high SNR produces high SNIR and decrease the channel capacity especially in the intercell interference regions. The deterioration of channel capacity is compensated by the high order of MISO array. The MISO system is optimized for high interference area of the room which is more depending upon the placement of LEDs and distance between them and transmitted power.

This paper is structured as follows. Section 2 describes the proposed schemes. The analyses are shown in Section 3. Section 4 represents the simulation results. Section 5 concludes this paper.

2. System Model

The higher-order MISO array is used to improve the capacity at high SNR of the system in cell interference environment. The LED array for brightness and data transmission are used for multiple receivers simultaneously. In this paper, four cells of N_T number of LEDs are installed at the same distances. We consider same number of LEDs in each cell.

The signal $x_i(t)$ is transmitted at time t from LEDs $i = 1, 2, 3, ..N_T$, and $y_j(t)$ is received at time t.

$$y_R(t) = \sum_{i=1}^{N_t} Rh_{ij}(t)x_i(t) + n_j(t), \tag{1}$$

where $h_i(t)$ is the complex channel gain with $E[h_i(t)]^2 = 1$ and R represents the responsiveness of the photo-detector (in A/W) and $x(t) = [x_1(t)x_2(t)x_3(t) \cdots ..x_{N_T}(t)]^{\mathrm{T}}$ and $y_R(t) = [y_1(t)y_2(t)y_3(t) \cdots ..y_{N_T}(t)]^{\mathrm{T}}$. The VLC channel matrix H_o with $1XN_T$ dimension as shown in Figure 1.

The direct signal or line of sight (LOS) is considered; however, signals from non-LOS (NLOS) are negligible. The distance between the transmitter and receiver is d, A_{PD} is the receiving area, p is the refractive index, ψ is the angle of incidence, φ is the irradiance angle, γ is the reflectance factor, l is the order of Lambertian emission, ψ_c is the field of view (FOV), and $T(\psi)_{\mathrm{cof}}$ is the signal transmission coefficient of an optical filter. The $g(\psi)$ is the gain of the optical concentrator which is expressed in [16]

$$g(\psi) = \begin{cases} \dfrac{p^2}{\sin^2\psi_c}, & 0 \le \psi \le \psi_c, \\ 0, & 0 \ge \psi_c, \end{cases} \tag{2}$$

where A_{eff} is effecting area of photodiode and A_r is the surface area of the photodiode, which can be write mathematically as

$$A_{\mathrm{eff}}(\psi) = \begin{cases} N_r A_r \cos\psi, & 0 \le \psi \le \dfrac{\pi}{2}, \\ 0, & \psi > \dfrac{\pi}{2}, \end{cases} \tag{3}$$

$$A_{\mathrm{eff}}(\psi) = \begin{cases} N_r A_r \cos\psi T_s(\psi) g(\psi), & 0 \le \psi \le \psi_c, \\ 0, & \psi > \psi_c. \end{cases}$$

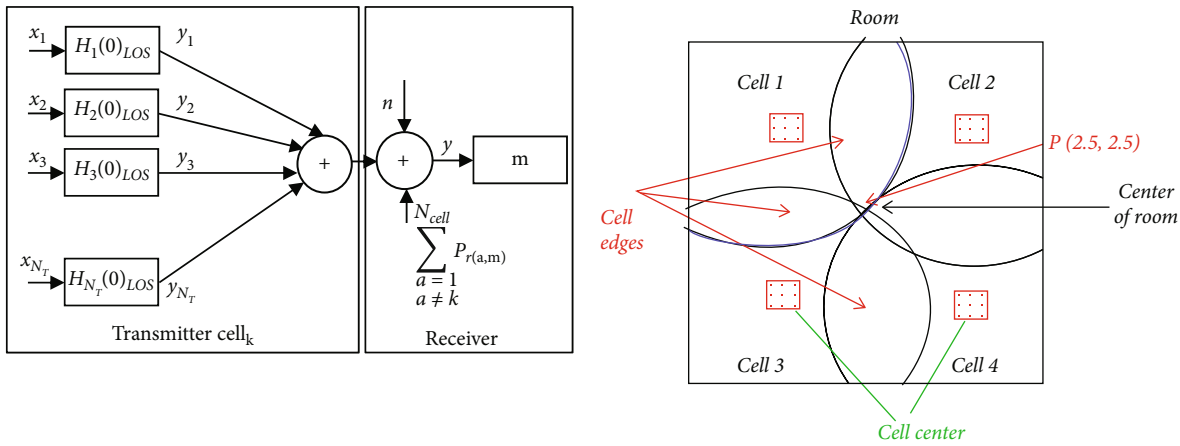

FIGURE 1: Top view of VLC MISO system. (a) MISO system. (b) Footprint of four cells.

The transmitted and received power can be expressed as

$$P_r = \sum_{i=1}^{N_T} P_{t(i)} H_d(t). \tag{4}$$

However, the transmitted power is divided equally between all number of LEDs and received power in the room is shown in Figure 2, where transmitted power is

$$P_t = \frac{I(\varnothing)}{R(\varnothing)}, \tag{5}$$

where $R(\varnothing)$ is radiant Lambertian.

Received power is a product of received intensity $I_t(\varnothing)$ and the effective area $A_{\text{eff}}(\psi)$. Therefore, the received power can be defined as [17]

$$P_r = \frac{I(\varnothing)}{d^2} A_{\text{eff}}(\psi), \tag{6}$$

$$H_d(0)_{\text{LOS}} = \begin{cases} \dfrac{(l+1) N_r A_r \gamma \cos^l(\varphi) g(\psi) T(\psi)_{cof} \cos(\psi)}{2\pi d^2}, \\ 0 \le \psi \le \psi_c, \\ 0, \text{elsewhere}. \end{cases} \tag{7}$$

Equation (7) represents the DC gain $H_d(0)$ in LOS in frequency domain. The average transmitted optical power is given in

$$P_t = \lim_{T \longrightarrow \infty} \frac{1}{2T} \int_{-T}^{T} x(t) dt. \tag{8}$$

The different MISO cells are transmitting different bit streams data. Therefore, the m is nearby receiver to the k^{th} cell as shown in Figure 1(a). Thus, the maximum SNR is received from the k^{th} cell. The powers from neighbor cells which are using the same signal shape but different bit streams are considered interference $\sum_{\substack{a=1 \\ a \neq k}}^{A} P_{r(a,m)}$ as given in

$$P_{r(m)} = P_{r(k,m)} + \sum_{\substack{a=1 \\ a \neq k}}^{N_{\text{cell}}} P_{r(a,m)} \tag{9}$$

The footprint of four cells are shown in Figure 1(b), and the illumination of every cells is overlapping the neighbor cell which cause the interference. However, the interference area and cell edges are clearly mentioned in Figure 1(b). The highest interference area is located at the center of the room.

3. Analysis

In this paper, the channel information of the VLC system is known at both the side receiver and transmitter. The [18, 19] multiple independent data streams are simultaneously transmitted from different cells to achieve higher transmission data rate. The diversity gain of MISO transmission technique is transmitting same bit streams within a cell. The diversity gain increases the SNR within the cell and improves the channel capacity of the system. In this paper, the diversity gain is analyzed within the cells of a VLC system. The cell interference of the neighbor is analyzed between cells which dominant at the boundaries of the cell as shown in Figure 1(b). The cell interference is compensated through number of LEDs N_T at transmitter. The interference signals are dominant in cell edges and center of the room; therefore, the channel capacity performance are affected in interference regions. The cell interference effect is mitigated by increasing the number of LEDs at the transmitter. The higher-order MISO transmitter can be utilized only in high interference areas if receivers are static.

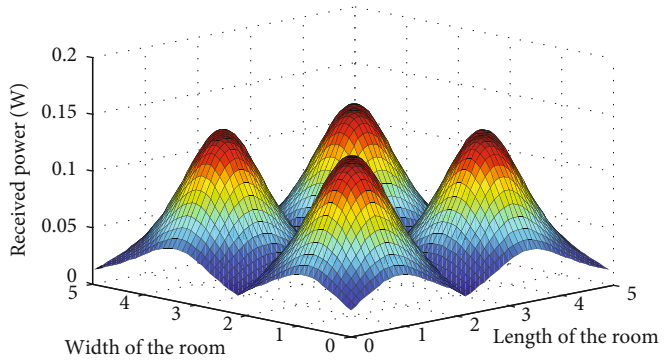

Figure 2: Received power of four cells' constrain.

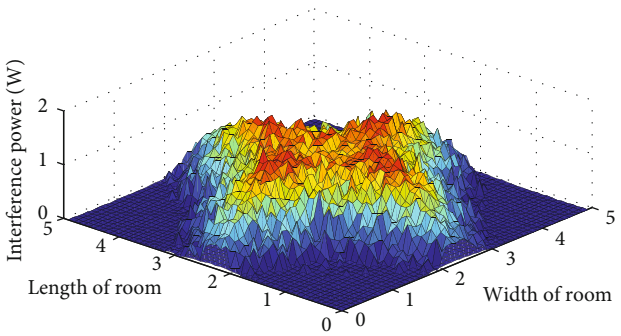

Figure 3: Interference power of four cells' indoor room.

The capacity of MISO AWGN channel:

$$C_{\mathrm{MISO}} \le \sum_{i=1}^{N_T} \log(1+\mathrm{SNR}), \qquad \gamma = \frac{P_{r(k)}^2}{n^2 W} N_T, \tag{10}$$

with cell interference $\mathrm{SNIR} = \mathrm{SNR}_{\mathrm{ICI}} \le (P_{r(k)}^2/(n + \sum_{\substack{a=1 \\ a\neq k}}^{N_{\mathrm{cell}}} P_{r(a,m)})W)N_T$, the $\sum_{\substack{a=1 \\ a\neq k}}^{N_{\mathrm{cell}}} P_{r(a,m)}$ is cell interference power from neighbor cells as shown in Figure 3.

The channel capacity per band for single input and single output (SISO) in interference environments is given below:

$$\frac{C}{W} \le \frac{1}{2} \log \left(1 + \frac{\left(P_{r(k)}\right)^2}{\left(n + \left(\sum_{\substack{a=1 \\ a\neq k}}^{N_{\mathrm{cell}}} P_{r(a,m)} \right)^2 \right) W} \right). \tag{11}$$

The approximation of noise at high interference is negligible. The MISO capacity is compared with capacity of SISO system without interference (SISOWI) as shown in Figure 4 to estimate the number of N_T

$$\frac{1}{2} \log \left(\frac{P_{r(k)}^2}{nW} \right) \ge \frac{1}{2} \log \left(\frac{P_{r(k)}^2}{\left(n + \sum_{\substack{a=1 \\ a\neq k}}^{N_{\mathrm{cell}}} P_{r(a,m)} \right) W} N_T \right),$$

$$\left(\frac{P_{r(k)}^2}{nW} \right) \ge \frac{P_{r(k)}^2}{\left(n + \sum_{\substack{a=1 \\ a\neq k}}^{N_{\mathrm{cell}}} P_{r(a,m)} \right) W} N_T,$$

$$\sum_{\substack{a=1 \\ a\neq k}}^{N_{\mathrm{cell}}} P_{r(a,m)} \ge \frac{P_{r(k)}^2}{P_{r(k)}^2} nN_T W - n,$$

$$\sum_{\substack{a=1 \\ a\neq k}}^{N_{\mathrm{cell}}} P_{r(a,m)} \ge nN_T W - n,$$

$$N_T \ge \left(\frac{\sum_{\substack{a=1 \\ a\neq k}}^{N_{\mathrm{cell}}} P_{r(a,m)} + n}{Wn} \right), \tag{12}$$

Equation (12) defines the required number of N_T to compensate the cell interference power in MISO systems. However, the SNR can be define as in

$$\left(\frac{P_{r(k,m)} + \sum_{a=1}^{N_{\mathrm{cell}}} P_{r(a,m)}}{n} \right) \ge N_T W - 1,$$

$$\left(\frac{P_{r(k,m)}}{n} \right) \ge \left[(N_T W - 1) - \frac{\sum_{a=1}^{N_{\mathrm{cell}}} P_{r(a,m)}}{n} \right]. \tag{13}$$

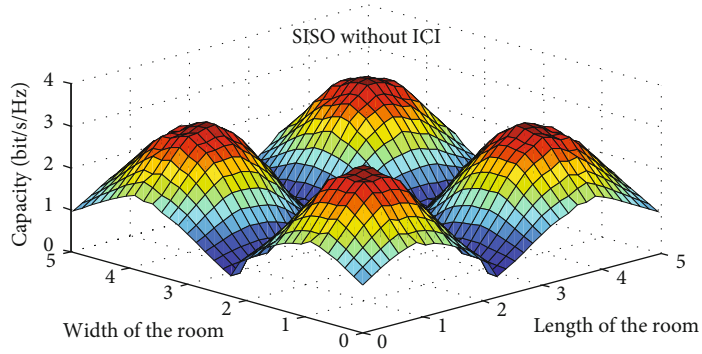

Figure 4: Channel capacity of SISO without considering interference.

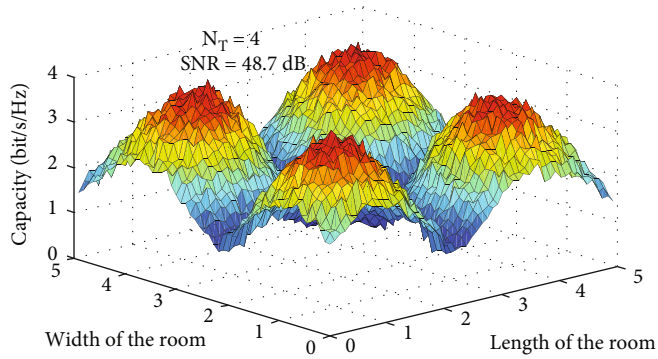

Figure 5: Channel capacity of four cells and each cell contain $N_T = 4$ MISO system.

The MISO system is optimized at highest interference area which is the center of the room. The center of the room is at $P(x - \text{axis} = 2.5, y - \text{axis} = 2.5)$ as shown in Figure 1(b), the light from all cell received equally. Therefore, the interference power is three time greater then principle cell as shown in

$$\left(\frac{P_{r(k,m)}}{n}\right)_{(2.5,2.5)} \geq \left[(N_T W - 1) - 3 * \frac{P_{r(k,m)}}{n}\right]. \quad (14)$$

The condition for optimization is the difference between $(N_T W - 1)$ and $(3 * (P_{r(k,m)}/n))$ should be high enough to achieve the high SNR. Therefore, analytically the high SNR requires high MISO array system in interference areas of the room. Hence, the MISO system is optimized as per high interference to achieve the required SNR.

The overall capacity of whole indoor cellular system is equal to the combination of all cell's capacity. However, every cell is transmitting different bit stream which creates the cell interference in neighboring cells. Every cell utilizes the MISO system with diversity gain and get an improved capacity in that particular cell. The overall capacity

$$C = \sum_{\text{cell}\,(i)=1}^{Y} C_{\text{cell}(i)}, \quad (15)$$

where Y represents the number of cells and every cell (i) utilizes diversity gain with N_T order of MISO system to minimize the cell interference from neighbor cell. The distance between cells decreases the SNIR at the boundaries of every cell. However, the less distance between cell increases the cell interference which requires the higher order of MISO system. Therefore, we have trade-off between cell interference, distance between LEDs within cell, SNR and order of MISO system within one cell. The cell interference varies due to two factors one is distance between cells and SNR. However, distance between LEDs and SNR increase the interference at boundaries of the cell. The distance between LEDs improves the illumination distribution in the room, and interference power is compensated via MISO system.

4. Simulation Result and Discussion

The simulation of this indoor VLC MISO system is performed by using four cells installed in a 270 sq. ft. room. MISO LEDs are placed at same distances inside every cell, and the room is covered by four cells. Every cell has fixed number of N_T or LEDs. The receiving surface is 2 meter away from ceiling. This paper examined the simulation and analytical channel capacity which is deteriorated due to cell interference. The VLC is a high SNR communication; however, the high SNR is a big challenge to be achieved in intercell interference environments, because the intercell interference increases in high SNR.

Figure 5 is simulated at $N_T = 4$ MISO system for every cell. Figures 5–7 show that the higher-order MISO systems increase the channel capacity specially at high SNR in cell

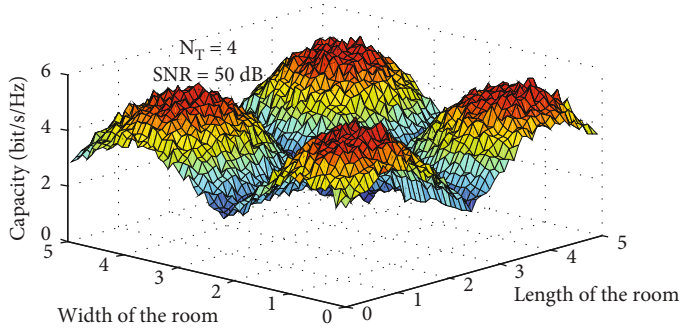

Figure 6: Channel capacity of four cells and each cell contain nine LEDs.

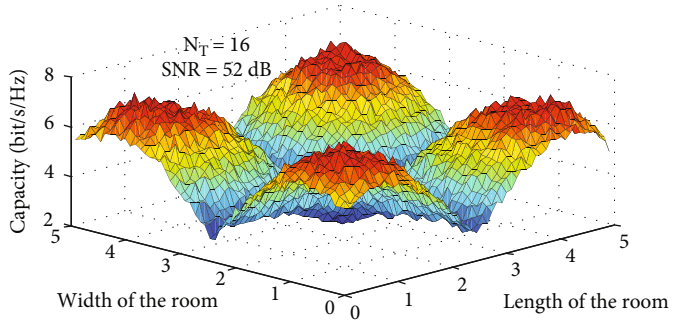

Figure 7: Channel capacity of four cells and each cell contain $N_T = 16$ MISO system.

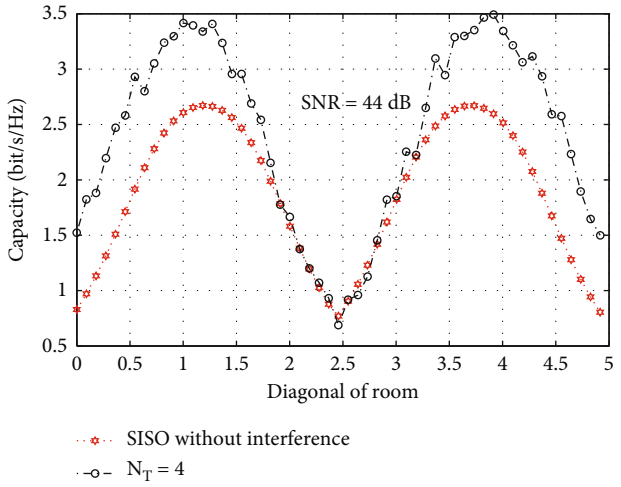

Figure 8: Channel capacity comparison of SISOWI and MISO $N_T = 4$ at 44 dB SNR.

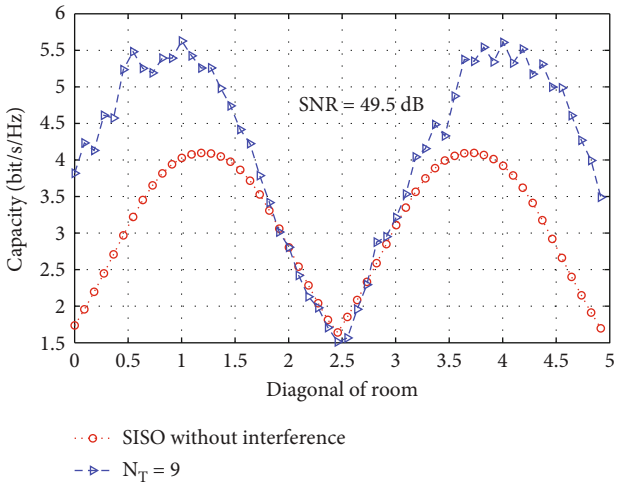

Figure 9: Channel capacity comparison of SISOWI and MISO $N_T = 4$ at 49.5 dB SNR.

interference regions. The center of the room is more affected with interference because the all four cells signals are combined at the center (signal overlapping). The minmum and maximum channel capacity is observed as 3.5 bit/s/Hz and 0.75 bit/s/Hz respectively which is much higher than channel capacity of SISO system as shown in Figure 5.

Similarly, Figures 6 and 7 is, respectively, simulated for $N_T = 9$ and $N_T = 16$ MISO system, and it is observed that the capacity is improved at high interference and low interference regions of the room. The SNR used in SISO are $N_T = 4$, $N_T = 9$, while $N_T = 16$ is used in the MISO system. The high capacity is noted as N_T increases. Hence, the higher N_T, MISO system reduces the effects of cell interference, particularly in high interference areas.

Moreover, this paper achieves the high SNR in cell interference environments. The MISO system is utilized to compensate the channel capacity in high-interference regions.

Figures 8–10 are simulated at the diagonal of the room by comparing the channel capacity of the MISO and SISOWI systems. Figures 8–10 depicted that the optimum capacity is achieved by using the MISO system. Higher-order MISO systems are simulated by including interference of neighbor cells. The MISO capacity is compared with SISOWI.

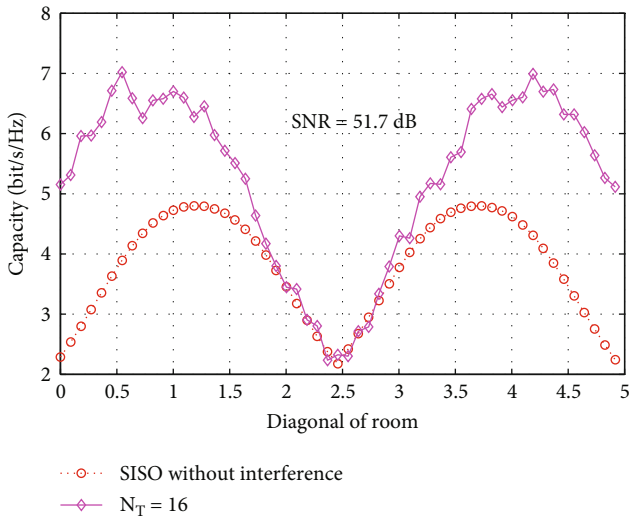

Figure 10: Channel capacity comparison of SISOWI and MISO $N_T = 16$ at 51.7 dB SNR.

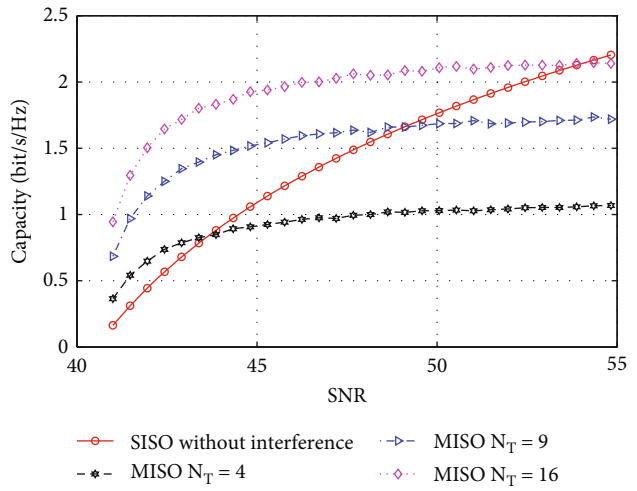

Figure 11: Channel capacity at high-interference area (1.5,1.5) location

Figure 8 shows that the in high-interference regions the SISOWI is achieved by $N_T = 4$ MISO system at 44 dB SNR. As the SNR increases the interference power increases, therefore, Figure 9 shows $N_T = 9$ MISO system is used at 49.5 dB SNR for high-interference area to achieve the SISOWI. Similarly, Figure 10 shows that the 51.7 dB SNR required $N_T = 16$ MISO system to achieve similar capacity response to that of SISOWI at the high-interference area.

Figure 11 shows the channel capacity at $(1.75, 1.75)$ location and the simulation at different SNRs using the SISOWI and MISO systems with interference. The results show that the highest channel capacity is achieved at $N_T = 16$ MISO system. The cell interference power increases with increasing of SNR, however, the SNR of $N_T = 4$, $N_T = 9$, and $N_T = 16$ MISO system become constant after getting certain level due to interference. The SISOWI increases with the increasing of SNR.

5. Conclusion

The proposed method in this paper attained the required capacity at high SNR by using the MISO system. The effect of intercell interference is high at high SNR especially at the overlapping regions. Therefore, a trade-off of the order of MISO array is investigated at different SNRs to achieve the interference free capacity system. The interference free capacity is achieved at 44 dB, 49.5 dB, and 51.7 dB SNR in cell interference environment at $N_T = 4$, $N_T = 9$, and $N_T = 16$, MISO system, respectively. Theoretical and simulation capacity show that the interference is eliminated and high SNR is achieved by using the high order of the MISO system. The mitigation of intercell interference at high SNR by using the MISO system outperforms the existing technique due to the less complexity of transmitter and receiver and cell planning.

Data Availability

The data used to support the findings of this study are available from the corresponding author upon request.

Conflicts of Interest

The authors declare no conflict of interest.

Acknowledgments

The work is self-funded by the authors who are working in Karary University and Syed University of Engineering and Technology,.

References

[1] C. Chen, W. D. Zhong, H. Yang, and P. du, "On the performance of MIMO-NOMA-based visible light communication systems," *IEEE Photonics Technology Letters*, vol. 30, no. 4, pp. 307–310, 2018.

[2] L. Wei, H. Zhang, and J. Song, "Experimental demonstration of a cubic-receiver-based MIMO visible light communication system," *IEEE Photonics Journal*, vol. 9, no. 1, pp. 1–7, 2016.

[3] T.-A. Tran and D. C. O'Brien, "Performance Metrics for Multi-Input Multi-Output (MIMO) Visible Light Communications," in *2012 International Workshop on Optical Wireless Communications (IWOW)*, Pisa, Italy, 2012.

[4] S. Deepthi and P. Visalakshi, "Enhanced optical OFDM: a novel approach for SISO and MIMO visible light communication system in indoor environment," *Optical and Quantum ElectronicsElectronics*, vol. 53, no. 9, pp. 1–24, 2021.

[5] K. Xu, H. Yu, and Y.-J. Zhu, "Channel-adapted spatial modulation for massive MIMO visible light communications," *IEEE Photonics Technology Letters*, vol. 28, no. 23, pp. 2693–2696, 2016.

[6] A. S. Hamza, S. S. Khalifa, H. S. Hamza, and K. Elsayed, "A survey on inter-cell interference coordination techniques in OFDMA-based cellular networks," *IEEE Communications Surveys & Tutorials*, vol. 15, no. 4, pp. 1642–1670, 2013.

[7] M. Rahaim and T. D. Little, "Interference in IM/DD optical wireless communication networks," *Journal of Optical Communications and Networking*, vol. 9, no. 9, pp. D51–D63, 2017.

[8] X. Guan, Q. Yang, and C.-K. Chan, "Joint detection of visible light communication signals under non-orthogonal multiple access," *IEEE Photonics Technology Letters*, vol. 29, no. 4, pp. 377–380, 2017.

[9] M. Rahman and H. Yanikomeroglu, "Enhancing cell-edge performance: a downlink dynamic interference avoidance scheme with inter-cell coordination," *IEEE Transactions on Wireless Communications*, vol. 9, no. 4, pp. 1414–1425, 2010.

[10] A. Ibrahim, T. Ismail, K. F. Elsayed, M. S. Darweesh, and J. Prat, "Resource allocation and interference management techniques for OFDM-based VLC atto-cells," *IEEE access*, vol. 8, pp. 127431–127439, 2020.

[11] K. Zhou, C. Gong, and Z. Xu, "Color planning and intercell interference coordination for multicolor visible light communication networks," *Journal of Lightwave Technology*, vol. 35, no. 22, pp. 4980–4993, 2017.

[12] A. Bin Sediq, R. Schoenen, H. Yanikomeroglu, and G. Senarath, "Optimized distributed inter-cell interference coordination (ICIC) scheme using projected subgradient and network flow optimization," *IEEE Transactions on Communications*, vol. 63, no. 1, pp. 107–124, 2015.

[13] V. P. Mhatre and C. P. Rosenberg, "Impact of network load on forward link inter-cell interference in cellular data networks," *IEEE transactions on wireless communications*, vol. 5, no. 12, pp. 3651–3661, 2006.

[14] A. Adnan-Qidan, M. Morales-Céspedes, and A. G. Armada, "Load balancing in hybrid VLC and RF networks based on blind interference alignment," *IEEE Access*, vol. 8, pp. 72512–72527, 2020.

[15] L. Yin and H. Haas, "A tractable approach to joint transmission in multiuser visible light communication networks," *IEEE Transactions on Mobile Computing*, vol. 18, no. 10, pp. 2231–2242, 2019.

[16] T. Komine and M. Nakagawa, "Fundamental analysis for visible-light communication system using LED lights," *IEEE transactions on Consumer Electronics*, vol. 50, no. 1, pp. 100–107, 2004.

[17] S. Fuada, A. P. Putra, and T. Adiono, *Analysis of received power characteristics of commercial photodiodes in indoor LoS channel visible light communication*, 2017, Unpublished.

[18] J. Lian and M. Brandt-Pearce, "Multiuser MIMO indoor visible light communication system using spatial multiplexing," *Journal of Lightwave Technology*, vol. 35, no. 23, pp. 5024–5033, 2017.

[19] C. Xu, S. Sugiura, S. X. Ng, P. Zhang, L. Wang, and L. Hanzo, "Two decades of MIMO design tradeoffs and reduced-complexity MIMO detection in near-capacity systems," *IEEE Access*, vol. 5, pp. 18564–18632, 2017.

Hindawi
Wireless Communications and Mobile Computing
Volume 2022, Article ID 9060676, 15 pages
https://doi.org/10.1155/2022/9060676

Research Article

Performance Analysis of Dual-Beam Free Space Optical Communication Link under Dust and Rain Conditions

Sultan Mahmood Yasir,[1] Naeem Abas,[1] Shoaib Rauf,[1] Muhammad Shoaib Saleem,[2] and Aun Haider[2]

[1]*Department of Electrical Engineering, University of Gujrat, Hafiz Hayat Campus, Gujrat, Pakistan*
[2]*Department of Electrical Engineering, University of Management and Technology Lahore, Sialkot Campus, Sialkot, Pakistan*

Correspondence should be addressed to Naeem Abas; naeemkalair@uog.edu.pk

Received 5 December 2021; Revised 29 June 2022; Accepted 12 July 2022; Published 8 August 2022

Academic Editor: Ghanshyam Singh

Free space optical (FSO) communication has become an enduring and well-established communication technology in the last few decades with several advantages of high data rate, enormous bandwidth, low power consumption, transportable technology without right of way, and inherently secure line of a sight communication system. The invisible, intensity-modulated signal of light propagated through the air and detected on the receiver side experiences attenuation because of uneven distribution of rain droplets, suspended dust aerosol particles, and the droplet size distribution of fog particles in atmospheric layer degrade performance of FSO communication link. The ever-increasing demand for high data rate has quest for an innovative research for a communication link. In this paper, the performance of a dual-beam FSO communication link is evaluated under rain and dust as attenuation conditions. The system parameters, such as link distance transmitted and received power, link distance, diameter of transmitter and receiver aperture, and divergence angle, are optimized for a metropolitan FSO communication link. Dual-beam FSO communication signal propagated through an estimated attenuation level at 30 dBm transmitted power for link distance up to 2.5 km. The optical power splitter and power combiners are used in the simulation to estimate different channel parameters without the MIMO technique. The information signal of the 10 Gbps data rate is internally modulated using the NRZ generator, externally modulated by the Mach-Zehnder, and an optical signal transmitted through a dual-beam optical spectrum frequency of 193.1 THz using power splitter technique apart from each other. A comprehensive analysis is performed to design and assess robust optical communication systems through efficiency parameters such as received power, optical signal-to-noise ratio (OSNR), bit error rate (BER), and Q-factors. Results show that received optical power is a weather-dependent variable that shows a decreasing pattern as weather attenuation increases. Likewise, Q-factor and OSNR show similar decreasing trend with introduction of rain and dust as attenuator; however, BER increases in presence of attenuation.

1. Introduction

FSO communication is mature communication technology used for wireless communication links for backhaul communication networks at high data rates without any electromagnetic interference, with advantages of reliability and range/link distance. The ever-increasing demand for data rate has forced researchers to find the ultimate solution for the existing and upcoming applications in the cellular network of the 5th generation because of bandwidth congestion of radio frequency. FSO communication has advantages of bandwidth, compared to optic fiber cable with several advantages of easy and portable installations, so it is better to replace high-cost optical fiber cable with an FSO link [1]. Optical wireless communication is a visible light communication system in which optical signals are traveled through the environmental layer, causing the loss of propagated signal along with the propagation channel and reducing the intensity of the transmitted signal at the optical receiver side [2]. There are several weather conditions like rain, dust, aerosol particles, and fog that degraded the performance of the FSO system [3]. Scintillation is another effect of an atmospheric layer

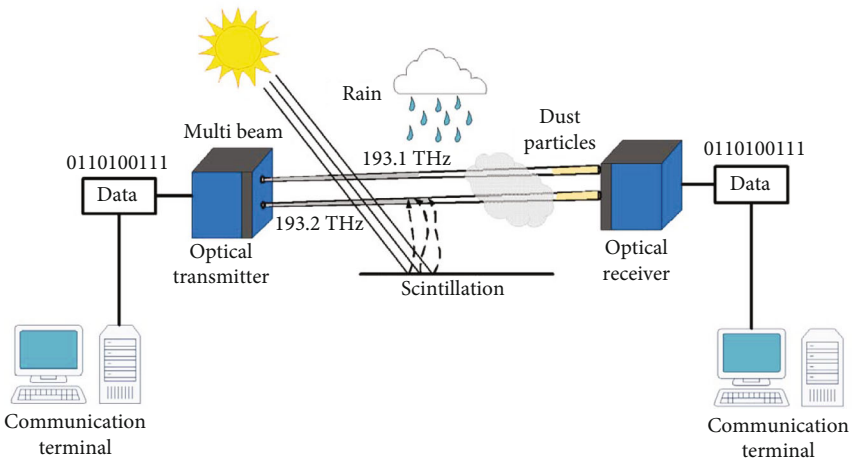

Figure 1: Multibeam FSO communication channel under rain and dust attenuation.

that may vary the intensity of the modulated optical signal traveled through the atmospheric channel and various automatic tracking techniques have been developed to deal with such problems [4]. To mitigate the scintillation effect, MIMO techniques can be used in which multiple laser beams are traveled through an atmospheric channel and are detected on multiple receiver apertures [5]. FSO communication is a mature technology utilized nowadays in numerous applications, such as backhaul communication networks, fiber backup networks, metropolitan area networks, and end-user networks to solve bottleneck issues of indoor and outdoor communication [6]. Several studies have been reviewed on atmospheric turbulence. It is observed that the channel attenuation is wavelength-dependent and optical signals behave differently [7–10]. A new optical Hermite-Gaussian mode multiplexing technique is also investigated for radio over free space optical communication (Ro-FSO) for connectivity between different picocells using a spatial correlator over a link distance of 500 meters. [11].

Lahore, a much populated metropolitan city, is an industrial hub and capital of province Punjab, Pakistan, and is ranked 42nd populated in the world [12]. Fog attenuation is one of the main performance degrading environmental factors that affects the performance of FSO communication link in December and January in Punjab, Pakistan. Optical attenuation due to fog can be a question mark but it can be mitigated by suitable link budget design, link margin, and link distance [13]. In the FSO communication system, the beam traveled through the environmental channel suffers from severe weather. A study has been carried out to investigate the effect of solar irradiance on FSO communication link based on Binary Phase shift Keying(BPSK), On-Off Keying (OOK), and differential phase shift keying (DPSK) [14]. An investigation for 10Gbps FSO communication has already been performed under the rain and dust attenuation conditions. Dust attenuation is estimated using the V-TSD model for suspended air particles and the visibility of the channel. Attenuation due to dust and rain is predicted in the paper [15]. The V-TSD model defines the experimental correlation with channel visibility and particles suspended in the airfield [16]. In the FSO communication system, another performance evaluating parameter for system design is the wavelength that can affect the link performance and receiver sensitivity of detection [17]. Raindrops are water droplets of a radius of 200 to 200 μm. These are significantly larger than a wavelength of an optical light source. These remained in the atmospheric layer for a short interval of time, so due to these factors, the rain has less effect on the performance of wireless optical communication as compared to other environmental factors [18]. The link distance is another geometrical design parameter of the FSO communication system. It has a significant effect on the performance of the FSO communication system [19]. There are several proposed techniques that are examined to mitigate the effect of the number of copropagating models grouped at the receiver side including the single mood filtration techniques and offset launch technique [20, 21]. The performance of the communication system is correlated with severe weather conditions. A comprehensive investigation under various weather conditions must be carried out before the physical installation of the communication system [22]. Geometrical losses are the constant losses related to the design of FSO communication links. Geometrical design parameters are fixed parameters of a communication system that have significant importance. FoV (Field of View) on the receiver side must be according to the footprint because the greater FoV will also produce noise in the original information signal [23]. The investigation report shows that, in geometrical design elements, divergence angle size is an important factor for long-distance FSO communication links. The result shows that, as the divergence of beam increases, BER is also increased. The author has suggested a beam divergence angle of 0.25 mrad for a link distance up to 70 km [24]. To improve performance of FSO communication system, different techniques are investigated, and it is common practice to use OFDM that is widely used in adverse weather. The performance can be improved with the help of semiconductor optical amplifier (SOA) for long-distance communication links [25]. A multibeam FSO communication link with the MIMO technique is used to mitigate the rain attenuation using two different carrier frequencies of 193.1 THz and 193.2 THz [26]. To mitigate the effect of specific fog attenuation, four beams are used with the MIMO technique to

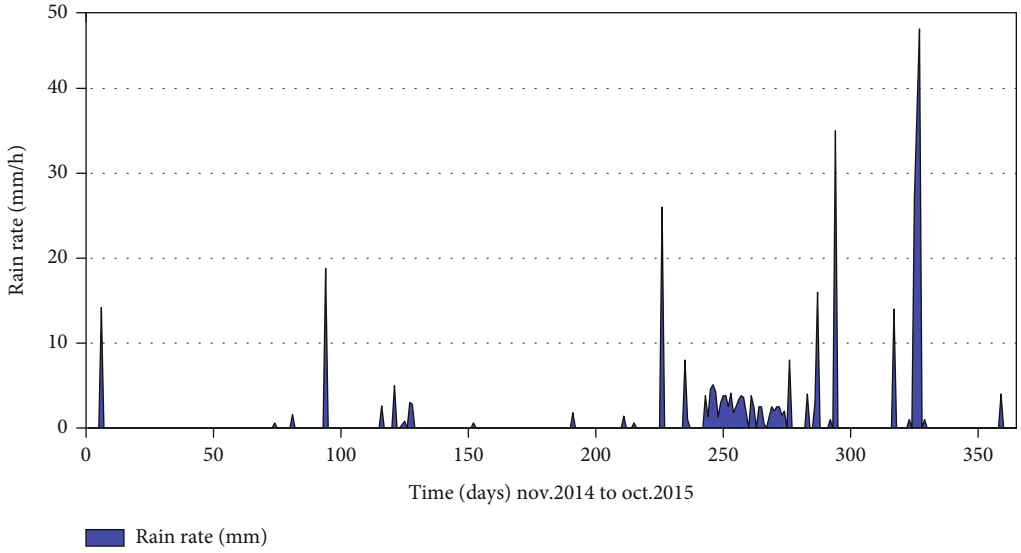

Figure 2: Rain rate (mm/hr) graph for Nov. 2014 to Nov. 2015 [15].

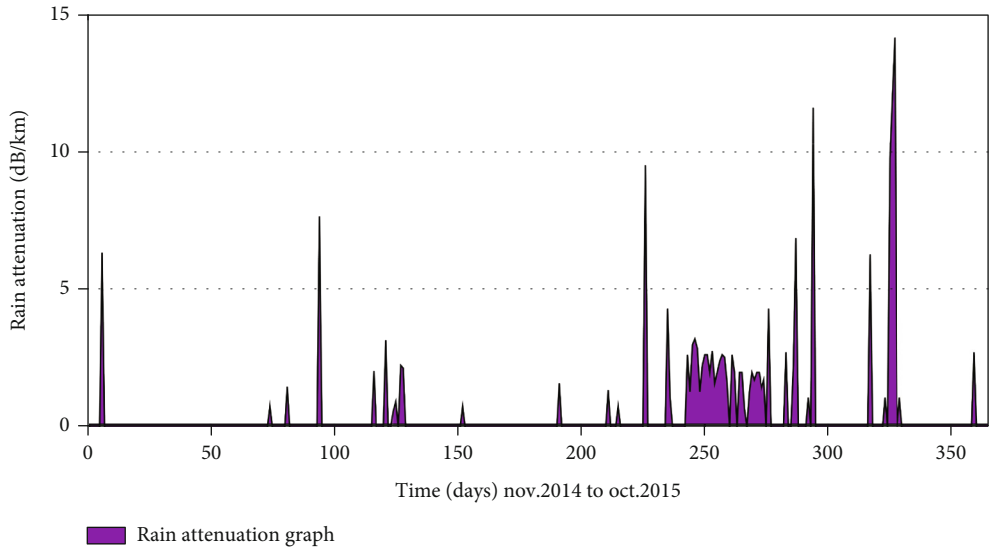

Figure 3: Rain attenuation graph [13].

Table 1: Estimated data statistics for rain attenuation from the graph.

Sr. No	Rain rate (mm/h)	Attenuation (dB/km)
Maximum value	47	14.19
Minimum value	1	0
Mean value	25.5	0.5031
Std. Deviation	14.58	1.655

investigate an FSO link for link distances of 1.7 km, 1.55 km, 1.5 km, and 1.4 km. The result shows that the quality of the signal enhances with multiple beams in communication [27].

In this paper, FSO communication link performance is examined under the rain and dust conditions in Lahore airfield. An information signal of 10 Gbps is transmitted using optical transmitter through dual-beam propagation using power splitter-combiner and analyses performed to improve FSO communication. The performance evaluating factors like OSNR, BER, and Q-factors are studied and simulated to find an FSO communication link under the rain and aerosol concentrations in the airfield of Lahore, Pakistan, to develop a fast metropolitan communication link in between different institutions especially universities and colleges.

2. Channel Model

FSO communication is an optical wireless communication link that can be used for indoor and outdoor data transmission. An optical signal is transmitted through an environmental layer or atmospheric channel. In indoor communication, channel noise is induced due to artificial lighting sources of similar wavelengths and in outdoor

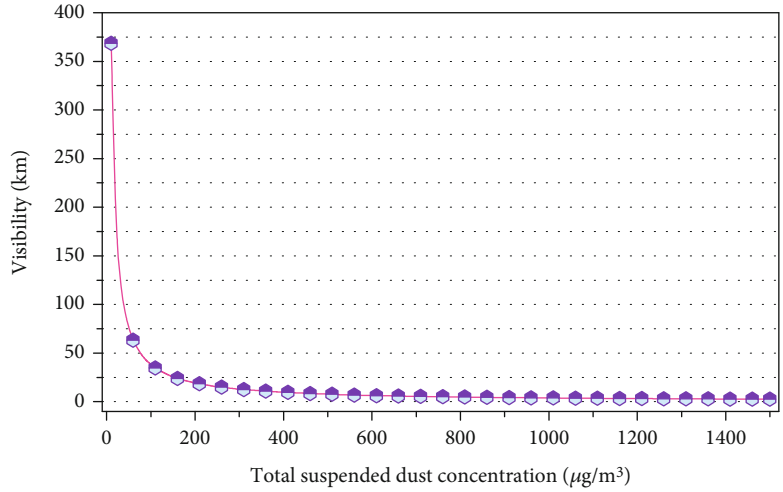

Figure 4: Illustration of visibility and concentration V-TSD model for Lahore, Pakistan.

Table 2: Data statistics of concentrations, visibility, and estimated attenuation in Lahore, Pakistan.

Location	C (μg/m^3)	Visibility (km)	Attenuation (dB/km) [29]
Walton	860	4.5961	10.48
Shadman	1350	2.9487	16.71
Township	745	5.2936	9.04
Misrishah	1192	3.3330	14.69
Charing Cross	1192	3.3330	14.69
City railway station	1523	2.6187	18.99
Bhatti Chowk	854	4.6279	10.41
Mazang Chungi	670	5.8764	8.10
Bund Road	1104	3.5944	6.7482
Choburgi Chowk	1210	3.2842	14.94
Niazi Chowk	1308	3.0419	16.17

Table 3: RF-spectrum data statistics of dual-beam FSO channel for link distance of 2.5 km at 193.1THz.

Attenuation (dB/km)	Signal power (dBm)	Noise power (dBm)	Maximum RF_C (Hz)
Clear sky (0.1 dB/km)	15.58	-52	$3.199x10^{11}$
Moderate attenuation (9.5 dB/km)	-31.42	-60	$3.199x10^{11}$
High attenuation (18.99 dB/km)	-78.8	-60.18	$3.199x10^{11}$

communication, natural light is a source of the noise. Optical transmitters transmit information in the form of light through the medium, experiencing atmospheric turbulence. The response of atmospheric attenuation was investigated using simulations or measuring the response of the channel on the receiver side. Scintillation is due to variation of temperature causing scattering of light signal to produce a pointing error on the receiver side whereas scattering and turbulence are two independent environmental factors and investigated using total impulse response (TIR). Figure 1 shows a block diagram of the multibeam FSO communication channel.

The droplet size distribution of rain and size of dust particles are random variables and scatter the light signal. The rain rate and dust concentration may be varied in the different areas, so the dual-beam propagation system may have variations in performance that effectively reduces the BER and improve the quality and reliability of the communication system.

2.1. Rain Attenuation. Rain and haze are environmental factors that cause optical attenuation for the FSO communication signal. Rain contains water droplets with a diameter larger than 0.5 mm. These water droplets scatter the optical signals causing pointing error at the receiver side [28]. The rain attenuation model for optical communication is expressed as: [15].

$$\alpha_{\text{rain}} = 1.076R^{0.67}\,\text{dB/km}, \tag{1}$$

where "R" represents a rain rate. The severity of rain attenuation depends upon the rain rate (mm/hour). The droplet size of rain is significantly larger than the wavelength of the laser used in FSO communication and has less attenuation as compared to fog attenuation. In this paper, we are investigating the effect of rain and dust on the FSO communication system for Lahore, Pakistan, and for this purpose, rain data is collected from the regional metrological department to simulate a rain attenuation model. The maximum rain rate recorded in Lahore on 23 Nov. 2015 was 47 mm/hr as shown in Figure 2 [15]. The estimated attenuation for the heaviest value of rain attenuation is 14.19 dB/km, as shown in Figure 3. Estimated data statistics for rain attenuation are presented in Table 1.

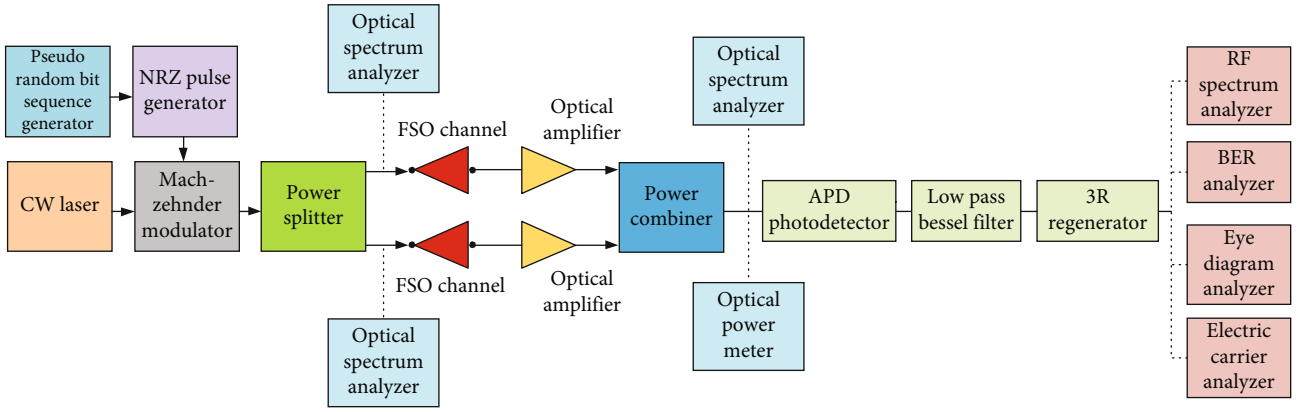

Figure 5: Simulation of dual-beam FSO communication link.

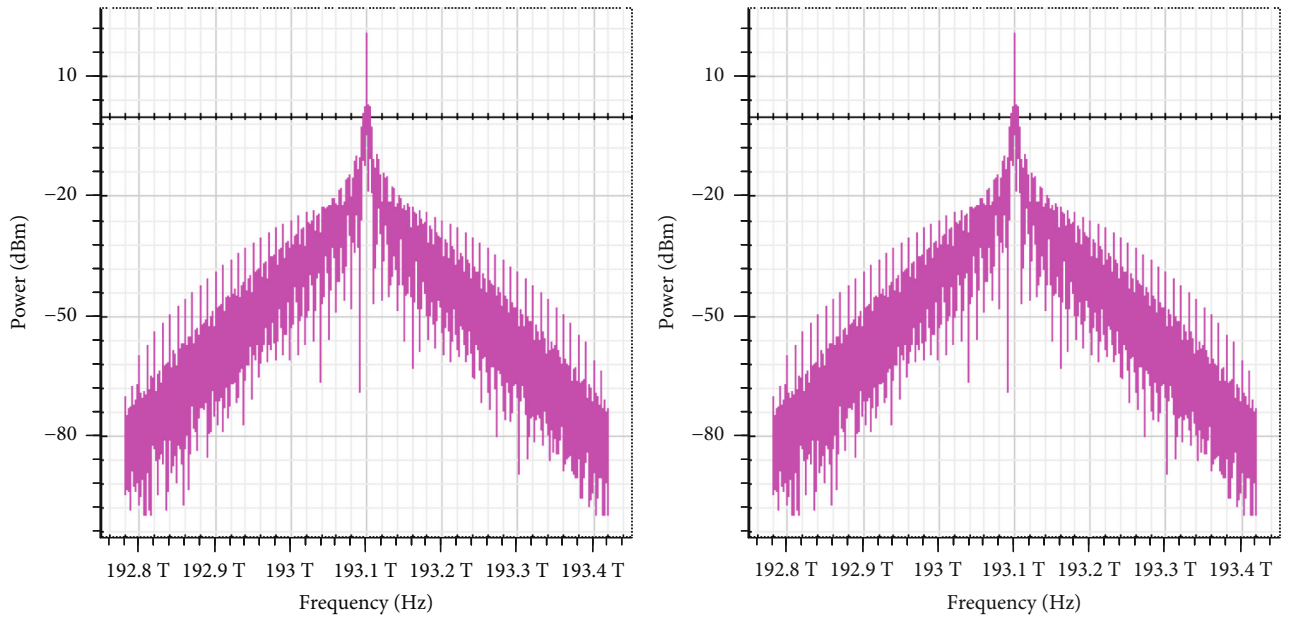

Figure 6: Optical spectrums of split dual-beam FSO Communication System on transmitter side.

2.2. Dust Attenuation. A joint investigation was made by the Pakistani, British, and Portuguese scientists to find out the concentration of different elements exhausted in the air by various industries in Lahore and they found the following concentration of these elements (Zn, Pb, C, and Ni) in different areas of Lahore with the help of Atomic Absorption Spectroscopy method [9]. The visibility of the atmospheric channel due to these concentrations was estimated using the visibility total suspended dust model (V-TSD Model). The mathematical equation for the V-TSD model is given below [15]:

$$C_{VTSD} = \frac{4050}{V^{1.016}} \tag{2}$$

where V is the visibility of the environment and C_{VTSD} is the total suspended dust concentration in $\mu g/m^3$. The graphical representation of the V-TSD concentration model is shown in Figure 4 [13]:

$1523\,\mu g/m^3$ is the highest concentration of suspended aerosol particles found in the area of the city railway station. The estimated optical attenuation due to total suspended dust particles is given in Table 2. The dust model used to estimate dust concentration is as under [29]:

$$\alpha = 52 \times V^{-1.05}\,\mathrm{dB/km}, \tag{3}$$

where V is the visibility in km and α is attenuation. This attenuation model is valid for the wavelength of 1550 nm and it is mostly used to estimate dust attenuation for FSO communication systems.

The invisible beams of FSO communication transmitted in the environmental channel suffer from scattering and absorption phenomena because of element concentration

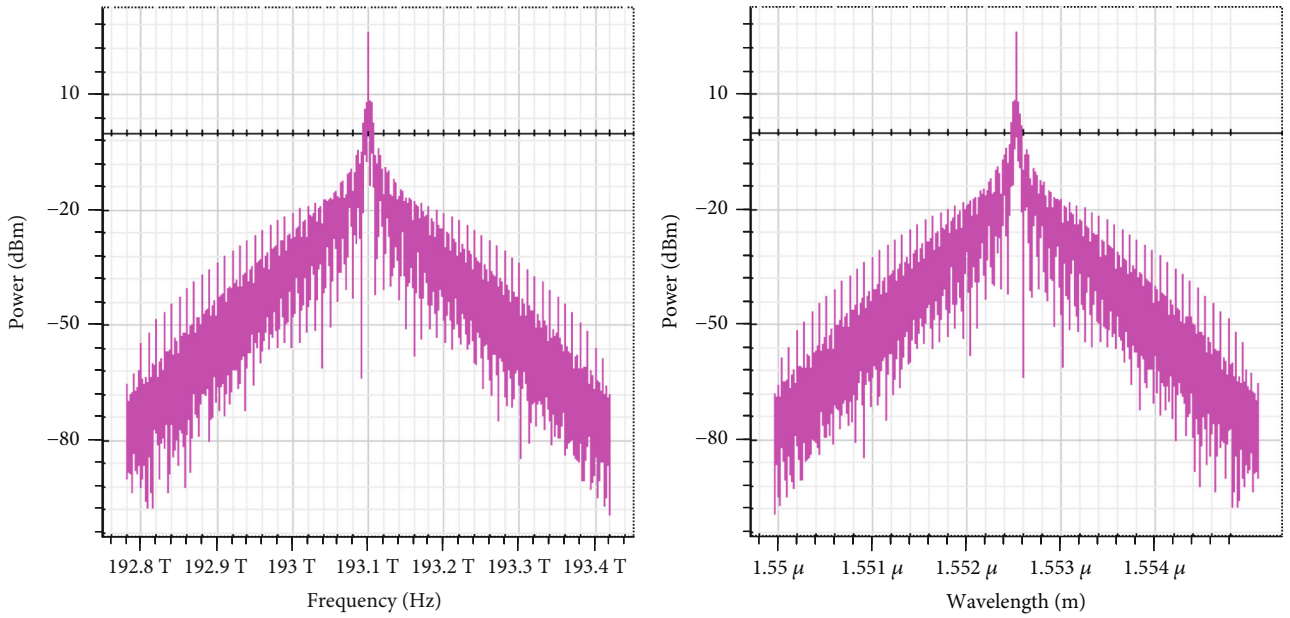

Figure 7: Optical spectrum of combined dual-beam FSO communication system on receiver side.

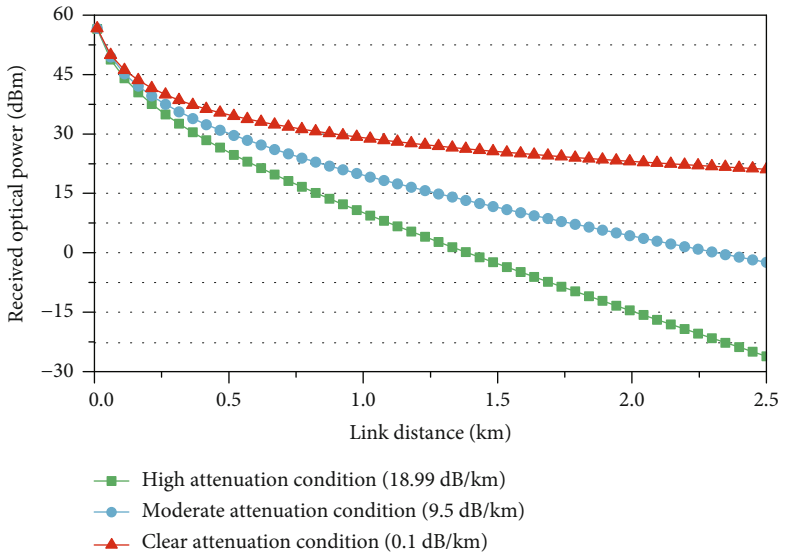

Figure 8: Illustration of received optical power and link distance correlation.

and total suspended dust, smog, fog, smoke, mist, haze, and rain droplets in the airfield. In the FSO communication system, a correlation between transmitted and received power for a link distance of L is described by Beer LambertâĂŹs [27]:

$$\tau(\lambda, L) = \frac{P_R}{P_T} \exp\left(\gamma(\lambda, L)\right), \tag{4}$$

where $\tau(\lambda, L)$ is transmittance of optical beam, $\gamma(\lambda)$ attenuation coefficient m^{-1}, P_R is received power of the optical signal, and P_T is the optical power of transmitter. The attenuation coefficient $(\gamma(\lambda)$ is the sum of absorption and scattering can be estimated as [30]:

$$\gamma(\lambda) = \gamma_m(L) + \gamma_a(L) + \beta_m(L) + \beta_a(L), \tag{5}$$

where $\gamma_m(L)$ and $\beta_m(L)$ are molecular absorption and scattering coefficients and $\gamma_a(L)$ and $\beta_a(L)$ are aerosol absorption and scattering coefficients, respectively. The link budget equation can be written as [31]:

$$P_R = P_T \times \frac{D_R^2}{\left(D_T + (\theta \times L)^2\right)} \times 10^{-\alpha L/10}, \tag{6}$$

where $D_R(\mathrm{m})$ is receiver aperture, $D_T(\mathrm{m})$ is diameter of transmitter aperture, $\alpha(\mathrm{dB/km})$ is attenuation, and $\theta(\mathrm{mrad})$ is

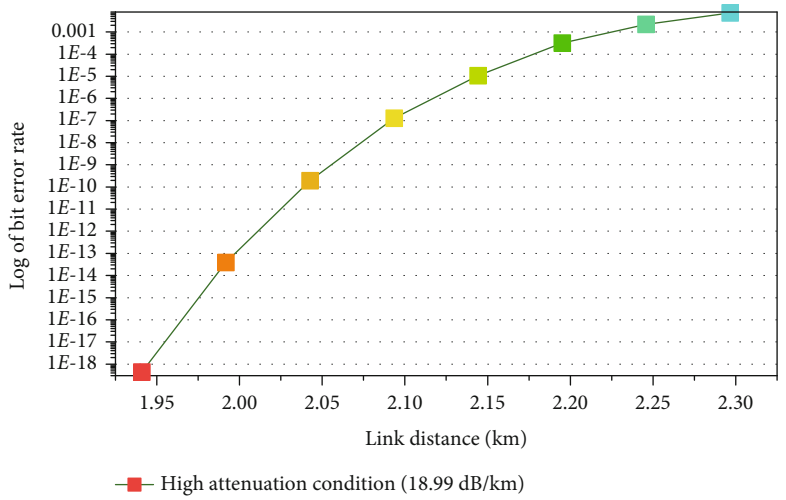

Figure 9: Illustration of BER and link distance correlation.

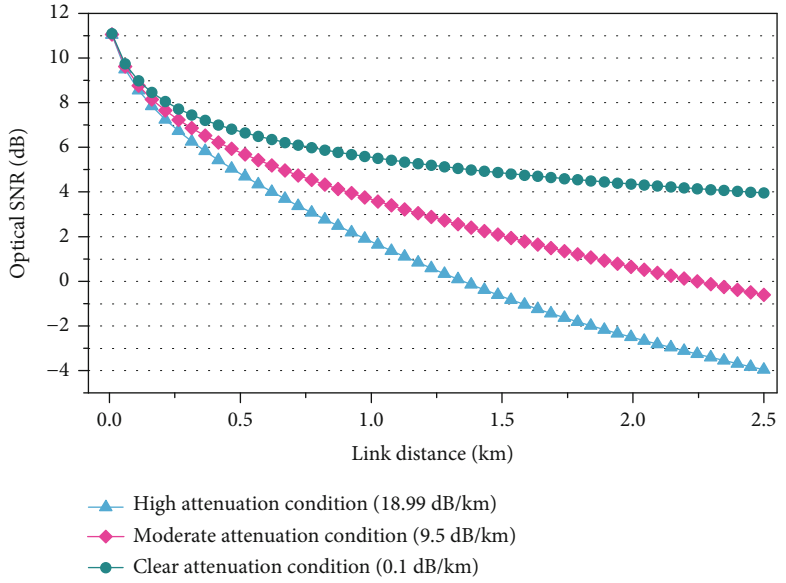

Figure 10: Illustration of OSNR and link distance correlation in clear, moderate, and high attenuation conditions.

divergence angle. The maximum attenuation due to rain and total suspended dust particles are 14.19 dB/km and 18.99 dB/km given in Tables 2 and 3. In this paper, analyses are performed under the following attenuation considerations, under clear sky condition, moderate, and higher attenuation at 0.1 dB/km, 9.5 dB/km, and 18.99 dB/km.

3. Design and Simulation of Dual-Beam FSO Link

In FSO communication, it is valuable to know what happened with a signal when transmitted through the environmental layer under various degrading factors, especially under rain and dust conditions. Under clear sky conditions, optical signal realistically receives optical attenuation as function path loss realistically; there is always a loss of signal power in the environmental channel. Optisys software was used to simulate the dual-beam FSO communication system consisting of a transmitter, an environmental channel for dual-beam signal propagation, and receivers to analyze channel impulse response under various estimated values of rain rate and dust attenuation. A dual-beam FSO system outlined and simulated as shown in Figure 4 for study and analysis under the expected impact of attenuation on three R's (range, rate, and reliability) of the FSO link in Lahore, Pakistan. In this article, a dual-beam FSO communication system simulated for a 10 Gbps data rate using two separate beams for link distance up to 2.5 km. A pseudorandom bit sequence (PRBS) generator is used to generate sequences of bits in the optical transmitter. A nonreturn zero (NRZ)

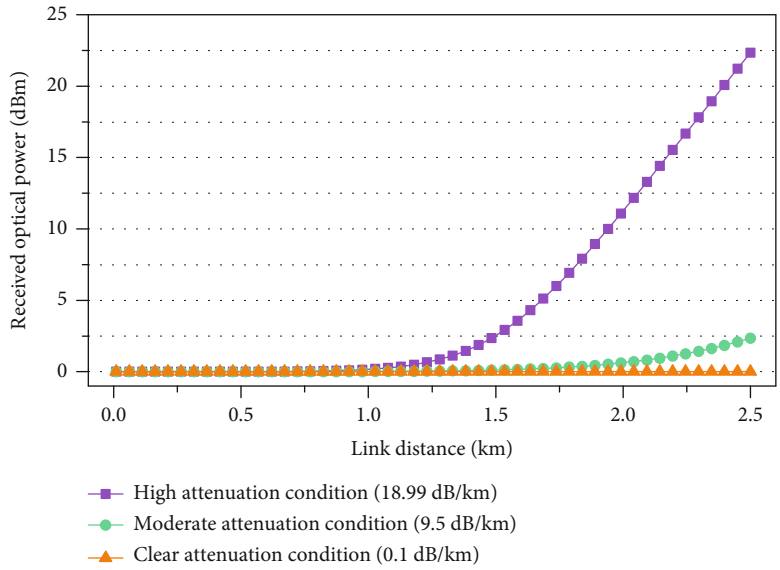

Figure 11: Illustration of noise power distribution throughout FSO channel.

generator is used to generate current pulses according to generate a sequence of 0's (off bits) and 1's (on bits) to modulate binary information in the form of current. CW laser is used for an optical source with a frequency of 193.1 THz at 30 dBm transmitter power. The scattering effect will fade the signal on the receiver side, so while designing an optical transmitter, it is also important to select a suitable size of divergence angle, a diameter of the transmitter, and receiver apertures so that geometrical losses can be reduced [23]. The geometrical design parameters of FSO channels are 1.5 mrad divergence angle and 5 cm and 20 cm diameters of transmitter and receiver apertures. NRZ pulses from the pulse generator and optical beam of CW laser are modulated by the Mach-Zehnder. The intensity-modulated signal is split by a power splitter into two FSO channels that have an optical amplifier of 20 dB gain and a figure noise of 4 dB. The optical transmitter uses the wavelength of 1552.5 nm for both optical beams for transmission of the optical signals. The FSO channel beams are combined with the power combiner at the receiver side with internal interferences. An avalanche photodetector (APD) receives an optical signal and is transduced into an electrical signal. On the receiver side, APD has response of 1 A/W with a gain of 3 dB followed by a low pass Bessel filter (LPBF) with a cut-off frequency of 0.8-bit rate that is utilized to annulled high-frequency contents of the electrical signal The geometrical design parameters of FSO channels are 1.5 mrad divergence angle and 5 cm and 20 cm diameters of transmitter and receiver apertures. NRZ pulses from the pulse generator and optical beam of CW laser are modulated by the Mach-Zehnder. The intensity-modulated signal is split by a power splitter into two FSO channels that have an optical amplifier of 20 dB gain and a figure noise of 4 dB. The optical transmitter uses the wavelength of 1552.5 nm for both optical beams for transmission of the optical signals. The FSO channel beams are combined with the power combiner at the receiver side with internal interferences. An avalanche photo detector (APD) receives an optical signal and is transduced into an electrical signal. On the receiver side, APD has response of 1 A/W with a gain of 3 dB followed by a low pass Bessel filter (LPBF) with a cut-off frequency of 0.8-bit rate that utilized to annulled high-frequency contents of the electrical signal [32]. The 3R generator is used to reproduce the original bit sequence and to generate an electrical signal from the received signal. The quality of the received signal is analyzed using BER and an Eye diagram analyzer. The optical receiver reproduces the original data signal encoded in the optical carrier. The RF-spectrum analyzer was used to find the frequency response of CW laser and signal power in the frequency domain.

An optical spectrum analyzer is used to measure the optical frequency, wavelength, and signal strength on the transmitter and receiver sides. The received power is analyzed to observe the values of signal and noise power. To enhance the quality and reliability of the FSO communication system, an optical signal beam is split into a dual-beam with a power splitter and combined at the receiver side with a power combiner. The simulation block diagram of the system is shown in Figure 5.

4. Results and Discussion

A dual-beam FSO communication system performance is studied and analyzed under the rain and suspended dust concentrations in the airfield of Lahore, Pakistan. The performance of the optical communication system is simulated and evaluated under various attenuation (clear 0.1 dB/km, moderate 9.5 dB/km, and high attenuation 18.99 dB/km) conditions. Figure 6 shows the optical spectrums of both transmission channels with the same maximum and minimum amplitudes of 27.23 dBm and -106.059 dBm.

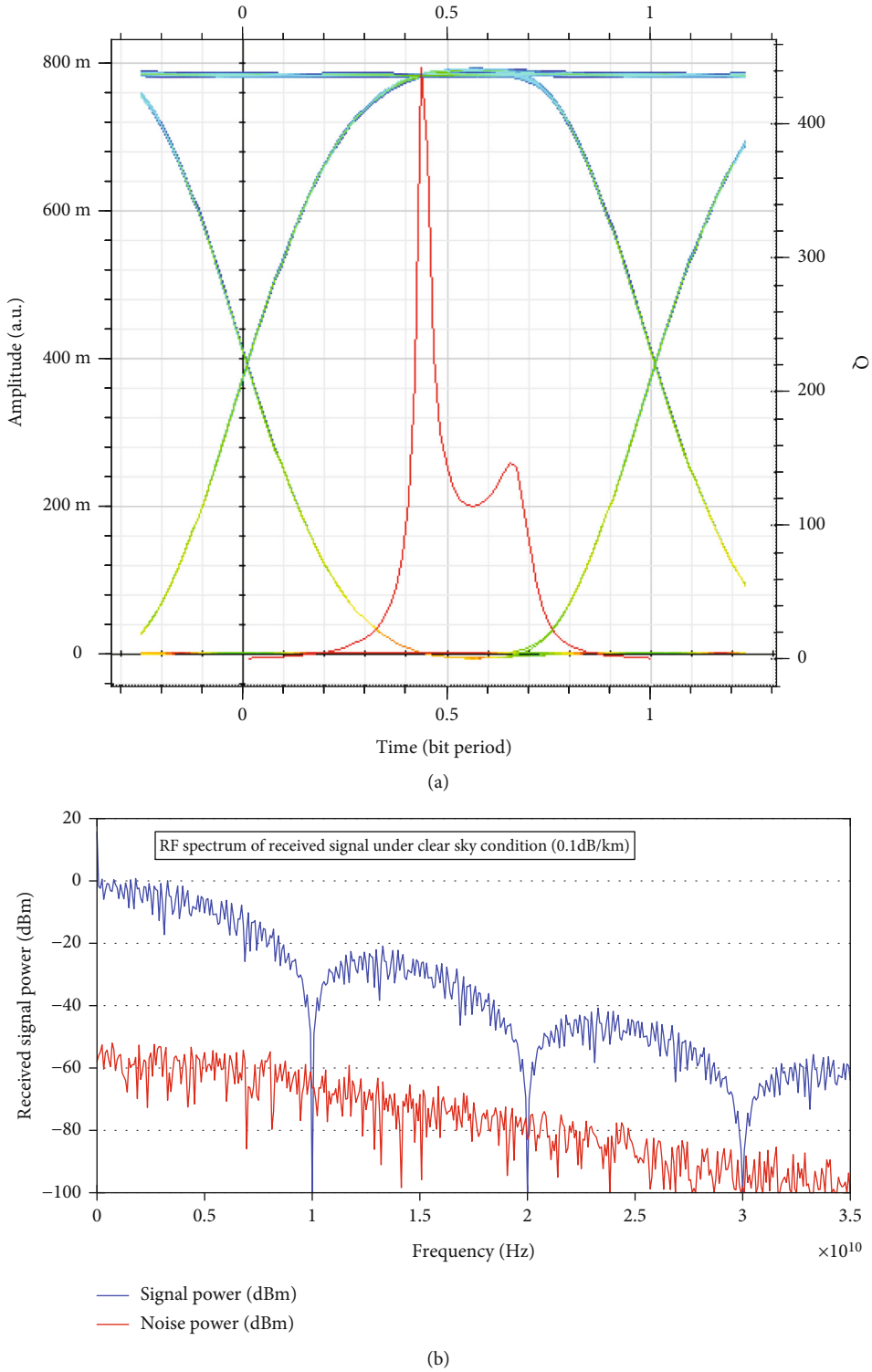

FIGURE 12: (a) Eye diagram under clear sky condition. (b) Signal power and noise power spectrum under clear sky condition.

CW laser Beam propagated through atmospheric attenuation of 18.99 dB/km for a link distance of 2.5 km and combined using a power combiner. The optical spectrum of both independent FSO channels illustrated in Figure 7 has maximum and minimum signal power amplitudes of -27.15 dBm and -103.5 dBm. The centralized frequency of 193.1 THz remains the same as the received power signal varies due to atmospheric attenuation.

It is observed that path loss increases with the increase in link distance between optical transmitters and receivers. This path loss due to optical attenuation limits the received optical power at the receiver side. There is a sturdy relationship

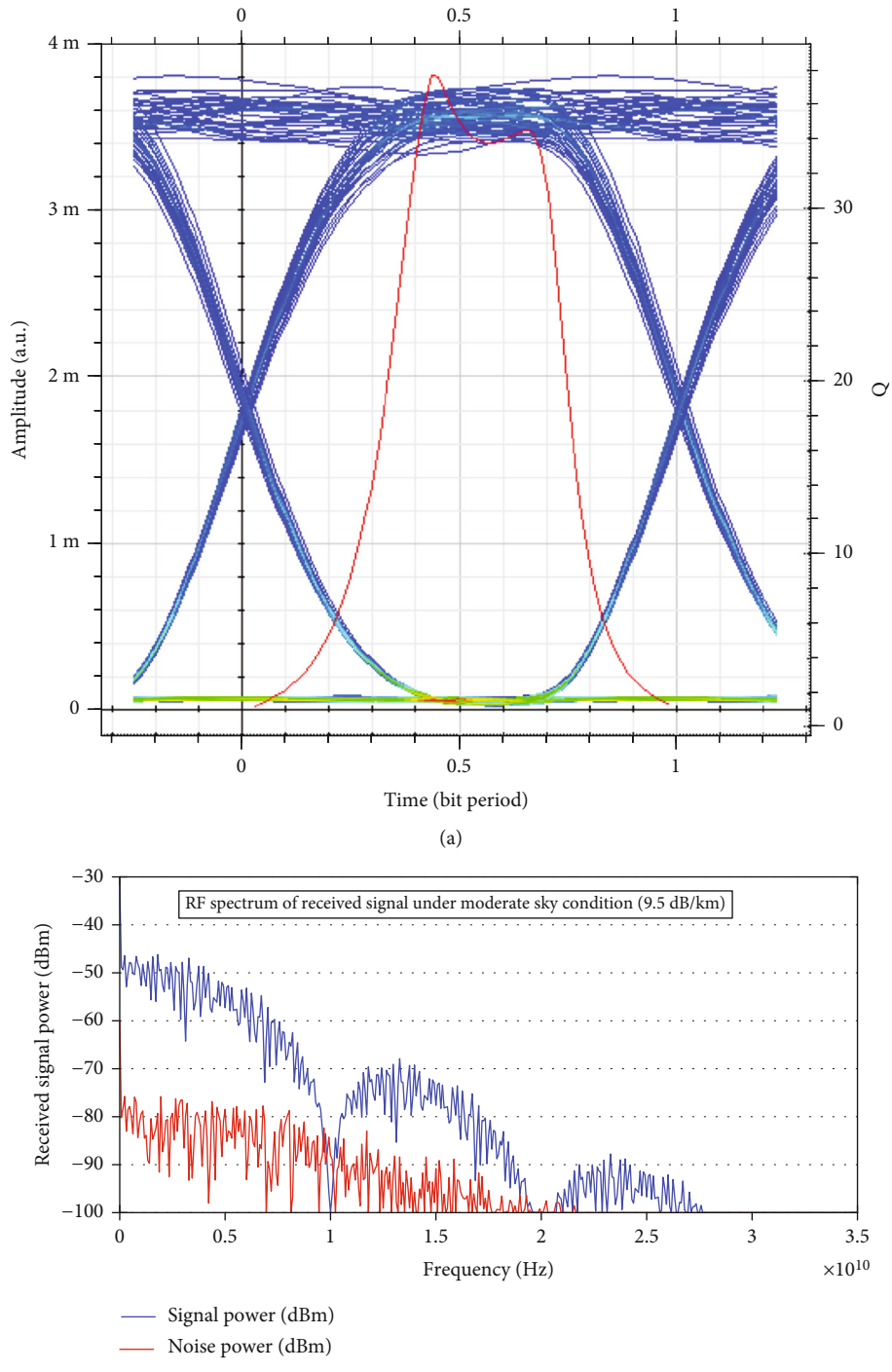

Figure 13: (a) Eye diagram under moderate sky condition. (b) Signal power and noise power spectrum under moderate condition.

between transmitter power and link distance [33]. This relationship between link distance (km) and received optical power is simulated under clear (0.1 dB/km), moderate (9.5 dB/km), and high attenuation (18.99 dB/km) conditions illustrated in Figure 8. It is observed that the reduction of received optical power was significant under high attenuation conditions, reducing the link margin for the 10Gbps communication rate for a link distance of 2.5 km. Data statistics are for 2.5 km link distance under clear, moderate, and high attenuation conditions, and minimum received powers are 21.1 dBm, -2.404 dBm, and -26.15 dBm. Under clear and moderate attenuation conditions, range, data rate, and reliability are not affected. But under high attenuations, FSO communication system performance is tainted and become unreliable.

Figure 9 illustrates a relationship between log BER and link distance under various attenuation conditions (clear, moderate, and high attenuation). For a reliable communication link, the BER rate must not be greater than the value of

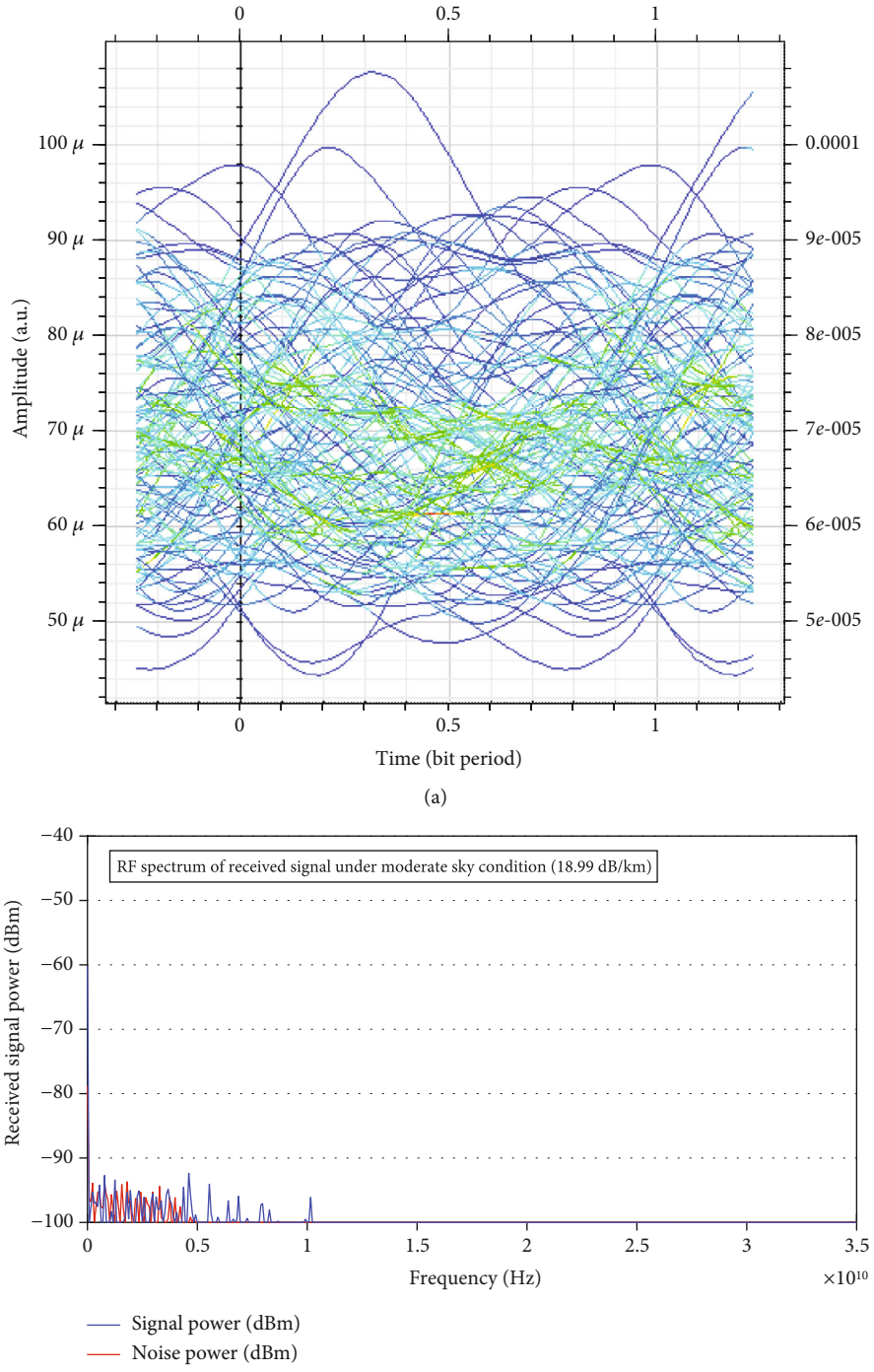

FIGURE 14: (a) Eye diagram under higher attenuation condition (b) Signal power and noise power spectrum under higher attenuation condition.

TABLE 4: Data statistics of dual-beam FSO channel for link distance of 2.5 km at 193.1THz.

Attenuation (dB/km)	Received optical power (dBm)	Quality of signal (min)	Bit error rate (max)	OSNR (dB) Minimum	RF_C (Hz) Maximum
Clear sky (0.1 dB/km)	21.1	415	Low (0)	3.96	$3.199x10^{11}$
Moderate attenuation (9.5 dB/km)	-2.404	40.7	$8.81x10^{-304}$	-0.6145	$3.199x10^{11}$
High attenuation (18.99 dB/km)	-21.15	0	High (1)	-3.96	$3.199x10^{11}$

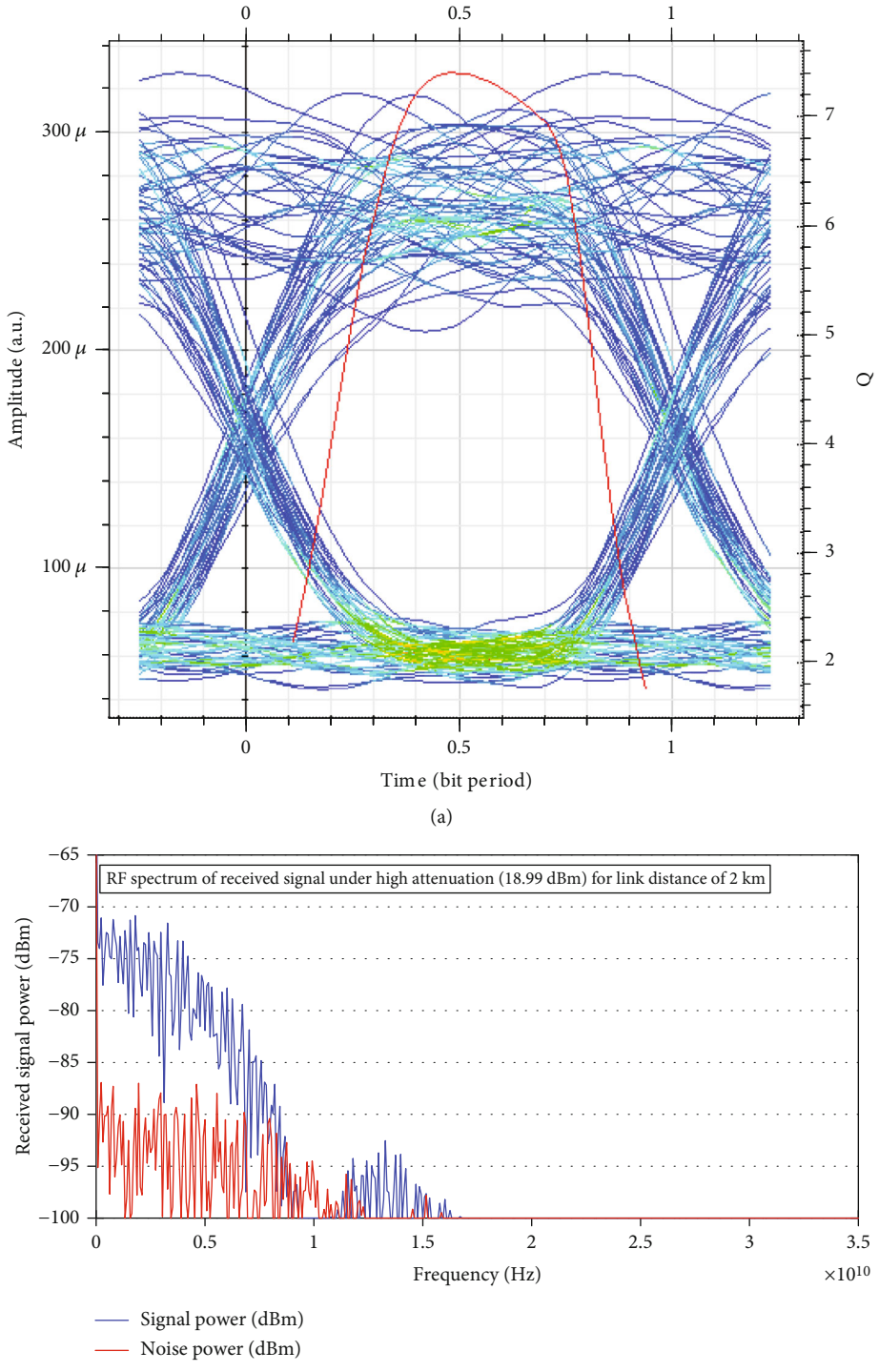

Figure 15: (a) Eye diagram under higher attenuation condition for 2 km link distance. (b) Signal power and noise power spectrum under higher attenuation condition for 2 km link distance.

Table 5: Data statistics of dual-beam FSO channel for link distance of 2 km at 193.1 THz.

Attenuation (dB/km)	Received optical power (dBm)	Quality of signal (minimum)	Bit error rate (maximum)	OSNR(dB) Minimum	RF_C (Hz) Maximum	Signal power (dBm)	Noise power (dBm)
High attenuation (18.99 dB/km)	-14.86	7.86	2.609×10^{-15}	-0.512	3.199×10^{11}	-56.06	-60.15

$1x10^{-9}$ is considered ideal [34]. It has been observed in this study that BER and link distance are proportional to each other, as illustrated in Figure 9. Under clear and moderate attenuation conditions, the communication link remained reliable for up to a link distance of 2.5 km with zero and $8.81x10^{-304}$, respectively. For under higher attenuation of 18.99 dB/km, BER is very high and has limited the reliability of the communication link.

The Q-factor is another performance evaluation parameter for the FSO communication system. A reliable optical communication link depends on BER and Q-factor, which are contrariwise with each other. Q-factor decreases with an increase in link distance. Q-factor of dual-beam FSO communication link is reliable under clear and moderate attenuation conditions for 2.5 km link distance with minimum values of approximately 464 and 42.89. This system becomes unreliable under high attenuation conditions for link distance up to 2.5 km with a minimum Q-factor of zero. OSNR is another performance monitoring parameter considered for the evaluation reliability of an optical communication system. The OSNR and BER are inversely proportional to each other so that a good and reliable FSO communication link has higher OSNR, higher Q-factor, and lower BER. A comparison of OSNR and link distance at different attenuations is illustrated in Figure 10. Under a clear sky and moderate attenuation conditions, a dual-beam FSO communication design is suitable for up to 2.5 km link with minimum values of 3.96 and -0.6145 but, under higher attenuation, OSNR reduces to -3.962 dB. As link distance increases, OSNR decreases due to the noise lumped in the optical communication link.

This noise is an unwanted, undesired signal produced due to electronic signal processing in optical communication devices, lightning in the environmental channel, and background noises. These noise sources also corrupt the channel estimations [35]. In this simulation, the CW laser has noise dynamics of 3 dB and optical amplifiers with 4 dB noise figures for each FSO channel. Such thermal noise reduces the OSNR of the FSO communication system. Figure 11 illustrates the log noise correlation ship with link distance. Noise signal increases with an increase in link distance under different attenuations. In clear and moderate attenuation conditions, the maximum value of log noise is 0.01403 dBm and 2.367 dBm, and under higher attenuation conditions value of log, noise power is 22.35 dBm.

The quality of the received signal is observed through performance evaluating factors Q-factor, OSNR, BER signal, and noise power of the dual-beam FSO communication system. Figures 12–14 illustrate performance under clear, moderate, and higher attenuation conditions. The eye diagram analyzer and BER analyzer were used to evaluate the quality of the received signal. The bit pattern under clear sky conditions with signal power and noise power is illustrated in Figure 12. It is observed that the pattern of the bits is very compact and tells a good quality of the signal at maximum radio frequency (RF) $3.199x10^{11}$ Hz with a very high Q-factor of 415 and zero BER mentioned in Table 3, whereas the received signal and noise observed by using an RF-spectrum analyzer are 15.58 dBm and -52 dBm given in Table 3. The attenuation has degraded the communication system performance so received power is reduced to -31.42 dBm with noise power of -60 dBm. If atmospheric attenuation increases, the performance of the system decreases. Figure 13 illustrates the performance of the system under a moderate attenuation condition. The pattern of the transmitted bits looks scattered due to moderate attenuation conditions with a de-shaped eye diagram. The Q-factor reduces to 40.7 with a BER of $8.81x10^{-304}$ n in Table 4.

Under higher attenuation conditions, the reliability of this communication system is badly affected as illustrated in Figure 14. The received optical power reduced to -21.15 dBm also reduces Q-factor to zero (0) and increases BER to high (1) as given in Table 4. The eye diagram shows a highly scattered bits pattern. This system under higher attenuation is no more reliable for a data rate of 10 Gbps. The effect of reducing received power can observe from the received power of -78.8 dBm with noise power of -60.18 dBm. It is observed that the communication system for a data rate of 10 Gbps is not reliable for this range or link distance (2.5 km).

The dual-beam FSO system data statistics show that under higher attenuation conditions, 10 Gbps data can be transmitted successfully with reliability up to a 2 km link distance with a Q-factor of 7.86 as illustrated in Figure 15.

The performance evaluating factors OSNR and BER are 0.512 dB and $2.609x10^{-15}$, with reasonable and acceptable received signal power of -56.06 dBm and noise power of -60.15 dBm and bit pattern as given in Table 5.

5. Conclusions

In this paper, the authors analyzed and proposed a dual-beam FSO communication system. The performance of the dual-beam FSO system has been studied and examined under the rain and suspended dust concentration attenuation conditions. The performance of the dual-beam FSO communication link has a degrading impact under rainy and dusty environmental conditions. More the rain rate offers high optical attenuation by absorption and scattering the transmitted signal. Similarly, higher values of the dust or aerosol particles definitely have higher absorption and scattering effect. A reliable, higher data rate (10 Gbps) communication link can be maintained for attenuation value up to 9.5 dB/km for a link distance of 2.5 km transmitted power (30 dBm) with a Q-factor of 40.7 with zero (0) BER. The higher attenuation reduces the reliability by affecting the link distance between the optical transmitter and receiver. It is observed that a reliable and efficient dual-beam FSO communication link can be implemented for up to 2 km with a data rate of 10 Gbps for Lahore airfield under attenuation of 18.99 dB/km with a Q-factor of 7.86 and BER of $2.609x10^{-15}$ but higher attenuation can degrade the performance of a dual-beam FSO communication link by increases BER, reduces Q-factor and OSNR, and making the system unreliable. This research will be helpful in designing a high-speed data metropolitan FSO communication network to interconnect different institutions, colleges, and universities in the future.

Data Availability

The simulation data used to support the findings of this study are available from the corresponding author upon request.

Conflicts of Interest

The authors declare that they have no known competing financial interests or personal relationships that could have appeared to influence the work reported in this paper.

References

[1] A. T. Trinh, T. C. Thang, and A. T. Pham, "Mixed mmWave RF/FSO relaying systems over generalized fading channels with pointing errors," *IEEE Photonics Journal*, vol. 9, no. 1, pp. 1–14, 2016.

[2] M. M. Abadi, Z. Ghassemlooy, S. Zvanovec, M. R. Bhatnagar, M.-A. Khalighi, and Y. Wu, "Impact of link parameters and channel correlation on the performance of FSO systems with the differential signaling technique," *Journal of Optical Communications and Networking*, vol. 9, no. 2, pp. 138–148, 2017.

[3] B. R. Strickland, M. J. Lavan, E. Woodbridge, and V. Chan, "Effects of fog on the bit-error rate of a free-space laser communication system," *Applied Optics*, vol. 38, no. 3, pp. 424–431, 1999.

[4] T. Kamalakis, I. Neokosmidis, A. Tsipouras, T. Sphicopoulos, S. Pantazis, and I. Andrikopoulo, "Hybrid free space optical / millimeter wave outdoor links for broadband wireless access networks," in *2007 IEEE 18th International Symposium on Personal, Indoor and Mobile Radio Communications*, pp. 1–5, Athens, Greece, 2007.

[5] N. Letzepis and A. I. Fabregas, "Outage probability of the Gaussian MIMO free-space optical channel with PPM," *IEEE Transactions on Communications*, vol. 57, no. 12, pp. 3682–3690, 2009.

[6] M. A. Khalighi and M. Uysal, "Survey on free space optical communication: a communication theory perspective," *IEEE Communications Surveys & Tutorials*, vol. 16, no. 4, pp. 2231–2258, 2014.

[7] A. Arnulf, J. Bricard, E. Curé, and C. Véret, "Transmission by haze and fog in spectral region 0.35 to 10 microns," *Journal of the Optical Society of America*, vol. 47, no. 12, pp. 491–498, 2001.

[8] M. Achour, "Simulating atmospheric free-space optical propagation; part II: haze, fog, and low clouds attenuations," in *Proceedings of SPIE*, vol. 4635, Boston, MA, USA, 2002.

[9] M. Achour, "Free-space optics wavelength selection: 10u versus short wavelengths," *Proceedings of SPIE*, vol. 5160, pp. 1–15, 2003.

[10] J. E. Wainright, H. H. Refai, H. Hazem, and J. J. Sluss, "Wavelength diversity n free-space optics to alleviate fog effects," *Proceedings of SPIE*, vol. 5712, pp. 110–118, 2005.

[11] A. Amphawan and S. Chaudhary, "Free-space optical mode division multiplexing for switching between millimeter-wave picocells," in *SPIE Proceedings*, Singapore, 2015.

[12] N. Ahmad, K. Hussain, N. Ahmad, M. Khaleeq-ur-Rahman, and A. Hussnainn, "A study of concentration of Lahore (Pakistan) suspended particulates and their trace elemental loadings," *World Applied Sciences Journal*, vol. 32, pp. 1952–1961, 2014.

[13] S. M. Yasir, M. Salman, and M. S. Saleem, "Critical events of fog attenuation using visibility data in Lahore, Pakistan," *NUST Journal of Engineering Sciences*, vol. 11, no. 2, pp. 41–50, 2018.

[14] H. Zhang, X. Tang, B. Lin et al., "Performance analysis of FSO system with different modulation schemes over gamma-gamma turbulence channel," in *17th International Conference on Optical Communications and Networks (ICOCN 2018)*, p. 83, Zhuhai, China, 2019.

[15] S. M. Yasir, N. Abas, and A. M. S. Saleem, "Performance analysis of 10Gbps FSO communication link under suspended dust and rain conditions in Lahore, Pakistan," *Nonlinear Optics, Quantum Optics: Concepts in Modern Optics*, vol. 50, no. 4, 2019.

[16] M. C. Baddock, C. L. Strong, J. F. Leys, S. K. Heidenreich, E. K. Tews, and G. H. McTainsh, "A visibility and total suspended dust relationship," *Atmospheric Environment*, vol. 89, pp. 329–336, 2014.

[17] G. K. Hemani Kaushal, "Free space optical communication: challenges and mitigation techniques," 2015, https://arxiv.org/abs/1506.04836.

[18] A. Kumar, A. Dhiman, D. Kumar, and N. Kumar, "Free space optical communication system under different weather conditions," *IOSR Journal of Engineering*, vol. 3, no. 12, pp. 52–58, 2013.

[19] M. B. Awan and S. Mohan, "Balloon mesh free space optical communication with tracking and link switching," in *2015 17th International Conference on Transparent Optical Networks (ICTON)*, pp. 1–4, Budapest, Hungary, 2015.

[20] T. Cseh and T. Berceli, "Dispersion compensation in millimeter wave radio over multimode fiber systems," *Microwave and Optical Technology Letters*, vol. 57, no. 1, pp. 204–207, 2015.

[21] S. R. B. K. Appaiah, R. Salas, S. Vishwanath, and S. R. Bank, "Offset coupling, feedback, and spatial multiplexing in 4×4 incoherent-MIMO multimode fiber links," *Journal of Lightwave Technology*, vol. 31, no. 17, pp. 2926–2939, 2013.

[22] N. A. N. Khan and N. Abas, "Design of an optical clock repetition rate multiplier," *Nonlinear Optics, Quantum Optics: Concepts in Modern Optics*, vol. 48, no. 1, pp. 29–39, 2016.

[23] M. T. Mushtaq, S. M. Yasir, M. S. Khan, A. Wahid, and M. S. Iqbal, "Analysis of internal design parameters to minimize geometrical losses in free-space optical communication link," *Acta Physica Polonica A*, vol. 134, no. 1, pp. 275–277, 2018.

[24] M. Singh, J. Malhotra, M. S. Mani Rajan, V. Dhasarathan, and M. H. Aly, "Performance evaluation of 6.4 Tbps dual polarization quadrature phase shift keying Nyquist-WDM superchannel FSO transmission link: Impact of different weather conditions," *Alexandria Engineering Journal*, vol. 59, no. 2, pp. 977–986, 2020.

[25] S. Chaudhary, A. Amphawan, and K. Nisar, "Realization of free space optics with OFDM under atmospheric turbulence," *Optik*, vol. 125, no. 18, pp. 5196–5198, 2014.

[26] F. K. Shaker and M. A. A. Ali, "Multi-beam free-space optical link to mitigation of rain attenuation," *Journal of Optical Communications*, vol. 42, no. 2, pp. 235–240, 2021.

[27] F. S. A. A. Farouk Kh, M. A. Shaker, and A. Ali, "Utilization of MIMO concept for optical communication system under fog condition," *ECTI Transactions on Electrical Engineering, Electronics, and Communications*, vol. 17, no. 2, pp. 130–135, 2019.

[28] K. N. Blaunstein, A. Shlomi, and A. Zilberman, *Applied Aspects of Optical Communication and Lidar*, CRC Press, 1st edition, 2009.

[29] M. A. Esmail, H. Fathallah, and M.-S. Alouini, "An experimental study of FSO link performance in desert environment," *IEEE Communications Letters*, vol. 20, no. 9, pp. 1888–1891, 2016.

[30] K. E. Kim II and B. McArthur, "Comparison of laser beam propagation at 785nm and 1550nm in fog and haze for optical wireless communications," in *Proceeding SPIE 4214.Optical Wirel. Commun.*, Boston, MA, 2001.

[31] S. Bloom, E. Korevaar, J. Schuster, and H. Willebrand, "Understanding the performance of free-space optics [Invited]," *Journal of Optical Networking*, vol. 2, no. 6, p. 178, 2003.

[32] N. Garg and S. Kumar, "Design of free space optical communication link with Mach-Zehnder optical modulator for long distance," in *2013 Fourth International Conference on Computing, Communications and Networking Technologies (ICCCNT)*, pp. 1–5, Tiruchengode, India, 2013.

[33] S. M. Yasir, N. Abas, A. Rahman, and M. S. Saleem, "Simulation analysis of adaptive FSO/RF hybrid link under diverse weather conditions of Lahore, Pakistan," *Results in Optics*, vol. 2, article 100047, 2021.

[34] A. K. Majumdar and J. C. Ricklin, *Free-Space Laser Communications*, Springer Science, New York, 2008.

[35] A. Khatoon, W. G. Cowley, and N. Letzepis, "Channel measurement and estimation for free space optical communications," in *2011 Australian Communications Theory Workshop*, pp. 112–117, Melbourne, VIC, Australia, 2011.

Hindawi
Wireless Communications and Mobile Computing
Volume 2022, Article ID 3150756, 11 pages
https://doi.org/10.1155/2022/3150756

Research Article

SDN-Driven Internet of Health Things: A Novel Adaptive Switching Technique for Hospital Healthcare Monitoring System

Barbaros Preveze,[1] Ahmed Alkhayyat,[2] Firas Abedi,[3] Aqeel Mahmood Jawad,[4] and Ali S. Abosinnee[5]

[1]*Department of Electrical and Electronics Engineering, Cankaya University Ankara, Turkey*
[2]*Computer Technical Engineering Department, College of Technical Engineering, The Islamic University, Najaf 54001, Iraq*
[3]*Department of Mathematics, College of Education, Al-Zahraa University for Women, Karbala, Iraq*
[4]*Communication Engineering Department, Al-Rafidain University College, 10014 Baghdad, Iraq*
[5]*Altoosi University College, Najaf, Iraq*

Correspondence should be addressed to Ahmed Alkhayyat; ahmedalkhayyat85@iunajaf.edu.iq

Received 28 February 2022; Revised 9 May 2022; Accepted 17 May 2022; Published 15 June 2022

Academic Editor: Ghanshyam Singh

In the last decent, the number of Internet of Things (IoT) health-based paradigm reached to a huge number of users, services, and applications across different disciplines. Thus, hundreds of wireless devices seem to be distrusted over a limited or small area. To provide a more efficient network, the software-defined network (SDN) thought to be a good candidate to deal with these huge number of wireless users. In this work, after a novel SDN algorithm is proposed for the hospital environment, it is also designed and integrated into an Internet of Health Things (IoHT) paradigm. The novel algorithm called adaptive switching (AS) is proposed as a novel adaptive access strategy based on adaptively hoping among existing Go-Back-N and Selective Repeat techniques. Finally, the throughput performance of the proposed AS method is compared with the performances of traditional Go-Back-N and Selective Repeat ARQ methods using the developed MATLAB simulation. For this, an optimal P_{error} rate that the network should prefer to switch either from Go-Back-N to Selective Repeat or from Selective Repeat to Go-Back-N method to maximize the network throughput performance is determined. The evaluated results are also confirmed by theoretical calculation results using well-known Mathis throughput formula. It is observed from the simulation results that the best throughput performance can be evaluated, when AS switches to Go-Back-N if the P_{error} is less than 3.5% and it switches back to Selective Repeat when the P_{error} is greater than 3.5%. By this way, it is also observed that the throughput always has its best possible results for all P_{error} rates and up to 37.52% throughput improvement is provided by the use of novel proposed adaptive switching (AS) algorithm.

1. Introduction and Related Work

1.1. Introduction. The IoT is a rapidly evolving ecosystem that connects hardware, computing devices, physical items, software, and animals or humans over a network, allowing them to interact, communicate, gather, and share data [1, 2]. From industrial applications to e-healthcare applications, there are many distinct kinds of IoT services [3–5].

In [6], the authors introduced the development in the rising technologies and the framework for EC-IoT-based SG (edge computing for IoT-enabled smart grid), with its implementation requirements. And in [7], the authors provide the current operations of the healthcare system and discuss the mapping of these operations into the architectural diagram. Smart wearable/implant sensors, machine devices connected to or within a human body for monitoring in a hospital digital healthcare system, are the goal of this study, to gather data about the person's state of health for heartbeat, blood pressure, glucose level, etc., via the technologies of wearable sensors [8]. The overall proposed structure of the software-defined network-driven Internet of Health Things paradigm is given in Figure 1. In this figure, the

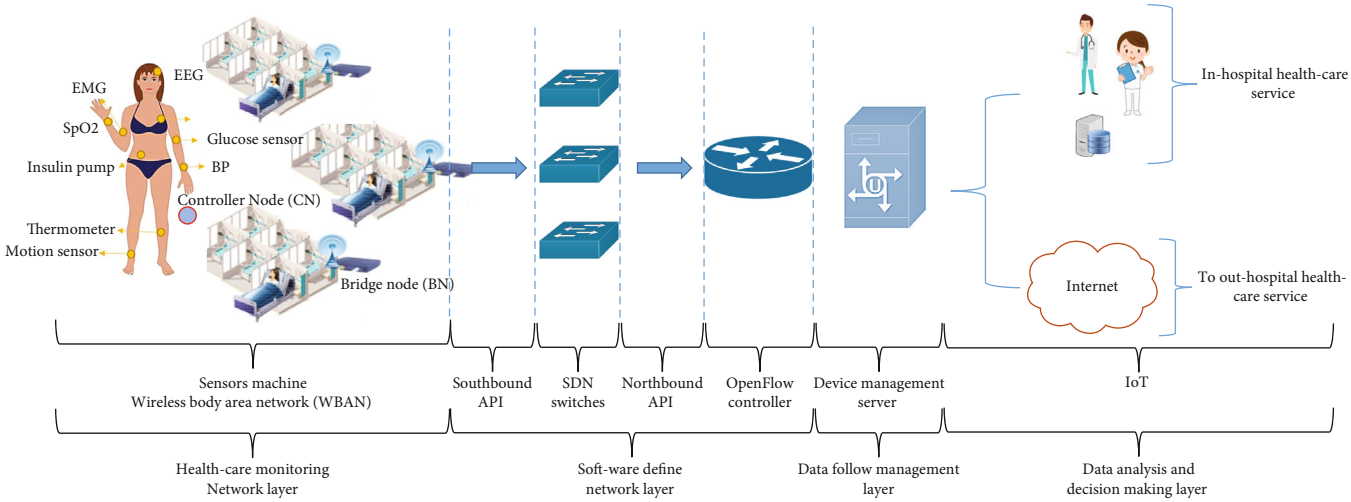

Figure 1: Proposed structure of the software-defined network-driven Internet of Health Things (SDN-IoHT) paradigm.

end-to-end (ETE) data flow in the proposed structure can easily be followed.

The control types of wireless body sensors used in hospital-based healthcare applications can be categorized into 3 subcategories as centralized control, decentralized control, and distributed control types [9]. In the case where the single node in a centralized control system has a global view and knowledge of the network, and it decides whether a node's functionality is required or not, the node should be active or inactive. In the case of the having a noncentralized control system, the categorization of the nodes will be done in several groups where there will certainly be a single node in each group (as the central node). The activity of these nodes is determined by interactions among the core nodes of different groups. When the distributed control is in use, there will be no grouping or no central control nodes, and also for network-wide decision-making, such as selecting the active nodes over the network region, all the nodes in the network will communicate with each other dynamically.

In this work, the throughput performance of decentralized control of wireless body sensors in hospital-based healthcare applications is investigated. And, since the SDN really does distinct from the control plane to the data plane, it is considered to be a good candidate for controlling such a network; thus, a new structure for SDN-driven Internet of Things is proposed for e-health applications.

In Figure 1, a multifloored hospital building structure is considered with several sections distributed in each floor of the hospital, where each of these sections consists of at least six and up to seven patient beds. The machine sensors are connected to the whole body of the patient to monitor his/her biological or vital signals and their other activities. Each of these sensors is also equipped with a wireless transceiver, and the gathered data are transmitted to the controller node over the wireless channel (each patient has his/her own single controller node which is located close to him but not attached to his/her body) using the standard of IEEE 802.15.6. The most important function of the controller node (CN) is to receive the data and transmit it to the bridge node (BN). In this work, the layer up to this point is called as "the healthcare monitoring network layer" or "the data plane layer."

The second layer above the first one is "the software-defined network (SDN) layer," for which the healthcare monitoring network layer can be considered as the data plane for it. In each of the sections, the data are collected and transmitted to the BN either by a multihop or by a single hop. Then, the SDN controller selects the appropriate path for the data gathered by the CN over the hop or multihop and delivers them to the BN using IEEE 802.15.6 standard (the sensors collect data, which is then sent to the controller based on 802.15.6 standard). However, to increase the system performance, the CN will also use the novel proposed technique called "adaptive switching (AS) technique" as the second function of the SDN controller.

The third layer which is called "the IoT layer" is in charge of the data follow management and the making of decision. The data are forwarded either to the healthcare services inside the hospital (and represented by doctors or nurses before being stored in the data storage devices) or to other hospitals and the intelligent cloud system over the Internet.

The main contribution of this work is done on the data link layer of OSI (open systems interconnection) model where a novel adaptive switching (AS) technique is proposed which is a combination of traditional automatic repeat request protocols. This technique is simulated on a hospital healthcare monitoring system to be used with the SDN-driven Internet of Health Things (SDN-IoHT). As the result of this work, it is shown that the throughput performance of hospital healthcare monitoring system is improved by the proposed technique.

The major contributions provided in this work can be summarized as follows:

(i) An SDN-driven Internet of Health Things (SDN-IoHT) network is designed for the hospital monitoring system in real time which comprised of three layers, "healthcare monitoring network layer," "SDN layer," and "IoT" layer

Table 1: State of Arts Comparison.

Pub. year [ref. no.]	Protocols/methods	Metrics	Highlight
2019 [10]	SDN routing based	(i) Throughput (ii) End-to-end delay (iii) Energy consumption (iv) Successful transmission	(i) Proposed an energy-aware and controller-based routing algorithm (SDN routing) with a new interface protocol (WBAN flow) (ii) Proposed a new architecture consisting of data, control, and application planes for the SDN-based WBAN environment
2018 [11]	Software-defined WBAN (SDWBAN)	—	(i) Proposed new framework based on lack of current WBAN architectures and challenges such as heterogeneous WBAN traffic handling, static architecture, mobility management, traffic priority management, secured authentication, network reconfiguration, energy efficiency
2017 [12]	Software-defined network-service function chain (SDN-SFC)	(i) Total distance (ii) Overload (iii) Time cost	(i) Proposes combined software-defined network-service function chain (SDN-SFC) with heuristic SA algorithm to reduce IoT health-based data transmission time (ii) Considering load-balancing for remote healthcare system
2015 [13]	SDN-cloud computing (CC) based	—	(i) Generalized software-defined cloud-based architecture for virtual hospital has been proposed (ii) Future possible open research issues and challenges have been discussed to provide an interesting and enormous research effort for near future
2015 [14]	Centralized controller using SDN	Response time	(i) Proposed a design of the elastic health IoT structure, which deals with both intelligent health monitoring and emotional care (ii) A health IoT framework with software defined is proposed which separates the application from the underlying physical infrastructure (iii) Proposed framework enables elastic control and management of the physical infrastructure and speeds up the innovation of various healthcare applications

(ii) The novel proposed switching technique called adaptive switching (AS) which makes switching among one of the traditional Go-Back-N and Selective Repeat methods according to the packet error rate of the network at an instant is simulated, and it is shown that the throughput performance of real-time hospital monitoring system is improved

(iii) Additionally, a multihop technique is also utilized to present alternative paths to CN and to overcome the direct transmission failures

The rest of the paper is organized as follows.

The MAC protocol of the Go-Back-N and selective repeat ARQ is explained in Subsection 2.1; then, in Subsection 2.2, the proposed adaptive switching (AS) technique is described. In Section 3, the evaluated simulation results and the provided throughput performance improvement are presented. Finally, in Section 4, conclusions are made and future research approaches are suggested.

1.2. Related Work. The limitations of the proposed frameworks/design/algorithms in Table 1 are as follows:

(i) Single work considered the important metric quality of service which represented by throughput in the SDN environment for healthcare applications

(ii) None of the previous work consider the packet error rate in the SDN environment for healthcare application

(iii) Finally, none of the previous work design framework that taken into account MAC protocol in the SDN environment for healthcare applications

Only a few research has been done on the SDN healthcare-based paradigm thus far. SDN is a promising technology that defines new network communication design and management techniques. Despite the fact that it is a broad emergency, IoHT is still in its infancy, with a huge field of study for different issues such as scalability and heterogeneity, with existing IoHT paradigm and so forth.

In [10], for the healthcare paradigm, a WBSN architecture based on the SDN paradigm with a novel energy-aware routing algorithm is presented. As a result, for e-healthcare architecture, a WBSN architecture based on the SDN method with a novel energy-aware routing algorithm is presented and built.

In [11], a framework for software-defined WBAN (SDWBAN) is designed and proposed that brought the idea of SDN technologies into WBAN applications. By this concept, decoupling the control plane from the data plane and having more programmatic control would assist to remedy the current deficiencies and challenges of WBAN.

In [12], the use of SDN is proposed in addition to service function chain (SFC), and instinctive simulate annealing (SA) methods, in e-health service networks, decrease the time it takes for IoT data to be transmitted. The SA technique is proven to be more effective in reducing data transmission time for multiple users; however, the greedy algorithm looks like a good candidate for more users. They designed a side-by-side e-health network by the proposed methods.

In [13] for WBSN, a virtual hospital architecture based on SDN is recommended. The inclusion of cloud architecture into WBSN for virtual hospital architectural ideas leads in a new and fundamental architecture that may benefit from SDN and reduce the intricacy of cloud architecture.

[14] proposes and presents a flexible network architecture that can handle intelligent health monitoring and emotional care. Particularly, an architecture based on an SDN system named e-health IoT is developed through separating the application plane from the physical infrastructure. The healthcare services acquire the ability to customize, transfer, and process their own gathered data. Several applications are permitted on a shared infrastructure due to emotion feedback via well-defined APIs, lowering total expenses. The physical infrastructure may also be controlled and managed in a flexible manner. In the study, the application plane of the proposed architecture is focused on.

In [15], a secure IoHT system that is integrated with the WBAN is demonstrated and investigated. Reliable cryptoprimitives were applied to make dual communication systems which could be guaranteed the transmission privacy as well as build an entity authentication for the machine sensors, the CN, and the edge of the network.

In [16], low-power consumption, transmission reliability, latency, data speeds, and security are all examined in the WBSN domain. Furthermore, the authors examined the needs and requirements of WBAN in a traditional e-healthcare system in order to determine how such systems are able to communicate effectively in the home environment network.

[17] presents and investigates a mathematical equation for the in-body to off-body channel statistical model, which may explain the signal traveling between the transmitter and receiver antennas. The research is based on a three-dimensional virtual human body model.

The authors looked at a novel design of IoT e-healthcare paradigms in [18], which they called a secure e-healthcare IoT-based paradigm for BSN-care.

In [19], the nonstatic e-healthcare IoT paradigms are suggested with an end-to-end security mechanism. The authors of the study used the idea of fog layers in IoT to provide seamless mobility for the fog extending the cloud system to the network's edge.

In [20], the applications of IoT in the e-healthcare industries are investigated and presented, revealing the intelligentization trend of future research in e-healthcare IoT-based paradigms.

An on-body sensor device with solar energy harvesting and a low-power transmission paradigm is explored in [21], allowing for the implementation of an autonomous WBSN. Furthermore, the information gathered from the human body is shown on a web-based smartphone application.

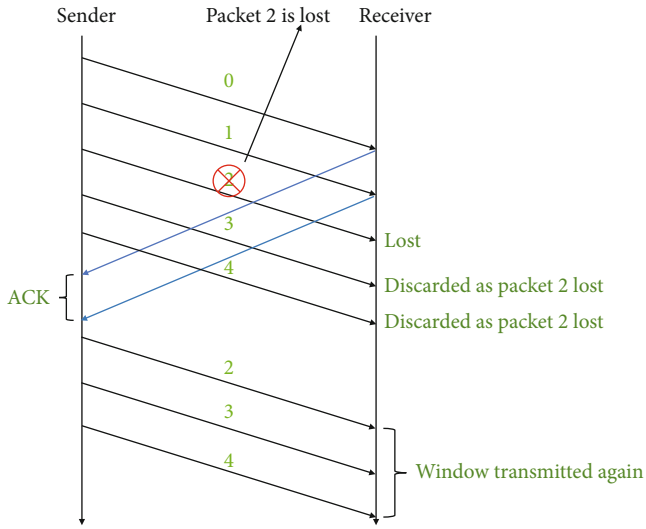

Figure 2: The working principle of the Go-Back-N method.

The effect of power allocation and packet size determination on the performance of an e-healthcare IoT-based system is addressed and studied in [22] for the wireless medium. Three protocols are suggested in the study: a power level decision, a power level and packet size choice, and a global link decision.

A new IoT-aware smart hospital system is introduced in [23]. The proposed system is capable of handling emergency circumstances effectively. Interoperability has been a major challenge for IoT researchers and developers.

But in [24], an IoT-based semantic interoperability paradigm is proposed, which enables semantic interoperability for heterogeneous IoT devices. Doctors are able to communicate with their patients since the collected data was semantically interpreted and conveyed in a meaningful way.

[25] establishes a developed concept connecting cloud computing and IoT: cloud IoT-health (CC-IoT) solutions. The idea of the CC-IoT is explored, as well as a number of important integration problems, in order to show a realistic vision that integrates current CC and IoT mechanisms in e-healthcare applications.

A privacy protector is suggested in [26], which safeguards the privacy of the patient data gathered. In privacy protector, the Slepian-Wolf-coding-based secret sharing is used to overcome a variety of security measures.

A type 2 fuzzy ontology–aided recommendation system for IoT-based healthcare is proposed in [27] to efficiently monitor the patient's body. This system greatly increased the accuracy of predicting a patient's condition as well as the accuracy of medical and nutritional suggestions.

In [28], harvesting energy IoT health-based paradigm has been developed, with the goal of reducing outage probability via interwireless body area network collaboration.

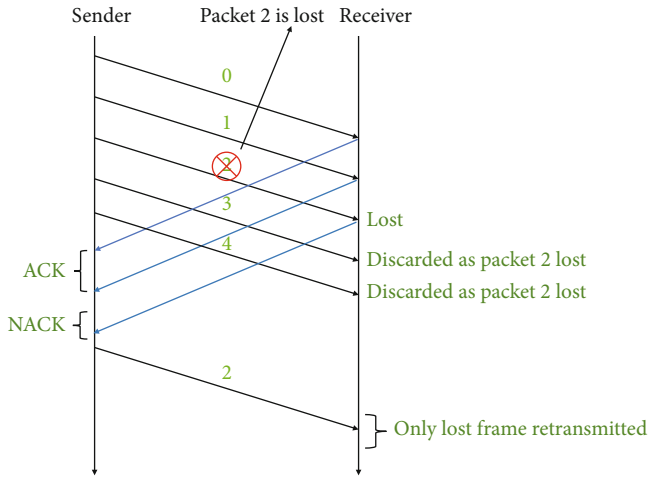

Figure 3: The working principle of the Selective Repeat method.

Finally, [29] investigates WBSN in IoT health-based applications: towards delay and energy consumption minimization.

However, to the best our knowledge, in none of these works,

(i) the developed SDN-based driven Internet of Health Things for hospital healthcare applications are considered

(ii) SDN integrates with the wireless body area network

(iii) an adaptive switching access technique has been considered for SDN-based driven Internet of Health Things

2. Proposed MAC Protocol

MAC protocols are needed to regulate communication between wireless devices over a shared medium. The commonly used wireless body area network MAC protocol is a hybrid access technique, and it comprises of carrier sense multiple access collision avoidances (CSMA/CA) and time division multiple access (TDMA) (802.15 s.6). In this work, although the intra-WBAN communication is not considered, the communication between the controller nodes and bridge node is regulated in each section of the hospital.

For this purpose, an access technique called adaptive switching (AS) is proposed in this study for determining the optimal packet loss rate that will be used to switch between Selective Repeat and Go-Back-N automatic repeat request (ARQ) methods. The proposed method is used on the controller nodes to wirelessly access the shared medium broadcasted by the bridge node.

2.1. Understanding Go-Back-N and Selective Repeat ARQ Methods. The working principles of Go-Back-N (GBN) and Selective Repeat (SR) ARQ methods [30] are given in Figures 2 and 3, respectively, for comparison. And all other parameters are also created eventually by the developed simulation program.

In Go-Back-N method, the frames are transmitted continuously and the receiver only ACKs the highest sequence-numbered frame received among the packets in the current window. Since the ACK of this packet will come back after a round-trip delay, there is also a timeout value (retransmission timer (RTT)) to decide whether to retransmit the same packet or to wait for a while. If the ACK does not arrive at the transmitter within this timeout value, the sender retransmits all the frames that are not ACKed in the current window. Thus, CWND minus N (where CWND is the current window size and N is the number of frames transmitted in the current window during the round-trip time) succeeding frames that were probably already transmitted during the round-trip delay will be retransmitted. For these retransmissions, a buffer is needed at the transmitter side and the receiver side does not have to buffer the frames. Because of these properties, GBN is more feasible and less complex and also requires less message overhead, and the unique disadvantage of it is we have to retransmit all the packets which are in the window but after the last acknowledged packet. That means GBN will waste the bandwidth in case of a packet loss but gain the bandwidth when no packet losses occur.

For the example in Figure 2 in which the window size is 3 and Go-Back-N is used, since pkt-1 is lost, only the last successfully arrived packet (ACK-0) of the window is acknowledged (ACK), so some of the next 3 packets outside the window cannot be taken in before receiving the ACK-1 and cannot be transmitted. Then, when all the packets are received and acknowledged but ACK-2 is lost on the returning way, pkt-2 will be considered as a lost packet by the system and the source node will retransmit it pct-2. This will cause unnecessary retransmissions. But on the other hand, the advantage of Go-Back-N is that we do not need to make ACK transmission from destination to source for each of the packets, and it is enough to transmit only the ACK of last received packet in the window.

However, in the Selective Repeat method for which an example is illustrated in Figure 3, even the packets are again transmitted continuously without waiting, the receiver

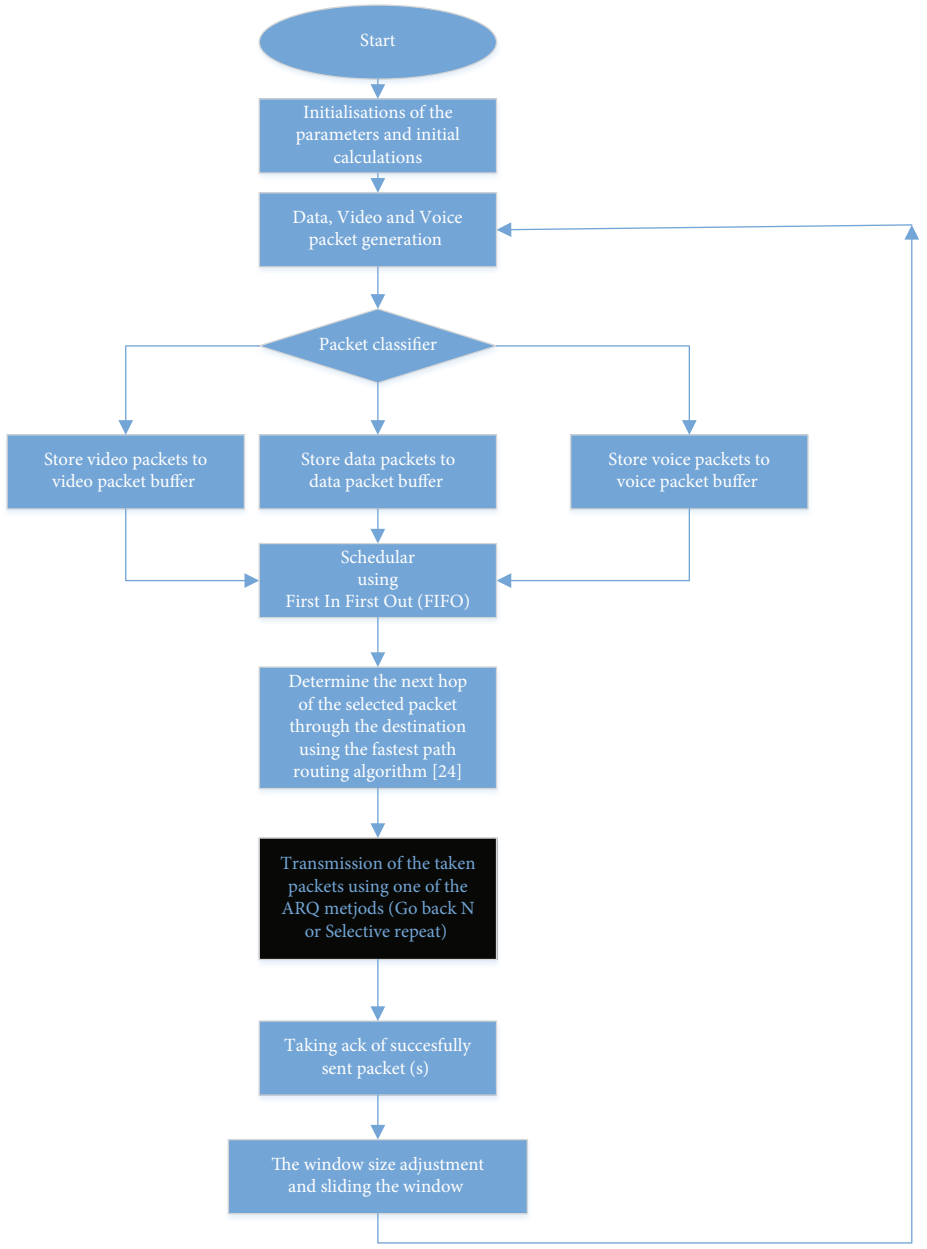

Figure 4: The flow chart of the process of proposed technique running on each controller node (CN) in the network where the sliding window that uses one of two ARQ methods is highlighted in black color.

ACKs not only the last successfully received packet but also ACKs all successfully received frames. Therefore, the transmitter will have the opportunity of retransmitting (repeating) only the unacknowledged frames when their own retransmission timers (RTT) expire. This method is known as the most efficient but also the most complex method, and buffers are needed at both transmitter and receiver sides. The disadvantage of this method is the usage of extra bandwidth for acknowledging all the packets.

Therefore, in some network conditions where there is low probability of error, Go-Back-N can be useful, but if there is more than a certain probability of error, Selective Repeat will be more useful. In this work, the proposed adaptive switching method will automatically switch between these two methods dynamically considering the current probability of error in the network.

The exact location of the proposed adaptive switching technique in the framework is given in Figure 4.

2.2. The Proposed Adaptive Switching (AS) Technique. Several studies and modifications were already made in the literature to increase the bandwidth utilization and to achieve a better quality of the network. It is known that each of the ARQ methods among "Stop and Wait" (SW) or "Go-Back-N" (GBN) and "Selective Repeat" (SR) may provide better results than others for different traffic conditions. However, at the beginning, it is not easy to predict which one will give the best results for a specific network. But since the P_{error} rate

Table 2: The parameter values used in the simulation and in the calculations.

Parameter	Value
Node number (N)	6 nodes
Buff size	1000 buffers per node
Pocket-size	1544 bytes [32]
Data rate	6 packets per sec
Receive window size (RWND)	65536 bytes [32]
Transmitter current window size (CWND)	1500 bytes (=MSS) [32]
Distance (d)	1000 km [32]
Maximum transferable unit (MTU)	1540 bytes [32]
Total header length (TCP\IP)	40 bytes [32]
Bandwidth of T3 channel (BW)	45 x 10^6 bits per sec [32]
Maximum segment size (MSS)	1500 bytes (MTU - total header length [32]
Probability of error (P_{error})	Ranging from 1% to 10% [32]
1 mile propagation delay	0.02 seconds
S threshold	65536 bytes (=RWND) [32]

of a network is a stochastically predictable and also sensible value in real time, the novel AS method is proposed to control the wireless access of the controller nodes to the shared medium by using the evaluated optimal P_{error} rate of the network to adaptively switch between different ARQ methods for the known traffic conditions.

In the use of GBN, a trade-off may be faced, such that using less ACK will increase the throughput performance, where the packets which were already sent successfully after the lost (and unACKed) packet will also be retransmitted which will cause extra retransmissions and reduced throughput performance. On the other hand, using SR may also have another trade-off such that using more ACK will decrease the throughput performance; however, the packets already sent successfully after the lost packet will not be retransmitted which will not cause a reduce on throughput performance. In this work, an adaptive access (AS) technique is proposed to switch between these ARQ methods when specified optimal P_{error} rate is experienced. For this purpose, the simulation results are evaluated using one of GBN or SR one at a time; then, it is expected to have an improved network throughput performance by dynamically switching between these methods when the system reaches to determined optimal P_{error} rate.

The flow chart of the proposed technique that is given in Figure 4 is running and controlled by the control plane of the SDN. In this figure, it is shown that each controller node forwards the packet to the bridge node based on initial calculations made by control plane in SDN and the system initializes the default simulation parameters such as buffer size, packet size, MTU (maximum transferrable unit), window size, bandwidth, and P_{error}. Then, using the specified functions, each node generates random numbers of video, voice, and data packets and stores them into their corresponding buffers. Then, the classifier function analyses the packets

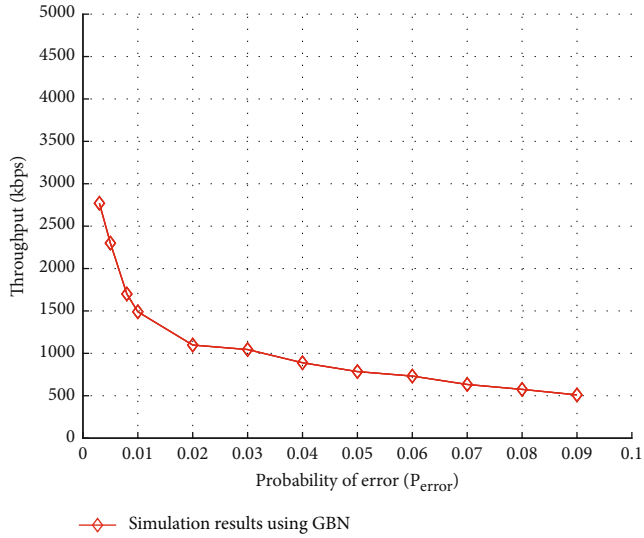

Figure 5: The evaluated expected theoretical results of expected throughput for GBN vs. different probability of error rates.

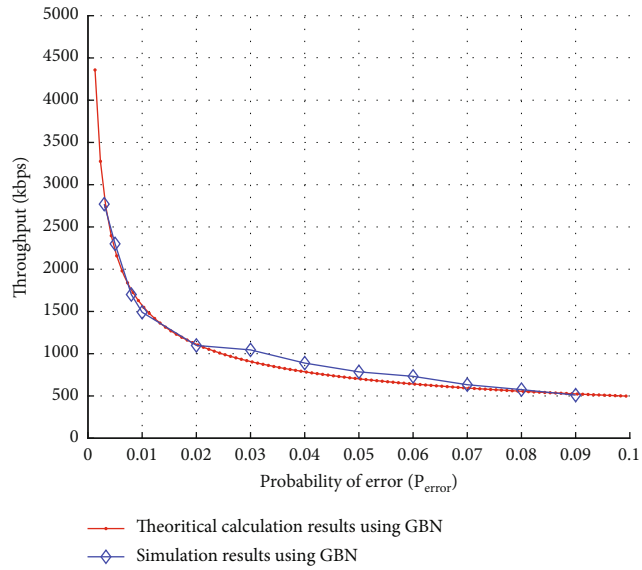

Figure 6: Confirmation of the evaluated simulation results under different packet loss rates for GBN by comparing the results evaluated using the Mathis formula.

and classifies them according to their types. Finally, the scheduler function schedules the selections of the packets from each of these buffers according to FIFO (first in first out) scheduling algorithm. Then, the fastest path routing algorithm [31] is implemented for each packet to define their routes and to transfer them to their own next nodes on their own calculated routes.

3. Simulation and Discussion

The suggested protocol's performance is assessed in this section. By this way, the developed MATLAB simulation program is used to implement the proposed AS method to provide an improvement on network throughput

```
clc
clear
hc=1;
Throughputs=zeros(1,9);
Perror=zeros(1,9);
ind=0;
perr=0.01;
WS=65536;
for i=1:hc
d(i)=1000;                  % km
end
MTU= 1540;                  % Bytes
headers = 40;               % 20 Bytes TCP + 20 Bytes IP
for i=1:hc
BW(i) = 45*10^6;            % bps for T3 Channel 45 x 10^6
end
for perr=0.0013:0.001:0.1
ind=ind+1;
Perror(ind)= (perr);        % 10^-6 for T3 Channel
MSS = MTU-headers;          % Bytes

for i=1:hc
RTT(i)= 2*d(i)/1609*0.02;   % seconds
BDP(i) = BW(i)/8*RTT(i) ;   % Required_Buffer_size
end
queuing_delay=0;
for i=1:hc
    if BDP(i) > WS && Perror(ind)~=0
    THR(i)=(MSS/RTT(i))*1/(sqrt(Perror(ind))); % the Throughput in case of Packet
losses
else
    THR(i)=(WS/RTT(i));     % the Throughput in case of NO Packet losses
end
Throughputs(i,ind)=THR(i);
end
end
sum=0;
for i=1:hc
hold on;
xlabel ('Probability of Packet Loss');
ylabel ('Evaluated Througput (kbps)');
hold on
R(i,:)=Throughputs(i,:)*8/1024/3;
sum=sum+1./R(i,:);
end
x=1./sum;
plot(Perror,x,'.-r');
axis([0 0.1 0 5*10^3]);
hold on;
grid on;
```

Figure 7: The MATLAB code used for GBN theoretical calculation results using the Mathis throughput formula.

performance. Table 2 lists the parameters used in the simulation and their default values, as well as the default values utilized in the calculations.

Figure 5 shows the evaluated throughput values versus different packet error rates ranging from 0 to 0.1 (10%). And it is seen from the graph given in Figure 5 that the TCP throughput is very sensitive to error rates and packet losses. And only an average of 1% packet loss rate restricts the TCP throughput to be less than 1500 kbps. The shape of the curve also reveals that greater loss rates dramatically affect TCP throughput too. If no packet losses occur, the window size (CWND) steadily increases until a corrupted/lost packet is detected or the RTT is over or the receiver advertises an insufficient receive buffer.

On the other hand, after the GBN and SR methods are separately simulated as event-driven MATLAB simulations, the theoretical Mathis throughput graph is also evaluated for confirmation of the evaluated simulation results and

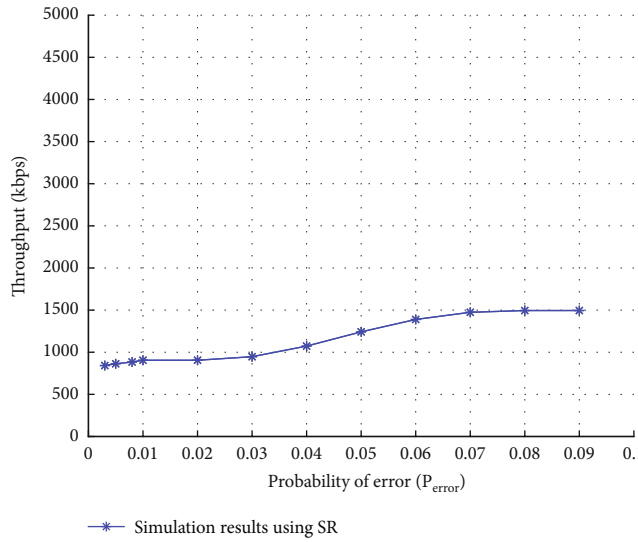

Figure 8: Evaluated simulation results under different packet loss rates for SR.

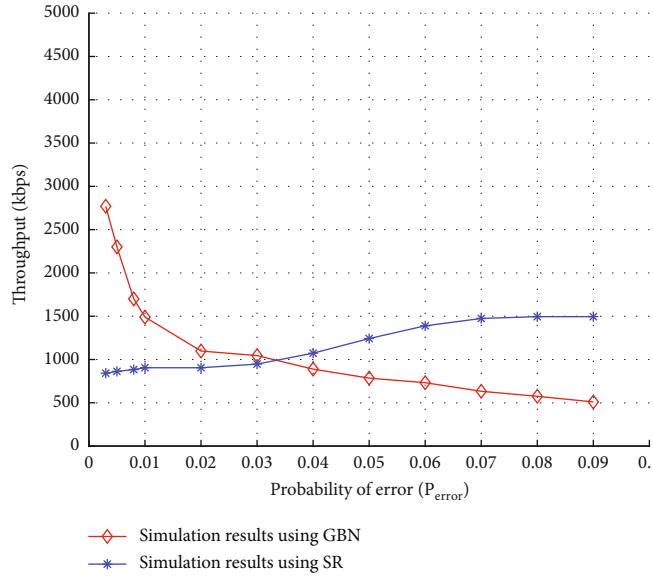

Figure 9: Comparison of the results of GBN and SR methods.

calculation results. When the simulation results are evaluated for different P_{error} rates using GBN and plotted holding on the calculation results evaluated by the Mathis formula [32, 33] for confirmation purpose, it is seen in Figure 6 that the experimental simulation results almost exactly match with the theoretically calculated throughput results.

The theoretical results in Figure 6 are evaluated analytically for GBN using the Mathis throughput formula [31] with the parameters given in Table 1 [32]. The MATLAB code implementation of theoretical calculations is given in Figure 7. On the other hand, simulation results are evaluated using a separate event-driven MATLAB simulation program in which GBN and SR methods are used. It is also shown that the evaluated outputs also match the outputs evaluated in [33].

In Figure 6 it looks like, as the probability of error increases, the throughput almost remains constant, but in fact, it just starts to slowly converge to zero throughput by the increased probability of error. Because by the time the probability of error will increase to 1 (100%), the throughput will obviously converge to 0.

On the other hand, when the simulation results are reevaluated using SR instead of GBN for the same P_{error} rate scale, it is seen in Figure 8 that the experimental simulation results tend to increase by increasing P_{error} rate.

It is seen in Figure 9 by the comparison of the evaluated simulation results under the same packet loss rate scale that GBN and SR can provide different throughput performances with different trade-offs. However, it is clearly seen from the resulting graph that GBN provides better throughput

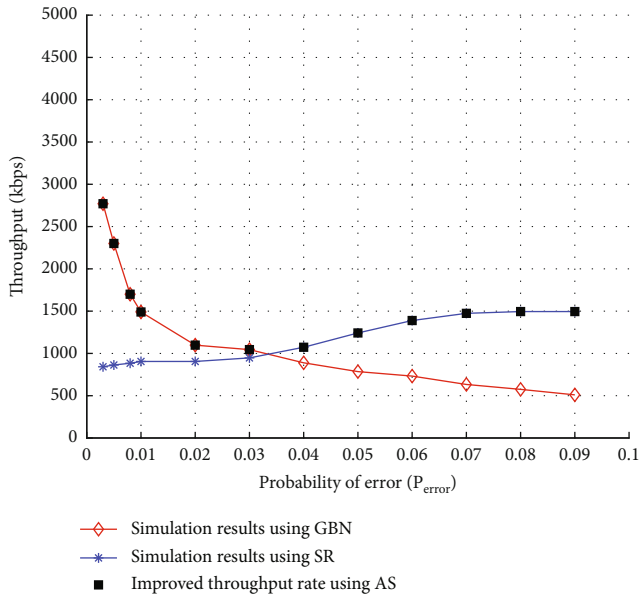

Figure 10: The evaluated simulation results under different packet loss rates for GBN, SR, and AS.

Table 3: The average amount of provided throughput improvement by the use of novel proposed AS method under different packet loss rates for GBN and SR.

	Mean throughput value (kbps)	Mean improvement W.R.T GBN	Mean improvement W.R.T SR
GBN	1219	0.00%	8.64%
SR	1122	-8.64%	0.00%
Proposed AS	1543	26.57%	37.52%

performance than SR for less P_{error} values and SR provide better performance for greater P_{error} values.

At this point, the value of P_{error} at the intersection point of throughput graphs in Figure 9 will be the crucial P_{error} value. Since the main goal of the work is maximizing the throughput performance, it is proposed for the network to switch between these two methods when P_{error} rate of the system reaches to the obtained critical P_{error} value.

Figure 10 gives the evaluated results in Figure 9 for both SR and GBN and the throughput improved by the system by using novel proposed AS method. The P_{error} rate value that the proposed AS algorithm will switch between two ARQ algorithms is also seen in Figures 9 and 10 as $P_{error} = 0.035$ where the result graphs evaluated by MATLAB simulation for GBN and SR intersect.

Since the system will periodically be aware of the packet error rates at each instance, it just decides whether the current P_{error} rate value is less than evaluated intersection point $P_{error} = 0.035\%$ or not, for switching from GBN to SR ($P_{error} < 0.035\%$) or for switching from SR to GBN ($P_{error} > 0.035\%$). The system will intentionally and periodically transmit packets using SR for a period and then using GBN for the same period while keeping the records of P_{error} rates vs. throughput to find and update the intersection point (P_{error} threshold).

The average amount of provided throughput improvement by the use of novel proposed AS method under different packet loss rates for GBN and SR is summarized in Table 3.

4. Conclusion and Discussion

In this work, the SDN structure integrated into an Internet of Health Things (IoHT) paradigm for the hospital environment is proposed and designed. Then, a novel proposed adaptive access technique called adaptive switching (AS) and based on traditional Go-Back-N and Selective Repeat technique is proposed.

Finally, the throughput performance of the proposed AS method is compared with the performances of traditional Go-Back-N and Selective Repeat ARQ methods using the developed MATLAB simulation. For this, an optimal P_{error} rate that the network should prefer to switch either from Go-Back-N to Selective Repeat or from Selective Repeat to Go-Back-N method to maximize the network throughput performance is determined. The evaluated results are also confirmed by theoretical calculation results using well-known Mathis throughput formula. It is shown by the evaluated results that when the novel proposed adaptive switching (AS) method is used, the throughput always has its best possible results for all P_{error} rates. Finally, it is being observed from Figure 10 and Table 3 that up to 37.52% throughput improvement is provided by the use of novel proposed adaptive switching (AS) method.

We will examine the performance of the suggested technique in future research by including different properties and critics data in the network, and add to that, we will include the energy factor to overall performance.

Data Availability

All data are available within the manuscript.

Conflicts of Interest

The authors declare that they have no conflicts of interest.

References

[1] A. Lakhan, M. A. Mohammed, J. Nedoma et al., "Federated-learning based privacy preservation and fraud-enabled blockchain IoMT system for healthcare," in *IEEE Journal of Biomedical and Health Informatics*, 2022.

[2] N. Zahid, A. H. Sodhro, U. R. Kamboh et al., "AI-driven adaptive reliable and sustainable approach for Internet of Things enabled healthcare system," *Mathematical Biosciences and Engineering*, vol. 19, no. 4, pp. 3953–3971, 2022.

[3] H. B. Mahajan, A. S. Rashid, A. A. Junnarkar et al., "Integration of Healthcare 4.0 and blockchain into secure cloud-based electronic health records systems," in *Applied Nanoscience*, pp. 1–14, Springer, 2022.

[4] D. A. Hammood, H. A. Rahim, A. Alkhayyat, and R. B. Ahmad, "Duty cycle optimization using game theory two

master nodes cooperative protocol in WBAN," *Wireless Personal Communications*, vol. 122, no. 3, pp. 2479–2504, 2022.

[5] S. Nandy, M. Adhikari, S. Chakraborty, A. Alkhayyat, and N. Kumar, "IBoNN: intelligent agent-based Internet of medical things framework for detecting brain response from electroencephalography signal using bag-of-neural network," *Future Generation Computer Systems*, vol. 130, pp. 241–252, 2022.

[6] M. Y. Mehmood, A. Oad, M. Abrar et al., "Edge computing for IoT-enabled smart grid," *Security And Communication Networks*, vol. 2021, Article ID 5524025, 16 pages, 2021.

[7] S. Razdan and S. Sharma, "Internet of medical things (IoMT): overview, emerging technologies, and case studies," in *IETE Technical Review*, Taylor & Francis, 2021.

[8] D. A. Hammood, H. A Rahim, R. B. Ahmad et al., "Enhancement of the duty cycle cooperative medium access control for wireless body area networks," *IEEE Access*, vol. 7, pp. 3348–3359, 2019.

[9] S. Bera, S. Misra, S. K. Roy, and M. S. Obaidat, "Soft-WSN: software-defined WSN management system for IoT applications," *IEEE Systems Journal*, vol. 12, no. 3, pp. 2074–2081, 2016.

[10] M. Cicioğlu and A. Çalhan, "SDN-based wireless body area network routing algorithm for healthcare architecture," *ETRI Journal*, vol. 41, no. 4, pp. 452–464, 2019.

[11] K. Hasan, X. W. Wu, K. Biswas, and K. Ahmed, "A novel framework for software defined wireless body area network," in *2018 8th International conference on intelligent systems, modelling and simulation (ISMS)*, pp. 114–119, IEEE, Kuala Lumpur, Malaysia, 2018, May.

[12] T. M. Li, C. C. Liao, H. H. Cho, W. C. Chien, C. F. Lai, and H. C. Chao, "An e-healthcare sensor network load-balancing scheme using SDN-SFC," in *2017 IEEE 19th international conference on e-health networking, applications and services (Healthcom)*, pp. 1–4, Dalian, China, Oct. 2017.

[13] M. Al Shayokh, J. W. Kim, and S. Y. Shin, "Cloud based software defined wireless body area networks architecture for virtual hospital," in *Proceedings of the 10th EAI International Conference on Body Area Networks*, pp. 92–95, Sydney, Australia, Sept. 2015.

[14] L. Hu, M. Qiu, J. Song, M. S. Hossain, and A. Ghoneim, "Software defined healthcare networks," *IEEE Wireless Communications*, vol. 22, no. 6, pp. 67–75, 2015.

[15] K. H. Yeh, "A secure IoT-based healthcare system with body sensor networks," *IEEE Access*, vol. 4, pp. 10288–10299, 2016.

[16] F. A. Kraemer, A. E. Braten, N. Tamkittikhun, and D. Palma, "Fog computing in healthcare–a review and discussion," *IEEE Access*, vol. 5, pp. 9206–9222, 2017.

[17] M. Ghamari, B. Janko, R. Sherratt, W. Harwin, R. Piechockic, and C. Soltanpur, "A survey on wireless body area networks for ehealthcare systems in residential environments," *Sensors*, vol. 16, no. 6, p. 831, 2016.

[18] R. M. Madhumathi, A. Jagadeesan, and S. Kaushik, "Healthcare monitoring system using body sensor network," in *Proceedings of the International Conference on Engineering Innovations and Solutions (ICEIS-2016)*, pp. 171–176, Rome, Italy, 2016.

[19] S. R. Moosavi, T. N. Gia, E. Nigussie et al., "End-to-end security scheme for mobility enabled healthcare Internet of Things," *Future Generation Computer Systems.*, vol. 64, pp. 108–124, 2016.

[20] Y. I. Yuehong, Y. Zeng, X. Chen, and Y. Fan, "The Internet of Things in healthcare: an overview," *Journal of Industrial Information Integration*, vol. 1, pp. 3–13, 2016.

[21] T. Wu, F. Wu, J. M. Redouté, and M. R. Yuce, "An autonomous wireless body area network implementation towards IoT connected healthcare applications," *IEEE Access*, vol. 5, pp. 11413–11422, 2017.

[22] L. Catarinucci, D. De Donno, L. Mainetti et al., "An IoT-aware architecture for smart healthcare systems," *IEEE Internet of Things Journal*, vol. 2, no. 6, pp. 515–526, 2015.

[23] X. Chen, M. Ma, and A. Liu, "Dynamic power management and adaptive packet size selection for IoT in e-healthcare," *Computers & Electrical Engineering*, vol. 65, pp. 357–375, 2018.

[24] S. Jabbar, F. Ullah, S. Khalid, M. Khan, and K. Han, "Semantic interoperability in heterogeneous IoT infrastructure for healthcare," *Wireless Communications and Mobile Computing*, vol. 2017, 10 pages, 2017.

[25] A. Darwish, A. E. Hassanien, M. Elhoseny, A. K. Sangaiah, and K. Muhammad, "The impact of the hybrid platform of internet of things and cloud computing on healthcare systems: opportunities, challenges, and open problems," *Journal of Ambient Intelligence and Humanized Computing*, vol. 10, no. 10, pp. 4151–4166, 2019.

[26] E. Luo, M. Z. Bhuiyan, G. Wang, M. A. Rahman, J. Wu, and M. Atiquzzaman, "Privacyprotector: privacy-protected patient data collection in IoT-based healthcare systems," *IEEE Communications Magazine*, vol. 56, no. 2, pp. 163–168, 2018.

[27] F. Ali, S. R. Islam, D. Kwak et al., "Type-2 fuzzy ontology–aided recommendation systems for IoT–based healthcare," *Computer Communications*, vol. 119, pp. 138–155, 2018.

[28] A. Ahmed, M. S. M. Thabit, A. Alkhayyat, and Q. H. Abbasi, "Energy harvesting Internet of Things health-based paradigm: towards outage probability reduction through inter–wireless body area network cooperation," *International Journal of Distributed Sensor Networks*, vol. 15, no. 10, Article ID 155014771987987, 2019.

[29] A. Alkhayyat, A. A. Thabit, F. A. Al-Mayali, and Q. H. Abbasi, "WBSN in IoT health-based application: toward delay and energy consumption minimization," *Journal of Sensors*, vol. 2019, 14 pages, 2019.

[30] I. Marsic, *Computer networks: performance and quality of service*, Rutgers, New Jersey, 2013.

[31] X. Yi and W. Wanye, "Finding the fastest path in wireless networks," in *2008 IEEE International Conference on Communications*, pp. 3188–3192, Beijing-China, 2008.

[32] T. Slattery, "TCP performance and the Mathis equation," 2009, https://www.netcraftsmen.com/tcp-performance-and-the-mathis-equation/.

[33] "Validating a very simple model for TCP throughput," 2013, https://www.thousandeyes.com/blog/a-very-simple-model-for-tcp-throughput/.

Hindawi
Wireless Communications and Mobile Computing
Volume 2022, Article ID 2951168, 10 pages
https://doi.org/10.1155/2022/2951168

Research Article

Development of Pneumonia Disease Detection Model Based on Deep Learning Algorithm

Dalya S. Al-Dulaimi,[1] Aseel Ghazi Mahmoud,[2] Nadia Moqbel Hassan,[3] Ahmed Alkhayyat,[4] and Sayf A. Majeed[5]

[1]*Intelligent Medical Systems Department, University of Information Technology and Communications, Iraq*
[2]*College of Nursing, University of Baghdad, Iraq*
[3]*Computer Engineering Department, College of Engineering, University of Mustansiriyah, Iraq*
[4]*College of Technical Engineering, The Islamic University, Najaf, Iraq*
[5]*Technical Computer Engineering, Al-Hadba University College, Mosul 41001, Iraq*

Correspondence should be addressed to Ahmed Alkhayyat; ahmedalkhayyat85@iunajaf.edu.iq

Received 17 March 2022; Accepted 17 May 2022; Published 6 June 2022

Academic Editor: Ghanshyam Singh

Pneumonia represents a life-endangering and deadly disease that results from a viral or bacterial infection in the human lungs. The earlier pneumonia's diagnosing is an essential aspect in the processes of successful treatment. Recently, the developed methods of deep learning that include several layers of processing to comprehend the stratified data representation have obtained the best results in various domains, especially in the identification and classification of human diseases. Therefore, for improving the systems' performance for detecting pneumonia disease, there is a requirement for implementing automatic models based on deep learning models that have the ability to diagnose the images of chest X-rays and to facilitate the detection process of pneumonia novices and experts. A convolutional neural network (CNN) model is developed in this paper for detecting pneumonia via utilizing the images of chest X-rays. The proposed framework encompasses two main stages: the stage of image preprocessing and the stage of extracting features and image classification. The proposed CNN model provides high results of precision, recall, F1-score, and accuracy by 98%, 98%, 97%, and 99.82%, respectively. Regarding the obtained results, the proposed CNN model-based pneumonia detection has achieved a better result of consistency and accuracy, and it has outperformed the other pretrained deep learning models such as residual networks (ResNet 50) and VGG16. Furthermore, it exceeds the recently existing models presented in the literature. Thus, the significant performance of the proposed CNN model-based pneumonia detection in all measures of performance can provide effective services of patient care and decrease the rates of mortality.

1. Introduction

Pneumonia represents inflammation of lung parenchyma that can result from chemical and physical factors, immunologic injury, pathogenic microorganisms, and other improper pharmaceuticals [1]. Pneumonia can be categorized into noninfectious and infectious relying on various pathogeneses in which noninfectious pneumonia can be categorized into aspiration pneumonia and immune-related pneumonia, while infectious pneumonia can be categorized into the virus, bacteria, chlamydial, mycoplasmas, etc. [2]. The accelerated detection of pneumonia and the subsequent implementation of proper medicine can assist considerably to avoid patients' condition deterioration that ultimately may lead to death [3].

In the last decades, various technologies have appeared like genomics and imaging that offer a complicated and enormous amount of health care data [4]. Chest X-ray images represent the preferable technology in diagnosis pneumonia; however, these images are somewhat not obvious and sometimes misclassified to benign abnormalities or other diseases by the expert radiologists, which lead to giving the wrong medicine to the patients and consequently

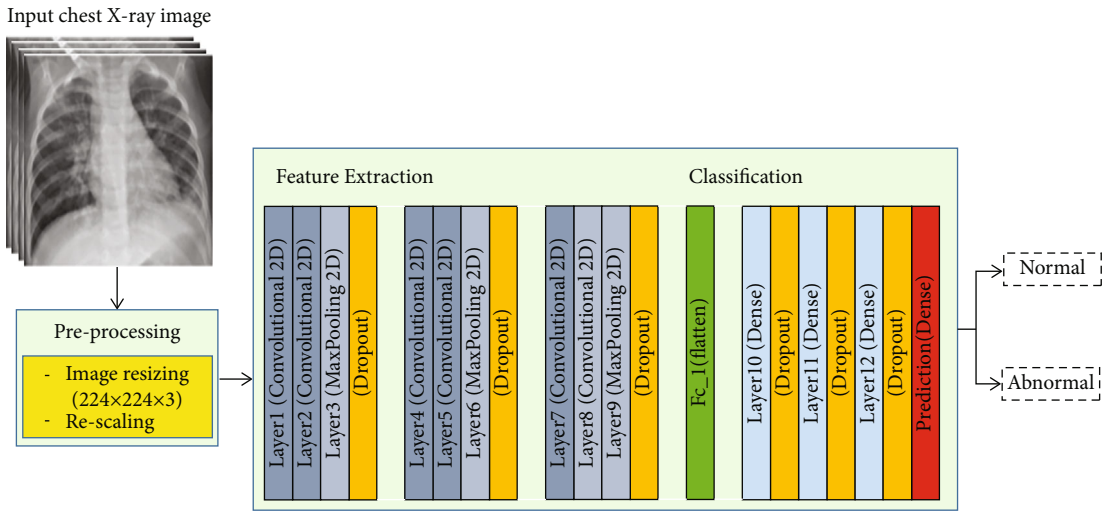

Figure 1: The proposed deep learning framework for detecting pneumonia disease.

worsening the patients' condition [5]. There is a requirement for an automatic and intelligent model to assist radiologists in diagnosing various kinds of pneumonia from the images of chest X-rays [6].

Deep learning represents a subdomain of machine learning regarding algorithms motivated via the structure and function of the brain [7]. The recently developed algorithms of deep learning promote the quantification, identification, and classification of patterns within medical images. Deep learning algorithms are capable of learning features simply from data, rather than hand-designing features depending on field-specific knowledge. The recently utilized model of developed deep learning is the convolutional neural network (CNN). This model of layers works on processing images and coming up with extracting low levels of features (like edges) within images. The layers of CNN can successfully capture the temporal and spatial dependencies in images with the assistance of filters. In contrary to the layers of normal feed-forward, the CNN layers include considerably fewer parameters and utilized a technique of weight sharing, consequently, decreasing the effort of computation. Thus, this developed model helps medical practitioners in diagnosing and classifying specific medical conditions effectively [8].

The main contribution of this work is to provide an effective deep learning framework for detecting pneumonia using the images of chest X-rays with a balanced performance in accuracy and complexity terms, furthermore providing medical and radiologist experts with a lower cost tool. The attended objectives are as follows:

(i) Firstly, applying CNN model to detect pneumonia from the images of chest X-rays as feature extraction and classification scheme

(ii) Secondly, investigating the performance of CNN and other deep learning models in classifying pneumonia

(iii) Finally, developing a model capable of detecting normal and abnormal (pneumonia) images

The residual of this paper is organized as follows; an examination of related works is stated in Section 2. The proposed deep learning model for detecting pneumonia is explained in Section 3, and its efficiency is shown in Section 4. Finally, Conclusions of this paper are highlighted in Section 6.

2. Related Works

Ayan and Ünver [9] compared two CNN models (VGG16 and Xception) for diagnosing pneumonia. In these models, transfer learning and fine-tuning are utilized in the stage of training. The obtained results demonstrated that the Vgg16 model exceeds the Xception model in several metrics: accuracy, specificity, precision, and f-score, by 0.87%, 0.91%, 0.91%, and 0.90%, respectively, while the Xception model exceeds the VGG16 model in sensitivity metric by 0.85%. Furthermore, the Xception model is more effective than the other model in detecting cases of pneumonia, while the VGG16 model is more effective in detecting normal cases. But these models require to be ensemble (combine the strengths) for achieving more effective results in diagnosing pneumonia. Hashmi et al. [10] proposed a model for pneumonia detection in chest X-ray images. In this model, firstly, the dataset was augmented; then, predictions from the pretrained deep learning models (Xception, Inception V3, ResNet 18, MobileNetV3, and DenseNet121) were combined, by utilizing a weighted classifier for computing the final prediction. This proposed model outperforms the other individual models and achieves an accuracy of 98.43%. But the utilized models had highly complex constructions; therefore, it is necessary to provide a model in which the weights according to various models are estimated effectively. Jain et al. [11] presented six CNN models for classifying chest X-ray images into pneumonia and nonpneumonia. These models have differed in the number of utilized parameters, hyperparameters, and convolutional layers. The first and second models include three convolutional layers and

Table 1: The parameters of the CNN model layers.

Layers (types)	Shape_output	Parameters
layer1 (convolutional 2D)	None, "224, 224, 64"	1792
layer2 (convolutional 2D)	None, "224, 224, 64"	36928
layer3 (max pooling 2D)	None, "112, 112, 64"	0
(Dropout)	None, "112, 112, 64"	0
layer4 (convolutional 2D)	None, "112, 112, 128"	73856
layer5 (convolutional 2D)	None, "112, 112, 128"	147584
layer6 (max pooling 2D)	None, "56, 56, 128"	0
(Dropout)	None, "56, 56, 128"	0
layer7 (convolutional 2D)	None, "56, 56, 256"	295168
layer8 (convolutional 2D)	None, "56, 56, 256"	590080
layer9 (max pooling 2D)	None, "28, 28, 256"	0
(Dropout)	None, "28, 28, 256"	0
(Flatten)	None, "200704"	0
layer10 (dense)	None, "512"	102760960
(Dropout)	None, "512"	0
layer11 (dense)	None, "128"	65664
(Dropout)	None, "128"	0
layer12 (dense)	None, "64"	8256
(Dropout)	None, "64"	0
(Dense)	None, "2"	130
Total of parameters: 103,980,418		
Trainable parameters: 103,980,418		
Nontrainable parameters: 0		

provide 85.26% and 92.31% of accuracy, respectively, while the other models are pretrained models (VGG16, VGG19, Inception V3, and ResNet 50) which provide 87.28%, 88.46%, 70.99%, and 77.56% of accuracy, respectively. These presented models are focused on the recall metric as a performance evaluator for minimizing the number of false negatives. The best-obtained recall was achieved by the second model which was 98%. However, these models require to improve the accuracy of classification via fine-tuning each parameter and hyperparameter. Al Mamlook et al. [12] presented seven models for detecting and classifying pneumonia from the images of chest X-rays; these models are random forest, decision tree, K-nearest neighbor, adaptive boosting, gradient boost, XGBboost, and CNN. Particularly, all these models were compared using f-score and accuracy score. The CNN model exceeds the other machine learning models with a small margin, and the obtained score of accuracy was 98.46%. Surprisingly, the random forest model achieved well and the score of accuracy was 97.61%. However, these presented models need to construct a large database for training and testing to provide better results. Wu et al. [13] proposed an improved median filtering based on the CNN model using a random forest algorithm. In this model, the adaptive median filter was firstly utilized for removing noises within the images of chest X-ray to be more easily recognizable; then, the architecture of CNN was established depend on dropout for extracting the features of deep activation from each image. Finally, a random forest dependent on GridSearchCV class was employed as a classifier for the features of deep activation in the CNN model. This proposed model not only works on avoiding the overfitting phenomenon in data training, however improving the image classification accuracy as well. The achieved score of accuracy was 96.9% for $64 \times 64 \times 3$ image size and 93.8% for $224 \times 224 \times 3$ image size. Regarding the achieved accuracy, the achieved scores for precision, recall, and F1-score were 90%, 95%, and 97.7%, respectively. But this model requires improving the CNN model's performance to be more efficient with no further preprocessing work. Chouhan et al. [14] presented a deep learning approach to detect pneumonia based on transfer learning. In this framework, firstly, the chest X-ray images were resized to $224 \times 224 \times 3$; then, the augmentation techniques (random horizontal flip, random resized crop, and a varying intensity) were utilized. After that, the features were extracted from images via utilizing several pretrained models on the dataset (AlexNet, Inception V3, DenseNet121, ResNet 18, and GoogLeNet) to be passed to the classifier for prediction. Finally, an ensemble model was employed that utilized the pretrained models and exceeded individual models. The obtained scores of recall and accuracy were 99.62% and 96.4%, respectively. But the performance of this framework requires further improvement either by increasing the size of the dataset or utilizing handcrafted features. Zhang et al. [15] presented a model based on CNN for diagnosing pneumonia. In this model, the technique of dynamic histogram equalization was firstly utilized to improve the contrast of chest X-ray images; then, the VGG-based CNN model was designed for features extraction and classification. This presented model can classify abnormal and normal chest X-ray images with a 94.41% precision rate and 96.07% accuracy rate. But this model requires exploring a more accurate architecture of classification for diagnosing pneumonia. Manickam et al. [16] preprocessed the input images of chest X-rays for identifying the existence of pneumonia via utilizing the architecture of U-Net based segmentation and classified pneumonia as abnormal and normal via utilizing pretrained models (Inception V3, ResNet 50, and Inception-ResNet V2). The ResNet 50 model exceeds the other models with 96.78% recall, 88.97% precision, 92.71% F1-score, and 93.06% accuracy.

Most of these related works are based on the utilization of a pretrained structure of neural network or finding a specific structure with a specific number of layers. When the number of layers is increased besides the complexity of the features to be detected via the neural network for achieving the required task, the complexity of computations will be increased with no implying any accuracy improvement. Furthermore, the utilization of a few layers can decrease the neural network's accuracy, since the features at the needed level of complexity are not detected. Therefore, the main aim of this work is to implement an effective deep CNN model on a publicly accessible dataset for detecting pneumonia by achieving a balanced performance in accuracy and complexity terms.

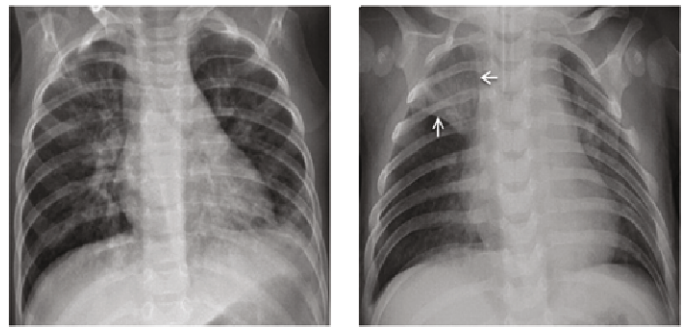

(a) Abnormal-viral pneumonia (b) Abnormal-bacterial pneumonia

(c) Normal

Figure 2: Examples of chest X-ray images.

Table 2: The obtained metrics of precision, recall, F1-score, and accuracy for the proposed CNN model.

Pneumonia classes	Precision	Recall	F1-score	No. of tested images
"Abnormal"	0.98	0.96	0.99	855
"Normal"	0.98	0.97	0.98	318
Accuracy	—	—	0.99	1173
Macroaverage	0.99	0.98	0.97	1173
Weighted average	0.98	0.98	0.97	1173

Table 3: The obtained metrics of precision, recall, F1-score, and accuracy for ResNet 50 model.

Pneumonia classes	Precision	Recall	F1-score	No. of tested images
"Abnormal"	0.95	0.98	0.97	855
"Normal"	0.94	0.86	0.90	318
Accuracy	—	—	0.95	1173
Macroaverage	0.95	0.92	0.93	1173
Weighted average	0.95	0.95	0.95	1173

3. Proposed Methodology

The proposed deep learning framework has been constructed and trained many times with various parameters for choosing the preferable hyperparameters and providing a balanced-performing architecture. Generally, it encompasses two main stages. The first stage involves several image preprocesses; firstly, the process of image resizing which is implemented to obtain $224 * 224 * 3$ image size and, secondly, rescaling the value of the image's pixel to [0,1] interval, while the second stage represents extracting features and image classification utilizing the proposed CNN models.

Table 4: The obtained metrics of precision, recall, F1-score, and accuracy for VGG16 model.

Pneumonia classes	Precision	Recall	F1-score	No. of tested images
"Abnormal"	0.88	0.73	0.80	855
"Normal"	0.50	0.74	0.62	318
Accuracy			0.73	1173
Macroaverage	0.74	0.73	0.73	1173
Weighted average	0.73	0.73	0.71	1173

The proposed CNN model is applied to detect pneumonia from the images of chest X-rays as feature extraction and classification scheme. Figure 1 shows the general structure of the proposed model for detecting pneumonia disease. This structure includes three main parts. The input layer in the CNN model represents the first part (layer) of the CNN structure that passes the input chest X-ray image of size $224 * 224 * 3$ to the next parts.

The feature extraction represents the second part of the CNN structure which includes three blocks, and each block

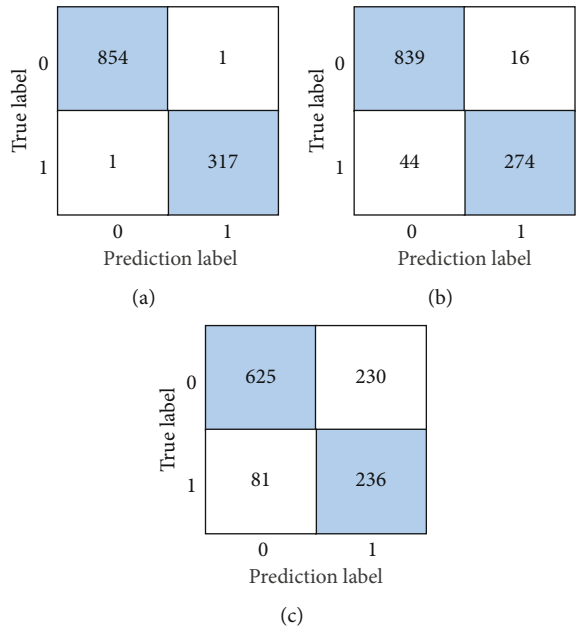

Figure 3: Confusion matrices: (a) proposed CNN model, (b) ResNet 50 model, and (c) VGG16 model.

includes the convolution layer, maximum pooling layer, and dropout layer. In the convolutional layer, the input images are converted into matrix forms. The operation convolution is implemented within the input matrix and a feature kernel of 3×3 dimension, and the outcome represents a feature map. This operation works on reducing the image dimensions to make it easier to be processed.

In order to achieve better performance, all the convolutional layers are followed by the Rectified Linear Unit (ReLU). ReLU is the widely utilized activation function that thresholds the inputs (converts the input to 0 if it is valued less than 0) and creates a nonlinear output.

After that, the max pooling layer is utilized for recognizing the prominent features within the image and reducing the image's dimensions and the parameters, consequently decreasing the computational complexity. The max pooling layer with a 2×2 dimension operates on every feature map and scales its dimensions by utilizing the function "MA" which works on selecting the highest value of a pixel from the image window. The dropout is added to the max pooling layers for preventing overfitting.

The output of the second part is subsequently passed to the third part which is the classification part. This part includes several layers; firstly, the flattened layer that is utilized for changing the shape of the data to a one-dimensional vector, secondly, three dense layers each of which is followed by the dropout layer and, finally, the dense layer of sigmoid activation function that works on classifying output image into normal or abnormal. The number of parameters that are utilized in the CNN model for detecting pneumonia disease is demonstrated in Table 1.

As demonstrated in Table 1, the proposed CNN model encompasses twelve layers (six convolutional layers, three max pooling, and three dense layers), and the number of trainable parameters was 103,980,418.

4. Computational Experiments

Python programming language was utilized in the implementation of the proposed deep CNN, ResNet 50, and VGG16 models. Google Colab was utilized for GPU runtime in the stages of training and validation. Each model was fine-tuned for 100 epochs, with 128 batch-size. The NAdam optimizer was utilized for optimizing the function of learning with 0.001 learning rate.

Regarding the implemented pretrained CNN models, VGG16 included sixteen layers (thirteen-convolution and three-dense), and the ResNet 50 included fifty layers (forty-eight-convolution, one-max pooling, and one-average-pooling). VGG16 had approximately 134 million trainable parameters, and ResNet 50 had approximately 23 million trainable parameters. The same image preprocessing steps are utilized in the implemented pretrained models, while the feature extraction and classification steps follow the structure of each model.

4.1. Dataset Description. The three deep learning models for pneumonia detection are trained and tested on the images of the chest X-ray dataset [17], which includes 5880 samples, 80% (4707 samples) were utilized for training these models, and 20% (1173 samples, 855 abnormal, and 318 normal) were utilized for testing. Figure 2 manifests examples of chest X-ray images in which abnormal-viral pneumonia demonstrates an interstitial pattern in the lungs and abnormal-bacterial pneumonia demonstrates the consolidation of focal lobar, while the normal image demonstrates pure lungs without any abnormal opacification areas in the chest X-ray.

4.2. Evaluation Metrics. The utilized performance metrics for identifying the best model are precision, recall, F1-score, and accuracy. In order to compute these metrics, True

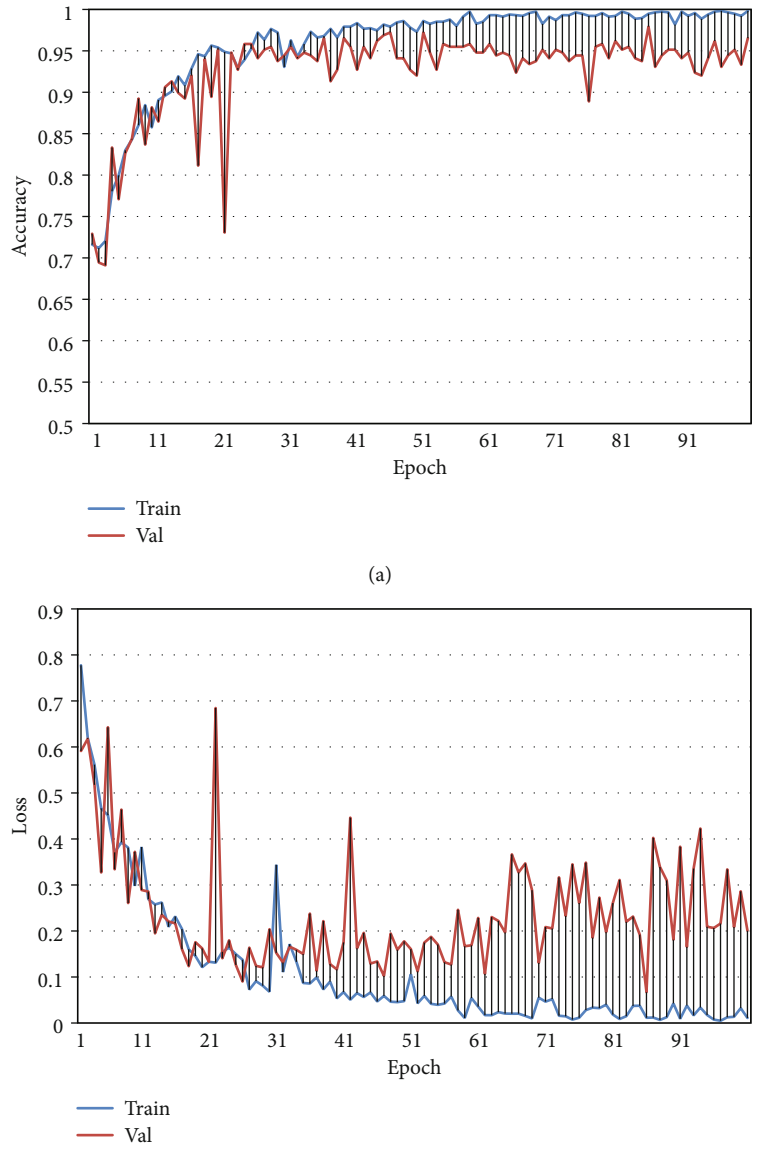

Figure 4: CNN-based pneumonia disease recognition: (a) accuracy per epoch and (b) loss per epoch.

Negative "T_{neg}," True Positive "T_{pos}," False Negative "F_{neg}," and False Positive "F_{pos}" are provided. The lower the T_{neg} and T_{pos}, the fewer classifiers' performance that capable of detecting normal and abnormal (pneumonia) images. The higher the F_{pos} and F_{neg}, the higher classifiers mistakes that misclassify pneumonia images as normal images and conversely. The specificity metric indicates the ability of classifiers to recognize the normal images; it is assigned by T_{neg} and F_{pos} as in

$$\text{Specificity} = \frac{T_{neg}}{\left(T_{neg} + F_{pos}\right)}. \tag{1}$$

The precision metric works on measuring the real abnormal (pneumonia) image percentage from all predicted abnormal images, as in

$$\text{Precision} = \frac{T_{pos}}{\left(T_{pos} + F_{pos}\right)}. \tag{2}$$

The recall metric (sensitivity) is a properly classified class from the model of classification, and the sensitivity with a high value will make the model more reliable and robust. This metric is associated with T_{pos}, as in

$$\text{Recall} = \frac{T_{pos}}{\left(T_{pos} + F_{neg}\right)}. \tag{3}$$

The accuracy metric is utilized for measuring the classification models' performance, and in other words, it

(a)

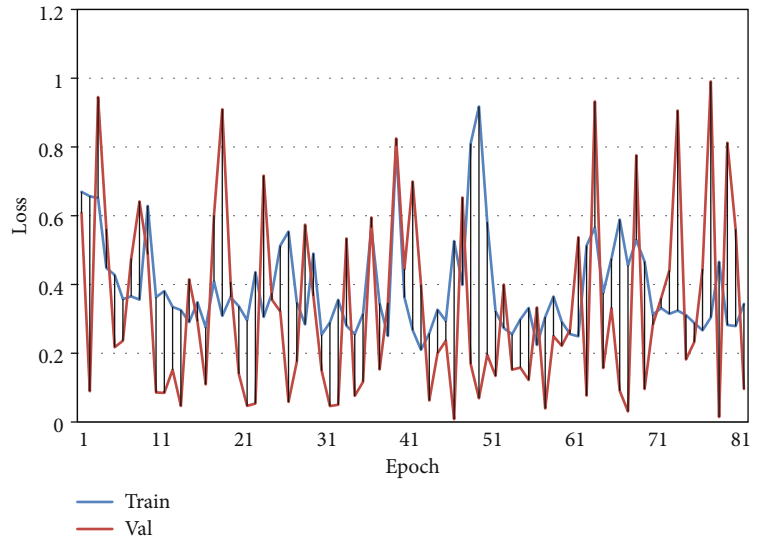

(b)

Figure 5: ResNet 50-based pneumonia disease recognition: (a) accuracy per epoch and (b) loss per epoch.

represents the total classifier performance that is measured by

$$\text{Accuracy} = \frac{\left(T_{\text{neg}} + T_{\text{pos}}\right)}{\left(T_{\text{neg}} + F_{\text{pos}} + T_{\text{pos}} + F_{\text{neg}}\right)}. \quad (4)$$

And finally, F1-score indicates the classifiers' ability of classification via utilizing the combination of precision and recall metrics as a single evaluation metric of performance, as in

$$\text{F1} - \text{score} = \frac{2(Precision \times Accuracy)}{(Precision + Accuracy)}. \quad (5)$$

5. Results and Discussion

Tables 2–4 show the obtained results of the utilized metrics (precision, recall, F1-score, and accuracy) for the proposed CNN model, ResNet 50, and VGG16 models, respectively.

As indicated in Table 2, the CNN model has the best results of precision, recall, F1-score, and accuracy by 98%, 98%, 97%, and 99.82%, respectively.

The obtained results of precision, recall, F1-score, and accuracy for the ResNet 50 model (indicated in Table 3) were 95%, 95%, 95%, and 95.37%, respectively.

The obtained results of precision, recall, F1-score, and accuracy for the VGG16 model (indicated in Table 4) were 73%, 73%, 71%, and 73.40%, respectively.

The confusion matrix offers a perception of the error being obtained via the utilized classifiers. It is utilized for describing the classification performance on the test images

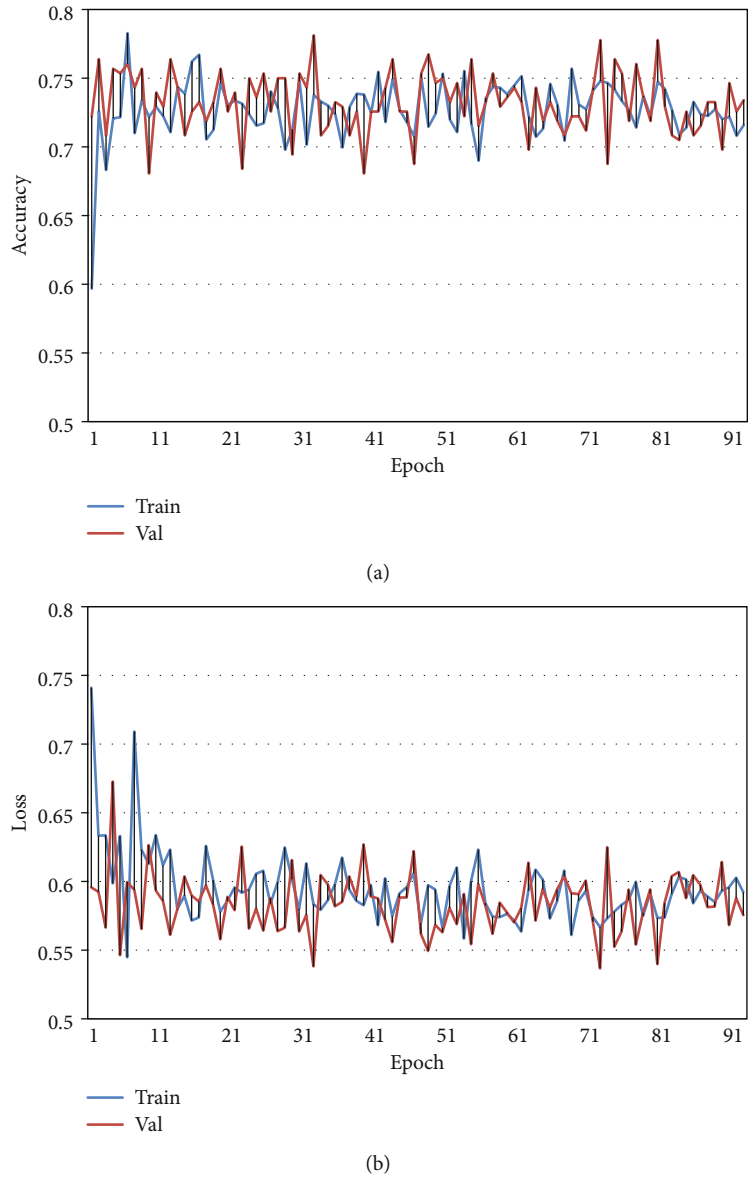

Figure 6: VGG16-based pneumonia disease recognition: (a) accuracy per epoch and (b) loss per epoch.

for the known true values. Figure 3 demonstrates the confusion matrices for the proposed CNN, ResNet 50, and VGG16 models.

The experiments were achieved with 100 epochs, 128 batch size, and "Nadam" optimizer. The accuracy per epoch and loss per epoch for the proposed CNN, ResNet 50, and VGG16 models are illustrated in Figures 4–6, respectively.

As demonstrated in Figure 4, the obtained curves of training and validation accuracy and training and validation loss for the proposed CNN model with 100 epochs were 99.82%, 96.53%, 0.0110, and 0.2005, respectively.

The proposed model has been evaluated by comparing it with the ResNet 50 and VGG16 models and recently presented models using the chest X-ray images as shown in Table 5.

As demonstrated in Table 5, the proposed CNN model-based pneumonia detection has achieved a better result of consistency and accuracy, outperforms the ResNet 50 and VGG16 models, and exceeds the other recently existing models presented in the literature.

6. Conclusion

A deep learning model is proposed in this paper for pneumonia disease detection from the images of chest X-rays. The number of layers is not constantly lead to improve the accuracy, and increasing the networks' layers may yield negative performance. Throughout the construction of the CNN model, an indisputable number of layers was attained that provided the best accuracy.

The obtained results demonstrated that the proposed CNN model-based pneumonia detection has the best high results of precision, recall, F1-score, and accuracy by 98%, 98%, 97%, and 99.82%, respectively, and this leads to the

Table 5: A comparison between the proposed model and other models.

Ref.	Learning models	Precision	Recall	F1-score	Accuracy
[9]	Xception	86%	85%	87%	82%
	VGG16	91%	82%	90%	87%
[10]	Weighted classifier based pretrained models	—	—	98.63%	98.43%
[11]	Inception V3	86%	84%	78%	70.99%
	ResNet 50	92%	97%	84%	77.56%
	VGG16	93%	96%	90%	87.18%
	VGG19	94%	95%	91%	88.46%
[12]	CNN	—	—	98.95%	98.46%
[13]	CNN-random forest	90%	95%	97%	93.8%
[14]	Ensemble model	93.28%	99.62%	94.8%	96.39%
[15]	VGG-based CNN model	94.41%	—	—	96.07%
[16]	ResNet 50	88.97%	96.78%	92.71%	93.06%
—	ResNet 50	95%	95%	95%	95.37
—	VGG16	73%	73%	71%	73.40%
—	Proposed CNN model	98%	98%	97%	99.82%

ability to utilize this model rather than other implemented models as a supplement for radiologists in the process of decision-making. The achieved results support the concept that deep learning models are capable of simplifying the process of diagnosis and improving the management of pneumonia disease and thus leading to improve treatment quality. Furthermore, the proposed CNN model exceeds the other recently existing models presented in the literature. This proposed model can be effectively implemented in diagnosing pneumonia disease and other diseases like COVID-19.

Data Availability

All data are available within the manuscript.

Conflicts of Interest

The authors declare no conflicts of interest.

Acknowledgments

This paper was supported by the University of Information Technology & Communications, University of Baghdad, and Mustansiriyah University.

References

[1] V. Fernandes, G. B. Junior, A. C. de Paiva, A. C. Silva, and M. Gattass, "Bayesian convolutional neural network estimation for pediatric pneumonia detection and diagnosis," *Computer Methods and Programs in Biomedicine*, vol. 208, p. 106259, 2021.

[2] G. U. Nneji, J. Cai, J. Deng, H. N. Monday, E. C. James, and C. C. Ukwuoma, "Multi-channel based image processing scheme for pneumonia identification," *Diagnostics*, vol. 12, no. 2, p. 325, 2022.

[3] A. U. Ibrahim, M. Ozsoz, S. Serte, F. Al-Turjman, and P. S. Yakoi, "Pneumonia classification using deep learning from chest X-ray images during COVID-19," *Cognitive Computation*, pp. 1–13, 2021.

[4] T. M. Hasan, S. D. Mohammed, and J. Waleed, "Development of breast cancer diagnosis system based on fuzzy logic and probabilistic neural network," *Eastern-European Journal of Enterprise Technologies, Information and Controlling System*, vol. 4, no. 9, pp. 6–13, 2020.

[5] T. Rahman, M. E. H. Chowdhury, A. Khandakar et al., "Transfer learning with deep convolutional neural network (CNN) for pneumonia detection using chest X-ray," *Applied Sciences*, vol. 10, no. 9, p. 3233, 2020.

[6] K. T. Islam, S. W. Wijewickrema, A. Collins, and S. O'Leary, "A deep transfer learning framework for pneumonia detection from chest X-ray images," in *In Proc. of the 15th International Joint Conf. On Computer Vision, Imaging and Computer Graphics Theory and Applications*, pp. 286–293, Malta, Valetta, 2020.

[7] A. G. Mahmoud, A. M. Hasan, and N. M. Hassan, "Convolutional neural networks framework for human hand gesture recognition," *Bulletin of Electrical Engineering and Informatics*, vol. 10, no. 4, pp. 2223–2230, 2021.

[8] H. Q. Flayyih, J. Waleed, and S. Albawi, "A systematic mapping study on brain tumors recognition based on machine learning algorithms," in *2020 3rd International Conf. On Engineering Technology and its Applications (IICETA)*, pp. 191–197, Najaf, Iraq, Sept. 2020.

[9] E. Ayan and H. M. Ünver, "Diagnosis of pneumonia from chest X-Ray images using deep learning," in *2019 Scientific Meeting on Electrical-Electronics & Biomedical Engineering and Computer Science (EBBT)*, pp. 1–5, Istanbul, Turkey, April 2019.

[10] F. Hashmi, S. Katiyar, A. G. Keskar, N. D. Bokde, and Z. W. Geem, "Efficient pneumonia detection in chest Xray images using deep transfer learning," *Diagnostics*, vol. 10, no. 6, p. 417, 2020.

[11] R. Jain, P. Nagrath, G. Kataria, V. Sirish Kaushik, and D. J. Hemanth, "Pneumonia detection in chest X-ray images using convolutional neural networks and transfer learning," *Measurement*, vol. 165, p. 108046, 2020.

[12] R. E. Al Mamlook, S. Chen, and H. F. Bzizi, "Investigation of the performance of machine learning classifiers for pneumonia detection in chest X-ray images," in *2020 IEEE International Conf. On Electro Information Technology (EIT)*, pp. 98–104, Chicago, IL, USA, July-1 Aug. 2020.

[13] H. Wu, P. Xie, H. Zhang, D. Li, and M. Cheng, "Predict pneumonia with chest X-ray images based on convolutional deep neural learning networks," *Journal of Intelligent & Fuzzy Systems*, vol. 39, no. 3, pp. 2893–2907, 2020.

[14] V. Chouhan, S. K. Singh, A. Khamparia et al., "A novel transfer learning based approach for pneumonia detection in chest X-ray images," *Applied Sciences*, vol. 10, no. 2, p. 559, 2020.

[15] D. Zhang, F. Ren, Y. Li, L. Na, and Y. Ma, "Pneumonia detection from chest X-ray images based on convolutional neural network," *Electronics*, vol. 10, no. 13, p. 1512, 2021.

[16] A. Manickam, J. Jiang, Y. Zhou, A. Sagar, R. Soundrapandiyan, and R. D. J. Samuel, "Automated pneumonia detection on chest X-ray images: a deep learning approach with different optimizers and transfer learning architectures," *Measurement*, vol. 184, p. 109953, 2021.

[17] D. S. Kermany, M. Goldbaum, W. Cai, M. Anthony Lewis, H. Xia, and K. Zhang, "Identifying medical diagnoses and treatable diseases by image-based deep learning," *Cell*, vol. 172, no. 5, pp. 1122–1131, 2018.